IDŐJÁRÁS

QUARTERLY JOURNAL
OF THE HUNGARIAN METEOROLOGICAL SERVICE

CONTENTS

****

http://www.met.hu/Journal-Idojaras.php

VOL. 114 * NO. 4 * OCTOBER – DECEMBER 2010

IDŐJÁRÁS

Quarterly Journal of the Hungarian Meteorological Service

Editorial Office: Gilice tér 39, H-1182 Budapest, Hungary
P.O. Box 39, H-1675 Budapest, Hungary
E-mail: bozo.l@met.hu or antal.e@met.hu
Fax: (36-1) 346-4809

Indexed and abstracted in Science Citation Index Expanded™ and Journal Citation Reports/Science Edition
Covered in the abstract and citation database SCOPUS®

Subscription by

mail: IDŐJÁRÁS, P.O. Box 39, H-1675 Budapest, Hungary
E-mail: kenderesy.k@met.hu or antal.e@met.hu

IDŐJÁRÁS

Quarterly Journal of the Hungarian Meteorological Service
Vol. 114, No. 4, October–December 2010, pp. 237–250

A new bias correction scheme for assimilating GPS zenith tropospheric delay estimates

Andrea Storto[1,2*] and **Roger Randriamampianina**[1,3]

[1]*Norwegian Meteorological Institute,*
P.O. Box 43, Blindern, N-0313 Oslo, Norway

[2]*Euro-Mediterranean Centre for Climate Change,*
viale Aldo Moro 44, I-40127 Bologna, Italy; E-mail: andrea.storto@cmcc.it

[3]*Hungarian Meteorological Service,*
P.O. Box 38, H-1525 Budapest, Hungary

[*]*Corresponding author*

(Manuscript received in final form August 10, 2010)

Abstract—The impact of GPS zenith tropospheric delay estimated from the ground-based network of GPS receiving stations in the Norwegian regional model is assessed in this work. The data are screened from the stations with irregular or insufficient dissemination of observations. A normality test on the observation minus model-equivalent of the remaining dataset led to 29 assimilated pairs of stations/processing centers from the initial 668. A site-dependent multi-linear scheme that uses model surface pressure, skin temperature, integrated water vapor, and tropospheric thickness as predictors to correct the observation departure biases has been implemented. This scheme is proved to successfully remove the observational error bias. A two-month impact study during the winter of 2008 showed that the selected and bias-corrected dataset was of benefit for geopotential and short-range humidity fields. The impact on temperature fields and precipitation forecasts was neutral.

Key-words: data assimilation, 3d-var, GPS, bias correction

1. Introduction

The zenith tropospheric delay (ZTD) is the converted-to-distance time delay of the Global Positioning System (GPS) signal transmitted by the Global Navigation Satellite System (GNSS) constellation. The time delay is mainly due to the constituents of the troposphere and stratosphere, and GNSS data processing provides estimates of the excess length, rather than a delay, along the zenithal path above the receiving station (*Bevis et al.*, 1992).

The tropospheric delay at the radio frequencies depends on the refractivity $N=10^6(n-1)$, n being the refractive index, integrated over the vertical column from the receiver altitude h to the top of the atmosphere (TOA), namely

$$ZTD = \int_{z=h}^{TOA} [n(z)-1]dz. \tag{1}$$

It is well-known (e.g., *Smith* and *Weintraub*, 1953) that the refractivity, neglecting the Lorentz polarization, can be expressed as

$$N = p_d \frac{K_1}{T} + p_v \left(\frac{K_2}{T} + \frac{K_3}{T^2}\right), \tag{2}$$

where p_d is the partial pressure of dry air, p_v is the partial pressure of water vapor, T is the temperature, and K_1, K_2, and K_3 are three constants. According to the previous formulation of Eq. (2), the refractivity within a zenithal atmospheric path depends on the temperature and specific humidity profiles. It is common practice in GPS meteorology to separate the total delay into a part which depends on surface pressure (called zenith hydrostatic delay, ZHD) and a part which is function of the water vapor distribution (called zenith wet delay, ZWD). The latter can be empirically related to the integrated water vapor (IWV) (*Bevis et al.*, 1992).

Zenith estimates of atmospheric delays have been extensively exploited for mapping the vertical water vapor and the precipitable water content. Since 2005, the EUMETNET EIG GNSS Water Vapour Programme (E-GVAP) has been devoting many efforts in building a homogeneous network of GPS stations over Europe to provide near real-time ZTD estimates to be used in numerical weather prediction (NWP) and nowcasting (*de Haan et al.*, 2004; *de Haan*, 2006).

The comparison of GPS delay data with NWP models and collocated radiosonde observations (*Haase et al.*, 2003; *Deblonde et al.*, 2005) has suggested that GPS zenithal data of delay can be fruitfully used for improving moisture forecasts. Similarly, *Cucurull et al.* (2004) showed that a dense network of stations is able to improve precipitation forecasts in mesoscale models.

Computing temperature and moisture profiles from integrated refractivity data is an inverse problem, as the delay data represent a measure integrated over the vertical. Modern atmospheric data assimilation methods, like the variational ones, are based on the computation of the model departures from the observations in observation space. Hence, they require the computation of the zenith tropospheric delay from the model temperature and humidity profiles, which is a direct problem. In past years, several national weather services have studied the impact of assimilating ZTD data. In the frame of COST Action 716, an improvement of geopotential height has been found at the Danish

Meteorological Institute in the regional three-dimensional data assimilation system (*Vedel* and *Huang*, 2004). At the Swiss Federal Office of Meteorology and Climatology, *Guerova et al.* (2006) used the nudging technique for correcting specific humidity in the low and middle troposphere through IWV synthetic observations derived from the ZWD. They found a positive impact of GPS data during the summer period on the forecasts of humidity, though precipitation forecasts scores were not completely satisfactory. At ECMWF and Météo-France, *Poli et al.* (2007) assimilated ZTDs in global four-dimensional variational (4d-var) schemes with a constant site-dependent bias correction, obtaining promising results in terms of both short-range quantitative precipitation forecasts and medium-range circulation.

In the present implementation, GPS data are assimilated in terms of ZTD, rather than ZWD or IWV, in the HARMONIE-Norway data assimilation system, whose theoretical formulation is briefly reviewed in Section 2. It is important to underline that the quality of the data coming from different processing centers may vary significantly (*Vedel* and *Huang*, 2004); we adopted a strategy consisting in carefully selecting the stations suitable for data assimilation, rather than using a denser but qualitatively inhomogeneous network of observations. Therefore, we have dedicated particular emphasis on the data selection, and implemented an original multi-linear bias removal procedure, which are described in Section 3. Results from a two-month impact study are presented in Section 4. Finally, Section 5 summarizes the main achievements.

2. The data assimilation system

The HARMONIE-Norway data assimilation system, used in this study, is based on the ALADIN regional model data assimilation and forecast system (*Randriamampianina* and *Storto*, 2008), which is developed by the ALADIN consortium (e.g., *Bölöni* and *Horvath*, 2010; *Bubnová et al.*, 1993; *Fischer et al.*, 2005; *Radnoti*, 1995). The HARMONIE-Norway model runs in experimental mode at the Norwegian Meteorological Institute at a resolution of 11 km. The upper-air analysis is performed through a spectral three-dimensional variational (3d-var) data assimilation system, which consists of minimizing a cost function (see e.g., *Courtier*, 1997) given by

$$J=\frac{1}{2}(x-x_b)^T\,\mathbf{B}^{-1}(x-x_b)+\frac{1}{2}(y-\mathbf{H}(x-x_b)-H(x_b))^T\,\mathbf{R}^{-1}(y-\mathbf{H}(x-x_b)-H(x_b)) \quad , \tag{3}$$

where x is the analysis at the minimum of J, x_b is the background, which is a prior estimate of the atmospheric state (a 6-hour forecast), y is the vector of the

observations, H is the fully non-linear *observation operator* which projects the state of the atmosphere onto the space of the observations, **H** is the tangent-linear version of the *observation operator* and **B** and **R** are the covariance matrices of the background and observational errors, respectively. In the formulation of Eq. (3), the fully non-linear observation operator is used only once for computing the initial departures. Conversely, the tangent-linear model is used for updating the cost function at each iteration according to the new model state. This ensures the quadratic form of the cost function. The observation operator for the GPS delay data (*Poli et al.*, 2007) is given by Eqs. (1) and (2) which are computed separately for each model layer and summed up to give the total atmospheric delay along the zenithal path. In particular, to account for possible inconsistencies between the model orography and the actual receiving station altitude, a criterion based on the comparison between the pressure corresponding to the station altitude (computed from the model first-guess fields) and that of the model layers is used: (i) when the station pressure is smaller than the layer top pressure, that layer does not contribute to the total ZTD; (ii) when the station pressure lies in a layer, only the contribution from the station pressure to the layer top pressure is considered; (iii) when the station pressure is greater than the bottom lowest layer pressure, the bottom pressure is changed to that of the station and values of temperature and specific humidity are assumed constantly equal to the layer values between the layer bottom and the station (see *Poli et al.*, 2007 for more details).

In its standard configuration (*Randriamampinina* and *Storto*, 2008), the HARMONIE-Norway supports the assimilation of synoptic station observations (SYNOP), radiosondes (TEMP), surface data from oceanographic buoys (BUOY), wind profilers (PILOT), aircraft observations (AIREP), satellite infrared radiances from MSG/SEVIRI, and microwave radiances from the NOAA and Metop polar-orbiting satellites. The latter satellite and the radiosondes have been proved to be the observation network with largest impact on the forecasts (*Storto* and *Randriamampianina*, 2010a). Background-error covariances are calculated from ensemble global perturbed analysis (*Isaksen et al.*, 2007) downscaled to the regional domain and projected to a 6-hour forecast (*Storto* and *Randriamampianina*, 2010b). The balances are purely statistical, and computed through multi-variate linear regression (*Berre*, 2000).

3. Data processing

3.1. Selection of GPS receiving stations

Usual NWP implementations of the variational theory require the observational errors to follow a normal distribution. The test used for verifying the normality of the observations was the "Omnibus D'Agostino K2 test" (*D'Agostino* and *Pearson*, 1973; *D'Agostino et al.*, 1990), which is a versatile and powerful tool

for both small and large sample sizes. The test has been conducted for all the available couples of station/processing centers using the observation minus first guess (OMF) data for the 6-hour assimilation window in the period of December 1, 2007– April 15, 2008, after having rejected observations suspicious to be affected by gross errors (i.e., with a square OMF departure three times larger than the sum of the observation and background error variances, which for simplicity are assumed constant). Only the stations with a p-value greater than 0.1 have been retained. *Fig. 1* shows the occurrences of the test applied to the OMF data for two couples of station/processing centers; the station on the left panel (SAFONGAA) has been rejected by means of the normality test, while the station ALKMKNM1 (right panel) has been retained. From the initial set of 668 pairs of stations/processing centers, only 37 presented a temporally regular dissemination of the data and have therefore been considered for this impact study. In particular, only an average number of 1 ZTD datum per day within the study period was considered the minimum threshold to include a station among those with sufficient amount of data. Eight stations have been rejected by means of the normality tests and two pairs have been filtered out because of duplication of the ground-based station, leading to a number of retained pairs equals to 29.

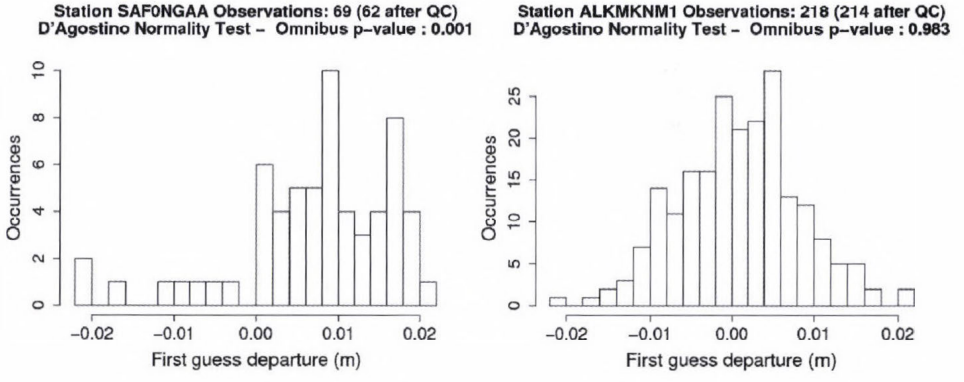

Fig. 1. Occurrences of first guess departures (observation minus first guess) for the station SAFONGAA (12.935° E, 59.136° N), rejected by means of the "Omnibus D'Agostino K2test", and the station ALKMKNM1 (4.728° E, 52.640° N), retained.

Fig. 2 shows the location of the selected stations. Most of them are located in the United Kingdom, Belgium, and the Netherlands, while a few of them are situated in southern Sweden and France. No horizontal thinning of the stations was considered in this study, because of their small amount.

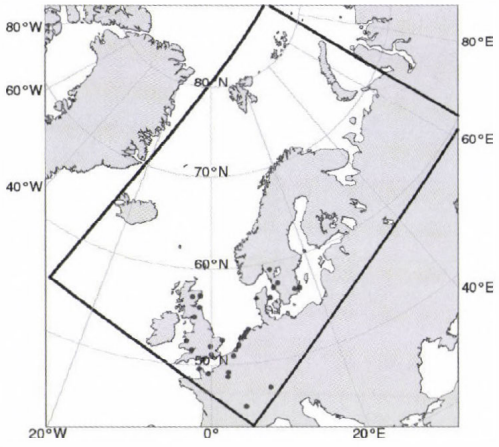

Fig. 2. Geographical distribution of the ground-based GPS stations retained for the assimilation of zenith tropospheric delays. Black lines represent the domain boundaries.

3.2. The ZTD bias correction scheme

In general, the retention of the observational bias, which usually arises from systematic errors in data processing or forecast model, is dangerous as it strengthens and propagates the bias in the analysis and in the forecasts (*Dee*, 2005). We have applied a bias removal that accounts for both GPS processing, observation operator, and NWP model systematic errors. The scheme was inspired by the bias correction scheme proposed by Harris and Kelly (*Harris* and *Kelly*, 2001). This scheme is largely adopted for bias correcting satellite radiances in NWP models. The OMF data can be thought of as the sum of different terms:

$$y - H(x) = \varepsilon_b + \varepsilon_o, \tag{4}$$

where ε_b and ε_o are the background and observational error, respectively. By applying the expectation operator, Eq. (4) becomes

$$E[y - H(x_b)] = b_o + b_b, \tag{5}$$

where b_o and b_b are the biases associated with the observation and the background errors, respectively. We assume that a linear bias model of the form

$$E[y - H(x_b)] = \beta_o + \sum_i \beta_i p_i \tag{6}$$

is able to represent the link between the model parameters and the OMF distribution. In Eq. (6), p_i is the ith predictor of the bias, β_i is its associated

coefficient, and β_0 is the offset. It is clear from Eqs. (5) and (6) that the bias coefficients can be calculated from the OMF dataset through multi-linear regression, if one knows the values of the model predictors corresponding to each observation. In the case of GPS ZTD, the sources of systematic bias in the OMF distribution are represented by errors in GPS data processing (formulation of hydrostatic delay, use of the mapping functions, errors in the ray-path to zenith delay conversion), systematic errors in NWP model fields, and systematic errors in the ZTD observation operator (such as, for instance, the contribution to the total atmospheric delay from the part of the atmosphere above the model top or the mismatch between model orography and station altitude). In addition, *Haase et al.* (2003) demonstrated how the station altitude and the moisture content may affect the bias between the GPS stations and the model-equivalents. In order to account for these several sources of systematic errors, we chose the skin temperature, surface pressure, integrated water vapor (IWV), and thickness of the layer between 950 and 200 hPa as predictors. This choice relies on the idea of representing all of the most significant sources of bias in a simple model: surface pressure and skin temperature are indexes of large-scale regime and hydrostatic delay calculation, and near-surface heating, respectively, and IWV and tropospheric thickness correlation may be thought of as model bias indexes for vertically integrated mass fields and, in general, accuracy of the observation operator. The offset (i.e., the intercept of the regression) also explains systematic errors in data preprocessing. Such a bias correction scheme has been applied independently for each selected pairs of station/processing centers. The calculation of the bias coefficients on an individual station basis stems from the evidence that the correlation between the observational bias and the predictors varies notably between different stations. The OMF dataset was derived from an experiment without GPS ZTDs assimilation but with the on-line computation of the ZTD observation minus first guess. The surface pressure results the parameter most correlated with the observations, with a negative correlation often of the order of -0.4 or -0.5. This seems to be related to the fact that the ZHD calculation, which dominates the total atmospheric delay, relies on the surface pressure fields. The relative importance of the other parameters in explaining the OMF bias depends strongly on the station, and the correlation is globally positive for the skin temperature and the integrated water vapor, whereas negative for the tropospheric thickness. In *Fig. 3*, the correlation coefficients between the predictors and the bias are shown for all the selected stations, together with the station altitude. In addition, also the correlation values between the bias and the stratospheric thickness (between 200 and 50 hPa) are plotted, although this parameter has been excluded from the set of predictors used in the impact study (in the next Section), as it presents a globally smaller correlation. According to *Fig. 3*, it is not possible to see any link between the station altitude and the average integrated moisture content, unlike similar studies (e.g., *Haase et al.*, 2003). The new resulting distribution of the observation minus guess is

unbiased and shows a reduction of standard deviation of the order of 1.5 mm in most cases. Despite the low correlation between the observation bias and the predictors, this bias correction scheme is efficient to correct the GPS bias.

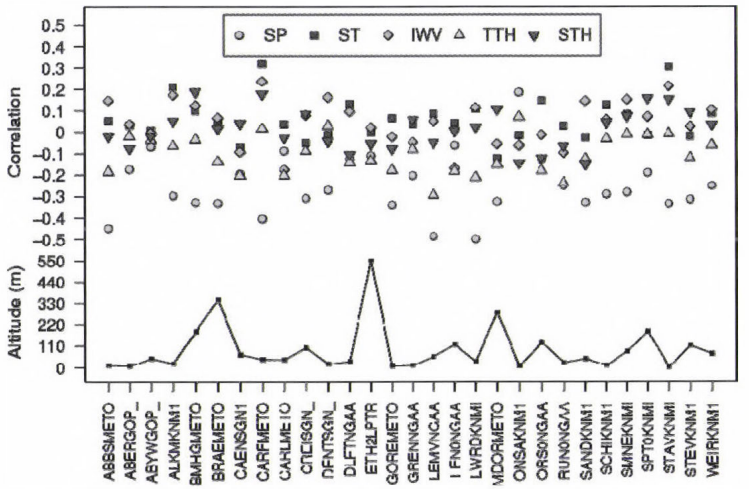

Fig. 3. Correlation values between observational bias and the predictors plus the stratospheric thickness, for all of the selected stations. In the bottom part of the figure, the station altitude is also plotted. The predictors are the surface pressure (SP), skin temperature (ST), integrated water vapor (IWV), tropospheric thickness (TTH, defined as thickness between 950 and 200 hPa pressure levels), and stratospheric thickness (STH, defined as thickness between 200 and 50 hPa pressure levels).

Table 1 demonstrates the impact of our multi-linear bias correction scheme. It reports the mean, the standard deviation and the maximum absolute value of the differences between the constant and the varying part of the bias correction scheme, i.e., between the first and the second term of the right hand side of Eq. (6), along with the station-dependent OMF statistics. Apart from two stations (ONSAKNM1 and STAVKNMI) which present very large differences between the two contributors to the bias correction of the order of tenths of centimeters, most stations show an average difference between the two terms of Eq. (6) of the order of 1 to 6 mm with a standard deviation between 1 and 4 mm. Maximum values are often around 1 cm, which is a value larger than the estimated accuracy of the ZTD (estimated to about 7 mm in both *Haase et al.* (2003) and *Poli et al.* (2007)), thus denoting that the varying part of the bias correction scheme effectively impacts the bias corrected values of the ZTD estimates. This may also be highlighted by comparing the OMF standard deviations with the standard deviation of the flat and the varying part of the bias correction scheme (in *Table 1*), where the former is in general between 2 and 10 times larger than the latter.

Table 1. Station-dependent observation minus guess statistics and difference between the constant and the varying part of the bias correction scheme (in Eq. (6) β_o and $\sum_i \beta_i p_i$, respectively). The table reports the mean the standard deviation of the observation minus guess departures and the mean, the standard deviation and the maximum absolute of the differences of the two components of the bias correction scheme in millimeters within the study period

Station	Observation – guess		Flat – varying		
	Mean	Standard deviation	Mean	Standard deviation	Maximum
ABBSMETO	2.2	10.8	1.1	3.8	9.9
ABERGOP_	7.2	7.0	6.4	1.3	9.4
ABYWGOP_	1.8	8.4	1.4	0.6	3.2
ALKMKNM1	0.8	8.2	0.8	2.5	6.4
BMHGMETO	-1.3	8.5	-1.3	2.8	6.4
BRAEMETO	1.8	7.3	1.7	3.1	10.6
CAENSGN1	8.5	68.0	2.3	2.5	7.2
CARFMETO	-0.4	9.1	-0.4	4.2	9.7
CARLMETO	-1.6	7.6	-1.5	1.9	5.9
CREISGN_	1.5	9.9	1.3	2.6	9.5
DENTSGN_	-0.4	25.9	3.5	2.4	9.9
DLFTNGAA	12.9	93.0	4.4	1.9	8.6
ETH2LPTR	8.7	10.1	6.5	1.9	10.8
GOREMETO	-0.1	10.3	-0.4	3.8	7.9
GRENNGAA	1.6	17.4	0.5	1.9	4.2
LEMVNGAA	1.2	17.9	-1.4	5.5	11.7
LEN0NGAA	8.0	15.4	6.5	1.5	10.4
LWRDKNMI	-0.8	9.5	-0.6	4.9	10.7
MDORMETO	2.5	8.1	2.5	3.0	10.1
ONSAKNM1	-2.5	9.4	-398.9	1.8	402.2
ORS0NGAA	2.2	18.3	4.2	3.0	11.6
RUN0NGAA	8.0	37.0	5.3	2.4	11.0
SANDKNM1	-3.3	8.0	-2.9	2.5	7.5
SCHIKNM1	0.4	9.8	0.2	2.7	7.3
SMNEKNMI	4.9	7.8	4.7	2.1	9.2
SPT0KNMI	4.6	7.0	4.5	1.5	7.8
STAVKNMI	2.3	10.4	-696.9	3.7	704.3
STEVKNM1	0.2	8.6	0.5	2.5	8.0
WEIRKNM1	1.2	9.2	0.9	2.6	6.8

4. Results

The wintertime impact study has been run for the period including February and March 2008, with four daily assimilation and forecast cycles (initialized at 00, 06, 12, and 18 UTC). Basic diagnostic statistics for the assimilation of GPS

delays are shown in *Fig. 4*. In most of the assimilation cycles, the OMF bias varied between –5 and 5 mm, with an average value of 0.6 mm. With respect to the observation minus analysis (OMA) bias, the average value is equal to 0.1 mm. Global standard deviation values of the OMF and OMA were equal to 8.7 and 2.7 mm, respectively. These values are smaller than the standard deviation of the difference between delay data and model-equivalents given by *Haase et al.* (2003), which was equal to 18 mm for the case of the HIRLAM model equivalents. Although this may be seen as a better fit of the HARMONIE-Norway first guess fields with the observations, it should be however mentioned that *Haase et al.* (2003) calculated the statistics within a summertime study period and for a domain covering southern Europe, as both these factors are important for increasing the ZTD OMF standard deviation, due to a larger moisture amount.

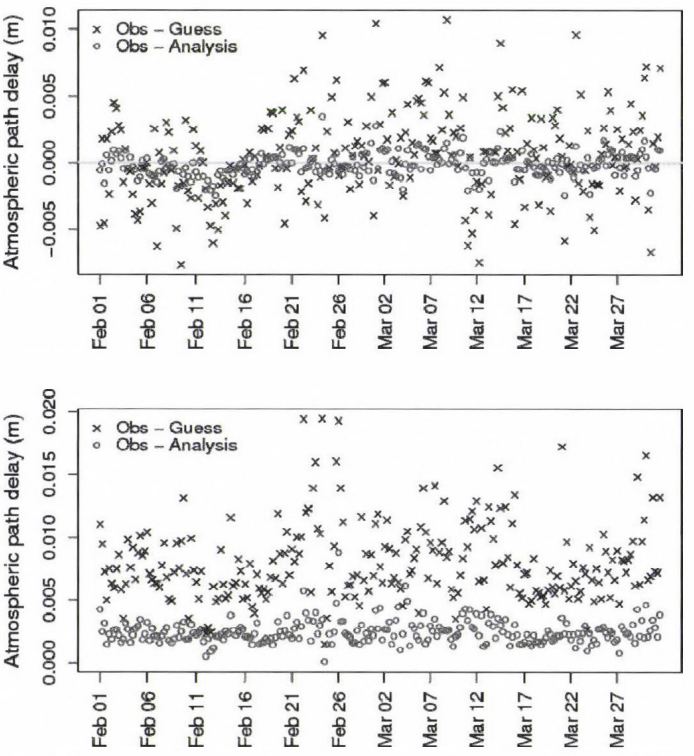

Fig. 4. Bias (top panel) and standard deviation (bottom panel) of observations minus first guess (black crosses) and observations minus analysis (red circles) for the six-hour GPS ZTD assimilation.

To quantify the impact of the GPS delay observations, the bias between the analysis increments of the GPS experiment and the analysis increments of the experiments without GPS data ("GPS" and "NOGPS", respectively) has been

calculated. Most of the signal coming from the new observations is transferred to dynamical parameters, especially for geopotential height (with overall bias reaching 0.3 $m^2 s^{-2}$ in low tropospheric levels), and velocity fields (up to 0.2 $m s^{-1}$), especially in the areas including the Norwegian Sea, the northern part of the Scandinavian peninsula, and the Danish peninsula. Effects of GPS observations on the humidity fields occur mostly in the Belgium and UK areas further to the Norwegian Sea, while the bias of the temperature analysis increment differences is very small. In general, the impact of the GPS observations can be observed rather in lower and middle than in upper tropospheric levels. In *Fig. 5*, the bias of the analysis increments between the two experiments is shown for 850 hPa specific humidity.

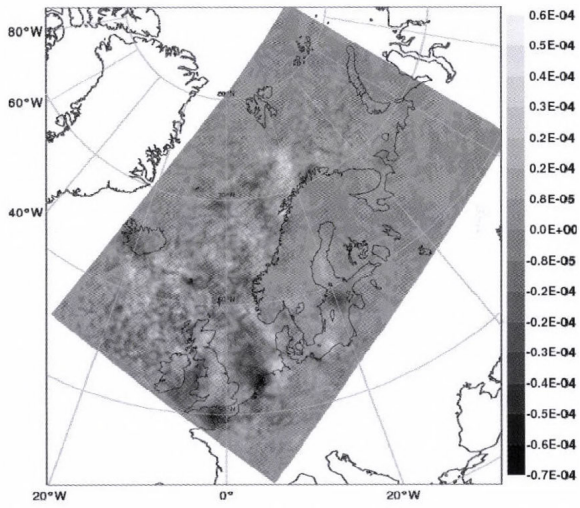

Fig. 5. Bias of analysis increments (analysis minus first guess) of GPS experiment minus NOGPS experiment, averaged over the two-month simulation period for 850 hPa specific humidity (kg/kg).

Verification skill scores against independent radiosonde measurements have been calculated for the overall impact period and compared against the NOGPS experiment. In *Fig. 6*, the contours of the differences between the root mean square error (RMSE) of the NOGPS and the RMSE of the GPS experiment as a function of forecast time and pressure are shown. The overall mean decrease of the error is particularly notable for the geopotential fields at all forecast ranges and below 300 hPa. The positive impact of the ZTD data increases with the forecast length (*Fig. 6*). *Fig. 7* shows the significance test[1] applied to the forecasts differences for the geopitential fields in middle tropospheric

[1] The significance test is based on statistical t-test on the difference in the expected values of the RMSE scores of the compared experiments.

levels (700 hPa). The impact on temperature is neutral to slightly positive, the impact on moisture fields is significantly positive on short-range forecasts throughout the troposphere, while the impact becomes negative on middle-range lower tropospheric levels (*Figs. 6* and *7*). We observed as well small, but significant positive impact of GPS data on two-day forecast of low tropospheric wind speed (not shown). For surface parameters (not shown), verified against independent observations from the EWGLAM network of synoptic stations, the effect of the GPS-ZTD assimilation is slightly positive for surface pressure and negligible for 2-meter temperature and humidity, and 10-meter wind. Unlike other impact studies, we did not find any significant impact on precipitation skill scores.

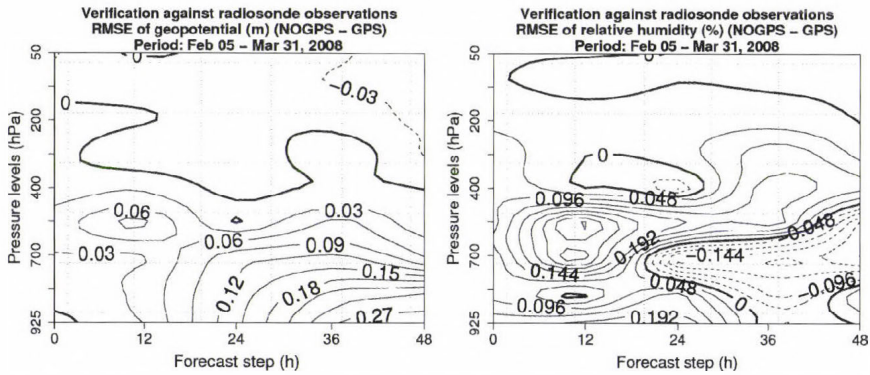

Fig. 6. Radiosonde verification skill scores: contour of differences between RMSE of the reference experiment (NOGPS) and RMSE of GPS experiment as a function of pressure level and forecast length. Positive values indicate that the assimilation of GPS-ZTD decreases the root mean square error; (left) geopotential, (right) relative humidity.

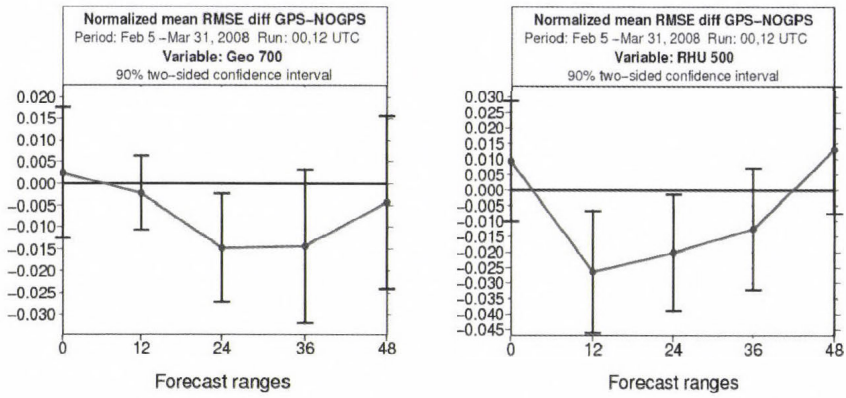

Fig. 7. Significance test: geopotential (left) and relative humidity (right) normalized mean RMSE differences at 700 hPa and 500 hPa, respectively The RMSE was computed from differences against observations.

5. Conclusions

At present, HARMONIE-Norway supports the assimilation of zenith tropospheric delay data from the ground-based GPS stations directly in the 3d-var assimilation system. Model-equivalents of the zenith delays are calculated as refractivities integrated over the vertical column. The strategy adopted in this study aims to evaluate the impact of those few stations, which are considered reliable according to (i) a criterion of regularity in the data availability and (ii) to the "Omnibus D'Agostino K2 test" of Normality of the OMF distribution. Instead of a constant site-dependent bias correction procedure, we noted a non-negligible correlation between the observation minus guess values and several surface and upper-air integrated parameters. This approach facilitated the identification of some sensitive predictors for a bias correction scheme, through multi-linear regression of OMF, independently for each station. Such a strategy allowed to have unbiased observation departures and, in most cases, a sensitive reduction of the OMF standard deviation. As point of discussion, the hierarchy of correlation between OMF bias and model predictors may largely vary among the GPS stations, except for the surface pressure which shows an important correlation for almost all the stations. As a matter of course, we stress the importance of the station-dependent definition of the bias correction scheme, which we kept in the data assimilation system. A wintertime impact study during February and March 2008 proved small but promising positive impact of GPS data on the regional HARMONIE-Norway assimilation and forecast system, especially for geopotential fields and short-range moisture forecasts. Negligible impact on temperature fields, skin parameters, and precipitation forecasts was found.

Acknowledgements—The authors are grateful to *Henrik Vedel* (Danish Meteorological Institute) and *Paul Poli* (Météo-France) for their support in the use of ZTD data. Two anonymous reviewers and the Executive Editor are acknowledged for the important help in improving the quality of this manuscript.

References

Berre, L., 2000: Estimation of synoptic and mesoscale forecast error covariances in a limited-area model. *Mon. Weather Rev. 128*, 644-667.

Bevis, M., Businger, S., Herring, T., Rocken, C., Anthes, R., and *Ware, R.H.*, 1992: GPS meteorology: Remote sensing of atmospheric water vapor using the global positioning system. *J. Geophys. Res. 97*, 15787-15801.

Bölöni, G. and *Horvath, K.*, 2010: Diagnosis and tuning of background error statistics in a variational data assimilation system. *Időjárás 114*, 1-19.

Bubnová, R., Horányi, A., and *Malardel, S.*, 1993: International project ARPEGE/ALADIN. In *Newsletter 22*, EWGLAM, 117–130.

Courtier, P., 1997: Variational methods. *J. Meteorol. Soc. Japan 75*, 211-218.

Cucurull, L., Vandenberghe, F., Barker, D., Vilaclara, E. and *Rius, A.*, 2004: Three-dimensional variational data assimilation of ground-based GPS ZTD and meteorological observations during the 14 December 2001 storm event over the western Mediterranean Sea. *Mon. Weather Rev. 132*, 749-763.

D'Agostino, R.B. and *Pearson, E.S.*, 1973: Testing for departures from normality. *The American Statistician 60*, 613-622.

D'Agostino, R.B., Belanger, A. and *D'Agostino, R.B.J.*, 1990: A suggestion for using powerful and informative tests of normality. *The American Statistician 44*, 316-321.

Deblonde, G., MacPherson, S., Mireault, Y. and *Héroux, P.*, 2005: Evaluation of GPS Precipitable Water over Canada and the IGS Network. *J. Appl. Meteorol. 44*, 153-166.

Dee, D., 2005: Bias and data assimilation. *Q. J. Roy. Meteor. Soc. 131*, 3323-3343.

de Haan, S., 2006: Measuring atmospheric stability with GPS. *J. Appl. Meteorol. 45*, 467-475.

de Haan, S., Barlag, S., Baltink, H. and *Debie, F.*, 2004: Synergetic use of GPS Water Vapor and Meteosat images for synoptic weather forecasting. *J. Appl. Meteorol. 43*, 514-518.

Fischer, C., Montmerle, T., Berre, L., Auger, L., and *Stefănescu, S.*, 2005. An overview of the variational assimilation in the ALADIN/FRANCE NWP system. *Q. J. Roy. Meteor. Soc. 131*, 3477-3492.

Guerova, G., Bettems, J.-M., Brockmann, E. and *Matzler, C.*, 2006: Assimilation of COST 716 near-real time GPS data in the nonhydrostatic limited area model used at MeteoSwiss. *Meteorol. Atmos. Phys. 91*, 149-164.

Haase, J., Maorong, G., Vedel, H. and *Calais, E.*, 2003: Accuracy and variability of GPS tropospheric delay measurements of water vapor in the Western Mediterranean. *J. Appl. Meteorol. 42*, 1547-1568.

Harris, B. A. and *Kelly, G.*, 2001: A satellite radiance-bias correction scheme for data assimilation. *Q. J. Roy. Meteor. Soc. 127*, 1453-1468.

Isaksen, L., Fisher, M. and *Berner, J.*, 2007: Use of analysis ensembles in estimating flow-dependent background error variance. In *ECMWF Workshop on Flow-dependent Aspects of Data Assimilation*. 11–13 June 2007, Reading, United Kingdom.

Poli, P., Moll, P., Rabier, F. Desroziers, G., Chapnik, B., Berre, L., Healy, S., Andersson, E., and *El Guelai, F.-Z.*, 2007: Forecast impact studies of zenith total delay data from European near real-time GPS stations in Météo France 4DVAR. *J. Geophys. Res. 112*, 644-667.

Radnóti, G., 1995: Comments on "A spectral limited-area formulation with time-dependent boundary conditions applied to the shallow-water equations". *Mon. Weather Rev. 123*, 3122-3123.

Randriamampianina, R. and *Storto, A.*, 2008: ALADIN-HARMONIE/Norway and its assimilation system: the implementation phase. *HIRLAM Newsletter 54*, 20-30.

Smith, E. and *Weintraub, S.*, 1953: The constants in the equation for atmospheric refractive index at radio frequencies. In *Proceedings of IRE*, 1035-1037.

Storto, A., and *Randriamampianina, R.*, 2010a: The relative impact of meteorological observations in the Norwegian regional model as determined using an energy norm-based approach. *Atmos. Sci. Let. 11*, 51-58.

Storto, A. and *Randriamampianina, R.*, 2010b: Ensemble variational assimilation for the representation of background-error covariances in a high-latitude regional model. *J. Geophys. Res. Atmospheres 115*, D17204, doi: 10.1029/2009JD013111.

Vedel, H. and *Huang, X.-Y.*, 2004: Impact of ground based GPS data on Numerical Weather Prediction. *J. Meteorol. Soc. Japan 82*, 459-472.

IDŐJÁRÁS

Quarterly Journal of the Hungarian Meteorological Service
Vol. 114, No. 4, October–December 2010, pp. 251–261

Analysis of climate change in Hungary according to an extended Köppen classification system, 1971–2060

Áron Péter Fábián[1] and **István Matyasovszky**[2]

Department of Meteorology, Eötvös Loránd University,
P.O. Box 32, H-1518 Budapest, Hungary
E-mails: [1]*csigaa@gmail.com,* [2]*matya@ludens.elte.hu*

(Manuscript received in final form August 31, 2010)

Abstract—The purpose of this paper is to provide information on tendencies of the climate change in the area of Hungary (48.3°–45.5° W; 16.0°–22.3° E) between 1971 and 2060. Future climate change results obtained from climate models are not used directly due to their uncertainties and inaccuracies, but spatio-temporal distribution of climate classes of the Köppen climate classification system is analyzed. It has become clear that the Köppen system is unable to indicate the expected warming of the summer in certain cases, thus, two additional climate classes are introduced. Two datasets are used, the CRU TS 1.2 (with a spatial resolution of $1/6 \times 1/6$ degrees) for observed temperature and precipitation, and TYN SC 1.0 (same resolution) for climate model generated data. In the latter case, all the four available emission scenarios (A1FI, A2, B1, B2) are analyzed. The climate class of each grid box is calculated for each year from temperature and precipitation data, then the changes of areas covered by the classes resulted from the previous step are analyzed. The evaluation of tendencies is based on 10- and 30-year climate average maps and on the extremes of yearly values of each class. It is found that climate extremes will strengthen in the future during a nearly constant warming. Additionally, the more and more frequent appearance of the steppe climate and the constant presence of the dry-summered class at the end of the period show growing aridity in the area.

Key-words: climate change, climate model, Köppen climate system, warming, drought

1. Introduction

Assessment of both the climate change experienced in recent decades and regional characterization of the anticipated global climate change is in the focus of research. The purpose of this paper is to provide information on tendencies of the climate change in the area of Hungary between 1971 and 2060. As the global or even regional climate models reproduce the observed climate with high

inaccuracies (*Bartholy et al.*, 2006; *Bartholy et al.*, 2008; *Szépszó* and *Horányi*, 2008) over the area of Hungary, future climate change results obtained from these models are not used directly but spatio-temporal distribution of climate classes of the Köppen climate classification system is analyzed.

Because model generated values of meteorological variables are used to determine these climate classes, their inaccuracies might result in climate class uncertainties. However, the applied classification methods are quite insensitive to deviations and errors (*Beck et al.*, 2006).

2. Data and methods

2.1. The Köppen climate classification system

The Köppen climate classification system is a so-called effective system. It classifies the climate by environmental characteristics and given threshold values of given climate components. The components used for classification are: annual mean temperature (t), annual precipitation amount (r), monthly average temperatures of the summer and winter months, monthly precipitation amounts of the summer and winter months, mean temperature of the summer and winter, precipitation amounts of the summer and winter, monthly mean temperatures of the 4 warmest months, monthly mean temperature of the coldest month, and elevation above the sea level. Threshold values of the climate classes which are likely to appear in Hungary are described in *Tables 1–3* according to *Critchfield* (1983).

Table 1. Arid Köppen climate classes according to *Critchfield* (1983)

Class	Description	Precipitation limit r (cm)	Temperature limit t (°C)
Arid with winter precipitation: at least 70% of the annual precipitation falls in the 6 coldest months, and $r < 2t$ applies			
BW	Desert	$r < t$	-
BSh	Warm steppe	$r > t$	$t > 18$
BSk	Cold steppe	$r > t$	$t < 18$
Arid with summer precipitation: at least 70% of the annual precipitation falls in the 6 warmest months, and $r < 2(t + 14)$ applies			
BW	Desert	$r < t + 14$	-
BSh	Warm steppe	$r > t + 14$	$t > 18$
BSk	Cold steppe	$r > t + 14$	$t < 18$
Arid with balanced precipitation: less than 70% of the annual precipitation falls in either halves of the year, and $r < 2(t + 7)$ applies			
BW	Desert	$r < t + 7$	-
BSh	Warm steppe	$r > t + 7$	$t > 18$
BSk	Cold steppe	$r > t + 7$	$t < 18$

Table 2. Temperate rain Köppen climate classes according to *Critchfield* (1983)

Class	Description	Summer (warmest month)	Winter (coldest month)	Precipitation
Cs	Arid in summer	Mean temperature over 10 °C	Mean temperature over -3 °C	Sum of the most arid summer month is less than 4 cm, and also less than the tierce of the precipitation sum of the most humid winter month
Cw	Arid in winter	Mean temperature over 10 °C	Mean temperature over -3 °C	Sum of the most arid winter month does not exceed the tenth of the precipitation sum of the most humid summer month
Cfa	Balanced precipitation	Mean temperature over 22 °C	Mean temperature over -3 °C	Balanced
Cfb	Balanced precipitation	Mean temperature over 10 °C for 4 months	Mean temperature over -3 °C	Balanced
Cfc	Balanced precipitation	Mean temperature over 10 °C	Mean temperature over -3 °C	Balanced

Table 3. Boreal forest and snow Köppen climate classes according to *Critchfield* (1983)

Class	Description	Summer (warmest month)	Winter (coldest month)	Precipitation
Ds	Arid in summer	Mean temperature over 10 °C	Mean temperature below -3 °C	Sum of the most arid summer month is less than 4 cm, and also less than the tierce of the precipitation sum of the most humid winter month
Dw	Arid in winter	Mean temperature over 10 °C	Mean temperature below -3 °C	Sum of the most arid winter month does not exceed the tenth of the precipitation sum of the most humid summer month
Dfa	Balanced precipitation	Mean temperature over 22 °C	Mean temperature below -3 °C	Balanced
Dfb	Balanced precipitation	Mean temperature over 10 °C for 4 months	Mean temperature below -3 °C	Balanced
Dfc	Balanced precipitation	Mean temperature over 10 °C	Mean temperature below -3 °C	Balanced
Dfd	Balanced precipitation	-	Mean temperature below -38 °C	Balanced

The original classification system is inappropriate to represent warming trends in such environments where the thresholds of Cfa or Dfa apply, but the highest monthly mean temperature is far above 22 °C. There is a need, therefore, to introduce additional climate classes to identify the warming of the climate regions with already hot summer in the beginning of the time series. Of course, the original methodology of the system is kept in sight. The newly-introduced classes are:

- **Cfa+**: the monthly mean temperature exceeds 22 °C for at least 4 months,
- **Dfa+**: the monthly mean temperature exceeds 22 °C for at least 4 months.

2.2. The CRU TS 1.2 data set

The *CRU TS 1.2* (*Mitchell et al.*, 2004) is a gridded data set of monthly means and sums of several climate variables for the period of 1901–2000 with a resolution of $1/6 \times 1/6$ degrees. Its spatial coverage is defined by the 11° W–32° E longitudes and 34°–72° N latitudes including the entire continent of Europe. Actually, temperature means and precipitation totals are used over an area with latitudes 48.3°–45.5° N and longitudes 16.0°–22.3° E represented by $18 \times 40 = 720$ grid boxes.

2.3. The TYN SC 1.0 data set

The *TYN SC 1.0* (*Mitchell et al.*, 2004) is a gridded data set of monthly means and sums of several climate variables for the period of 2001–2100 with a spatial coverage and resolution as in the case of the CRU TS 1.2 data set. It does not contain raw model output, but its values are derived from the means of 1961–1990, the variability of 1961–1990, and a model provided response pattern to the rise of temperature. This method, although does not use downscaling of the model-generated data, can give more accurate results than raw model output as it bypasses the inaccurate prediction process of mean and variability, and replaces them by real observed data (*Mitchell et al.*, 2004).

Temperature means and precipitation amounts obtained from the HadCM3 (*Gordon et al.*, 2000) climate model with 4 scenarios (A1FI, A2, B1, B2) (*IPCC*, 2000) are used. The A1FI scenario expects a future with fast technological development and convergence between regions, but strong reliance on fossil fuels. The A2 describes a more heterogeneous, less technically developed world. The B1, like A1, assumes convergence, but along with changes in economical structure and more usage of resource-effective technologies. The B2 works with slower, more locally focused development, but also optimal environmental politics, unlike A2.

2.4. Software used for data processing

Calculations have been performed with an own developed software written in the Python programming language. A scheme of its operation is shown in *Fig. 1*,

a more detailed discussion can be found in the Appendix. Three kinds of products were made: climate maps for each analyzed periods (10-year average maps from the observed and 30-year average maps from the predicted datasets), extremes plots showing the minimum and maximum gridbox numbers covered by all climate classes in all years of the analyzed period, and annual spatial mean temperature diagrams for each analyzed period.

The analysis of climate change was mainly based on the average maps; the extreme plots were used to indicate the variability during the analyzed periods. For instance, an arid climate class with relatively high maximum value indicates that although this class may not appear on the average map (wetter years compensate it), there were droughts during the analyzed period.

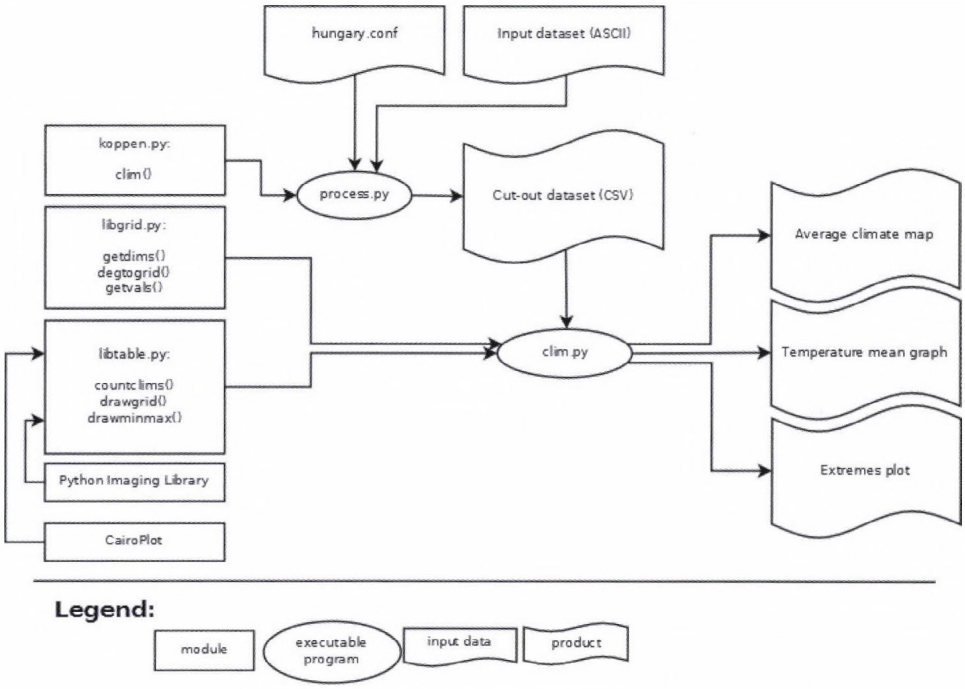

Fig. 1. A scheme of the software used for Köppen climate classification.

3. Results

3.1. Observed data

The climate of Hungary, according to the averages of the period 1951–2000 is classified as mild wintered and moderately warm summered Cfb class (*Kottek et al.,* 2006). However, the analysis of the years from 1971 to 2000 with the above

mentioned higher spatial resolution produces more precise and quite different results. The time series of annual spatial mean temperatures (*Fig. 2*) shows a quasi-constant rise with minor declines that can also be observed in the occupied areas of the climate classes through the period.

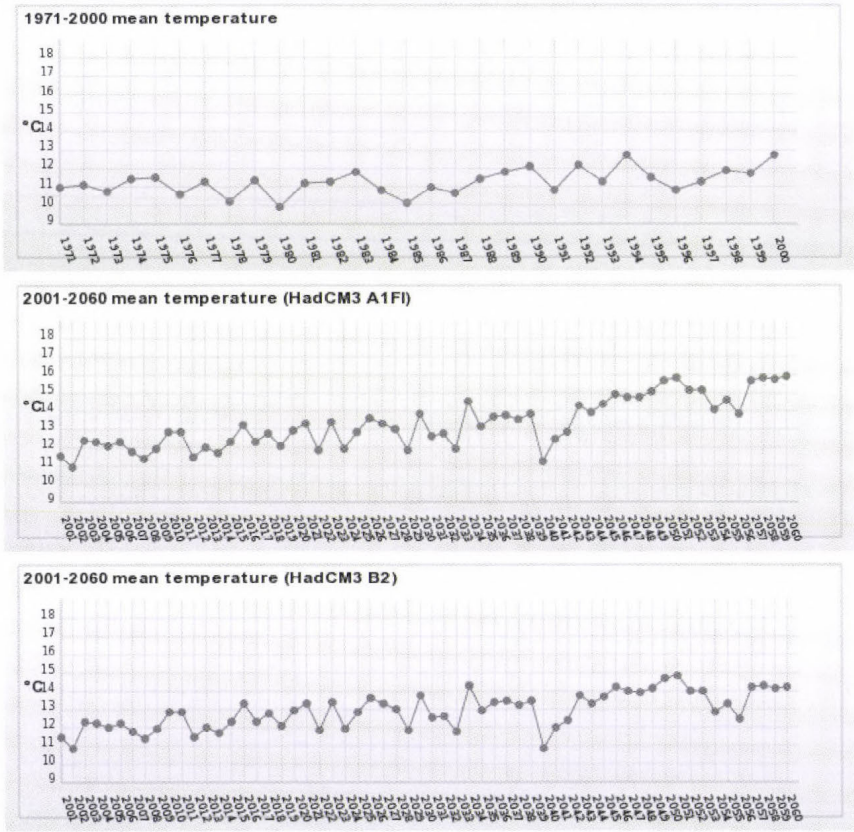

Fig. 2. Spatially averaged annual mean temperature for the periods of 1971–2000 (top) and 2001–2060 for scenarios A1FI (middle) and B2 (bottom).

3.1.1. The 1970s (1971–1980)

The climate average map of the 1970s (*Fig. 3*) shows an almost concentric spatial distribution: the middle of the basin is dominated by the hot summered and mild wintered Cfa, the hill and mountain regions are covered by the cooler summered Cfb, while the north is accompanied by the colder wintered Dfb. The extremes plot shows remarkable Cw-Cs and Cfb-Dfb fluctuations. The prior indicates intense oscillations in the distribution of precipitation through the years; the latter shows the same in mean temperature of the winter.

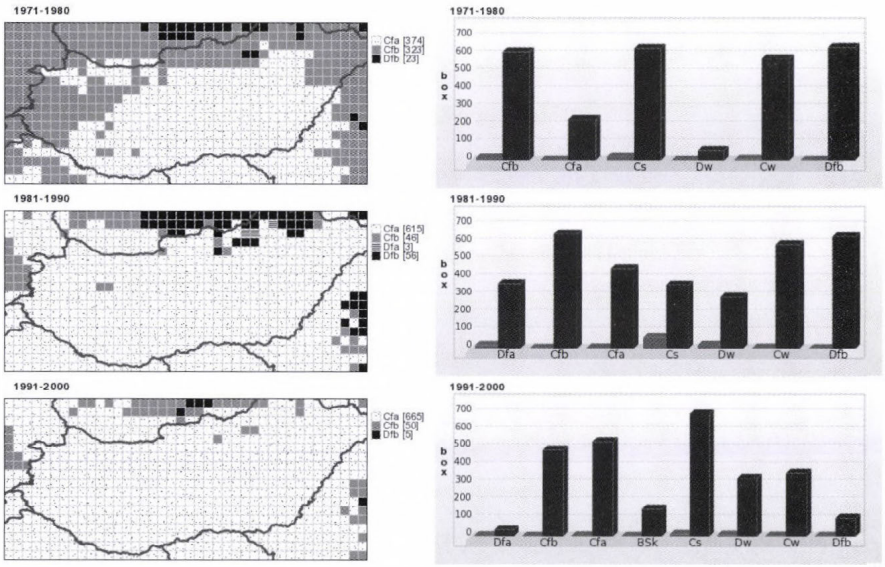

Fig. 3. Spatial distribution of Köppen climate classes with numbers of grid boxes (in parentheses) corresponding to different classes (left), and maximum (dark) and minimum (bright) numbers of grid boxes corresponding to different climate classes in individual years of the ten-year periods of 1971–2000 (right).

3.1.2. The 1980s (1981–1990)

On the average map of the 1980s (*Fig. 3*), the area of Cfa grows remarkably on the expense of Cfb (warming of summer), and the border of the northern Dfa zone expands to south suggesting the cooling of winters in these territories. The extremes plot shows again the Cfb-Dfb fluctuation started in the previous decade, but with lesser disturbances of the annual temporal distribution of precipitation (reduction of Cs area) and with somewhat major fluctuations in the mean temperature (Cw-Dw – mild or cold winter) as compared to the 1970s. These changes show a cooling in this decade identified also in the 30-year spatial mean temperature plot. The lower summer mean temperatures explain the phenomenon (*Szalai et al.*, 2005).

3.1.3. The 1990s (1991–2000)

In the 1990s (*Fig. 3*), the expansion of the Cfa area and the narrowing of colder climates continues. After the temporary decline during the previous decade, the rise of mean temperature returns. This tendency can also be observed in the extremes plot where the D classes are almost missing. Additionally, the considerably high maximum of the dry-summered Cs class with appearance of the steppe (BSk) show rising aridity with general and summer-specific precipitation reduction in the area.

3.2. Climate model generated data

The period 2001–2060 was analyzed according to the four emission scenarios. The scenarios generated similarly fluctuating spatial mean temperature curves (*Fig. 2*), but the slopes differ in each scenario. The entire period was divided into two intervals including the years 2001–2030 and 2031–2060, respectively. All scenarios produced similar results for the near-future period (2001–2030), so only one scenario (A1FI) is presented in this case. However, two scenarios – one with the least extreme changes (B2) and one with the most extreme changes (A1FI) – are presented for the latter period (2031–2060).

3.2.1. The period 2001–2030

The climate average map of this period is similar to the previous one (1990s) but with more Cfb in the borders of the basin indicating colder summers in these areas (*Fig. 4*). Additionally, the Dfb almost vanishes in this area showing the warming of the winters. In the middle of the basin, the mild-wintered, hot-summered Cfa still dominates. The extremes diagram is also very similar to the 1990s. The Cw and BSk maximums are higher on the expense of Cs, so the rise of aridity continues throughout this period.

3.2.2. The period 2031–2060 (A1FI)

The most intense climate change was obtained with scenario A1FI in this period (*Fig. 4*). On the average map, the Dfb fully and the Cfb almost vanishes. In the southern region, a big area of the very hot summered Cfa+ emerges. These changes unanimously indicate the warming of the summer. The majority of the basin remains Cfa. On the extremes plot, the maximum levels of BSk and Cs are remarkably higher than in the previous period, so very dry years can be counted on. As the Cw reduces the precipitation distribution has changed throughout the year. The relatively high maximum and minimum of Dfa+ (cold winter, very hot summer) shows extreme fluctuations of the temperature throughout the year in some regions.

3.2.3. The period 2031–2060 (B2)

The B1 scenario shows more similar picture to the previous period (*Fig. 4*). On the average climate map, the Cfb area reduces remarkably, although some Dfb remains. The coverage of Cfa+ in the south is also smaller. These effects involve a more moderate warming compared to A1FI. The extremes plot also shows milder changes: the maximum of BSk reduces, but the rising of Cs (observed in A1FI) is also unharmed here. The reduction of Cw is also observable, but the Dfa+ is weaker as compared to A1FI. To summarize, the B2 scenario shows almost the same changes as A1FI, but with a remarkably smaller level.

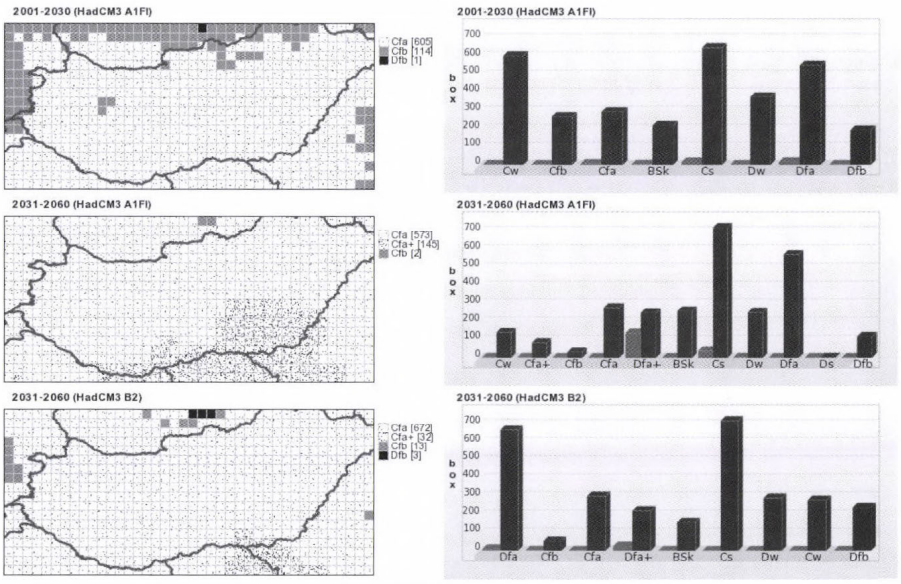

Fig. 4. Spatial distribution of Köppen climate classes with numbers of grid boxes (in parentheses) corresponding to different classes (left), and maximum (dark) and minimum (bright) numbers of grid boxes corresponding to different climate classes in individual years of the thirty-year periods of 2001–2060 (right).

4. Conclusions

The dominant climate class of the observed period 1971–2000 was Cfa in contrary to *Beck*'s (2006) results. Although the yearly results showed fluctuations with different magnitudes of the mean temperature and precipitation distribution, the area of Cfa extended on expense of the colder wintered and summered climate classes. This tendency fully coincides with the almost constant rise of mean temperatures observed in the period. Additionally, the emergence of steppe (BSk) in the last decade means minor drying.

In the climate model generated datasets, a warming tendency evidently exists. Also, the summer precipitation unanimously reduces in some years (see the high Cs maxima) and the occurrences of steppe (BSk) are also unharmed, so occasional droughts can be counted on. The different scenarios show these same changes but with different magnitudes, the most extreme is A1FI, and the least is B2. In A1FI, the strong presence of the Dfa+ (a class with cold winter and very hot summer) predicts extreme fluctuations of temperature in some years of the period.

The above discussed qualitative results coincide with the conclusions of IPCC for the future climate of Europe (*Alcamo et al.*, 2007). As the Köppen classification system is based on vegetation groups (*Peel et al.*, 2007), the results of this study can be used for various environmental, climatological, and agricultural purposes.

Also, a survey suggested that maps illustrating projected shifts of Köppen climatic zones are an effective visualization tool for disseminating climate change information (*Jylhä et al.*, 2010). Previous similar studies working on global (*Rubel* and *Kottek*, 2010) or continental (*Jylhä et al.*, 2010) scales give climate change information on relatively coarse spatial resolutions. For instance, an analysis of *Jylhä et al.* (2010) for Europe shows major future climate changes in the Iberian Peninsula, around the Black Sea and in the Alps. They found the regions with temperate (Cf, Cs) and dry climates (BW, BS) expanding. However, the entire area of Hungary is assigned here to Cfb class using data of the last five decades, and the projected future shifts of Köppen climatic zones are roughly represented as compared to our fine resolution approach. Also, presentation of extreme appearance of the different climate classes within the periods examined is an added product.

Since model generated values of meteorological variables are used to determine the climate classes, model output inaccuracies might result in climate class uncertainties. However, the applied classification methods are quite insensitive to deviations and errors (*Beck et al.*, 2006); see the threshold widths of the climate classes. Also, the raw model output is adjusted in the TYN 1.0 data set with a procedure reproducing much better the observed climate, and this procedure is then applied to model outputs corresponding to the future climate. This adjustment is expected to deliver more reliable model generated data (*Mitchell et al.*, 2004).

References

Alcamo, J., Moreno, J.M., Nováky, B., Bindi, M., Corobov, R., Devoy, R.J.N., Giannakopoulos, C., Martin, E., Olesen, J.E., and *Shvidenko, A.*, 2007: In *Climate Change 2007: Impacts, Adaptation and Vulnerability.* Contribution of Working Group II to the Fourth Assessment Report of the Intergovernmental Panel on Climate Change, Cambridge University Press, UK, 541-580.

Bartholy, J., Pongrácz, R., Torma, Cs., and *Hunyady, A*, 2006: *Modelling Regional Climates and Adapting the PRECIS Climate Model* (in Hungarian). Országos Meteorológiai Szolgálat, Budapest, pp. 228.

Bartholy, J., Pongrácz, R., Gelybó, Gy., and *Szabó, P.*, 2008: Analysis of expected climate change in the Carpathian Basin using the PRUDENCE results. *Időjárás 112*, 249-264.

Beck, C., Grieser, J., Kottek, M., Rubel, F., and *Rudolf, B.*, 2006: Characterizing global climate change by means of Köppen climate classification. *Klimastatusbericht KSB* 2005, 139-149.

Critchfield, H. J., 1983: *General Climatology*. 4th ed. Prentice Hall, 453 pp.

Gordon, C., Cooper, C., Senior, C.A., Banks, H., Gregory, J.M., Johns, T.C., Mitchell, J.F.B., and *Wood, R.A.*, 2000: The simulation of SST, sea ice extents and ocean heat transports in a version of the Hadley Centre coupled model without flux adjustments. *Clim. Dynam. 16,* 147-168.

IPCC, 2000: *Special Report on Emission Scenarios*. Cambridge University Press, UK, 570 pp.

Jylhä, K., Tuomenvirta, H., Ruosteenoja, K., Niemi-Hugaerts, H., Keisu, K., and *Karhu, J.A.*, 2010: Observed and projected future shifts of climatic zones in Europe, and their use to visualize climate change information. *Wea. Climate Soc. 2,* 148-167.

Kottek, M., Grieser, J., Beck, C., Rudolf, B., and *Rubel, F.*, 2006: World Map of Köppen-Geiger Classification Updated. *Meteorol. Z. 15*, 1-5.

Mitchell, T.D., Carter, T.R., Jones, P.D., Hulme, M., and *New, M.*, 2004: A comprehensive set of high-resolution grids of monthly climate for Europe and the globe: the observed record (1901–2000)

and 16 scenarios (2001–2100). *Tyndall Centre Working Paper No. 55.*, URL: *http://www.ipcc-data.org/docs/tyndall_working_papers_wp55.pdf.*

Peel, M.C., Finlayson, B.L., and *McMahon, T.A.*, 2007: Updated world map of the Köppen-Geiger climate classification. *Hydrol. Earth Syst. Sci. Discuss. 4,* 439–473.

Rubel, F. and *Kottek, M.*, 2010: Observed and projected shifts 1901–2100 depicted by world maps of Köppen-Geiger climate classification. *Meteorol. Z. 19,* 135-141.

Szalai, S., Konkolyné Bihari, Z., Lakatos, M., and *Szentimrey, T.*, 2005: *Some Characteristics of the Climate of Hungary from 1901* (in Hungarian). Országos Meteorológiai Szolgálat, Budapest.

Szépszó, G. and *Horányi, A.*, 2008: Transient simulation of the REMO regional climate model and its evaluation over Hungary. *Időjárás 112*, 203-231.

Appendix

The software group used for data processing consists of three common libraries (the koppen module for climate classification, the libgrid module for database processing, and the libtable module for producing climate maps and charts), a process program creating a sub-area including Hungary from the full dataset, and the clim program used to perform the analyses.

The koppen module's only function is clim(). This function is used to classify the climate of a year according to the Köppen system based on the given monthly mean temperatures and monthly precipitation totals, hemisphere (determining which months belong to winter and summer) and elevation data.

The functions of the libgrid module are the getdims() that reads the needed information from the headers of the data files, the degtogrid() that converts degree values to grid coordinates, and the getvals() that extracts the time series of the given grid boxes for the given dates.

The libtable module consists of countclims() creating the occurrence frequencies of the climates in a table, drawgrid() drawing a grid map using the values of the table, drawminmax() plotting the maximal and non-zero minimal area coverage data of all the climate classes in a given dataset. The Python Imaging Library and the CairoPlot module were used for drawing and plotting, respectively.

The process program creates a cut-out from the dataset according to the given geographical and temporal coordinates recorded in the configuration file hungary.conf, classifies the climates of all grid boxes in the cut-out, and saves them into a CSV data table. The difference between the process programs used for analyzing the observed and model generated datasets is that the program for the model data sets needs the name of the emission scenario (A1FI, A2, B1, B2) in command line argument; in addition, it indicates the scenario in the output file names.

The clim program uses the output files of the process. It draws the decadal mean climate maps, the spatial mean temperature graphs for the entire period, and the bar plots with the functions of the libtable. The program for the model generated datasets also needs the name of the emission scenario (A1FI, A2, B1, B2) in command line argument.

These programs are not actually available for public use, but development of their user friendly version is in progress.

IDŐJÁRÁS

Quarterly Journal of the Hungarian Meteorological Service
Vol. 114, No. 4, October–December 2010, pp. 263–273

Relation analysis between biomass and yield in maize seed production

Kálmán Kovács[1*], **Attila Csaba Dobos**[2], **Róbert Víg**[2], and **János Nagy**[2]

[1]*Federated Innovation and Knowledge Center,*
Budapest University of Technology and Economics,
Egry J. u. 18, bldg VI 526, H-1111 Budapest, Hungary; E-mail: kovacsk@mail.bme.hu

[2]*Centre for Agricultural and Applied Economic Sciences,*
Institute of Land Utilisation, Technology and Regional Development,
University of Debrecen,
Böszörményi út 138, H-4032 Debrecen, Hungary

[*]*Corresponding author*

(Manuscript received in final form November 3, 2010)

Abstract—The fact and volume of global warming in Hungary is proven by accurate meteorological measurements from the previous century. In agriculture and cultivation one should count with frequent changes of weather conditions due to climate change. Although the tendency of 0.6 °C raise in the annual average of temperature in the past one hundred years does not risk our cultivation so far, the high fluctuation of temperature, the winters, and the shorter transition seasons cause real problems. Similar potential threads are the decreasing trend of precipitation volume, the longer drought periods, and more frequent sudden heavy rainfalls. To provide a safe and well scheduled production, it is essential to maintain a decision support monitoring system based on up-to-date and accurate weather data. It is extraordinary needed in site-specific precision farming systems, where the aim is to produce goods of the highest quality. Nowadays, remote sensing is one of the basic instruments of continuous monitoring. Processing the collected data provides information for many fields of cultivation from technological parts to decision support processes.

The survey the vegetation state of plants, a measure can be calculated from remote sensing data, the so-called normalized vegetation index (NDVI).The aim of our research is to prove that satellite records can be a useful tool for maize seed production in two aspects: first, to find correlation between the NDVI and the weather conditions of a given year, and second, to find the optimal time interval for NDVI based crop estimation method.

Key-words: NDVI, yield estimation, climate change, remote sensing, crop of maize (*Zea mays L.*)

1. Introduction

To do successful cultivation, one should be aware of the interactions between the environmental factors and the cultivated plant as well as the crop fluctuations in time and space on account of these factors.

Hungary is on the edge of temperate continental climate with a high frequency of drought periods during the summer. The volume of precipitation, especially in the middle and southern parts of the country, decreased a rough 50 mm in the past 100 years, which is an extremely high degradation in respect to water needs. Meanwhile, the periods without precipitation have grown, and drought seasons have become more frequent (*Nagy*, 2006). Drought, as the most acute water shortage, can cause an economical catastrophe in cultivation. Fluctuation of precipitation in time and location is various in the territory of the country, thus periods and intensity of drought itself are also frequent. This aspect of the hypothetic climate change has a negative effect, extremely on the plants with high water needs. Further problems arise because of the sudden high volume falls (*Szász*, 2002). Naturally, the northern Great Plain region is not an exception either from climate change. Although the degradation of precipitation volume is rather timid, the annual average has declined 30–40 mm in the past 100 years. The question is how effective we are in eliminating the negative effects of climate change with irrigation, and what else we can do for this purpose.

Maize is a heat-sensitive field-corn, but the geographical edge of its potential of growing runs more and more to the north due to the result of plant breeding. The effective growing degree days (GDD) in Hungary are between 900 and 1500 °C, however, only maize hybrids between FAO 290 and FAO 540 maturity groups can be grown successfully (*Ángyán*, 1985). The minimum temperature of sprouting is 8–12 °C. If the soil temperature exceeds the minimum temperature of maize, the sprouting begins and its duration changes with regard to the ground temperature (*Keszthelyi*, 2005). The optimum temperature of shoot growth is 25–35 °C, therefore, maize can be grown in the most effective way where the average temperature of the hottest summer months is 21–27 °C. It needs an average temperature of 24–26 °C from detasseling period to the milk stage, however, in the period of pollen dispersal, too high temperature with meteorological drought can cause deficient fructification (*Shaw*, 1977 cit. *Turcsányi*, 1985). Maize is a good water utilizing plant, but it requires high quantity of water for intensive biomass production. The water need of maize is 420–440 mm in the growing season, but it can cope with a 250 mm lack of water compared to the optimum, since it can compensate the lack with the water stored in the ground, the groundwater, and the dew precipitation (*Bocz*, 1996). In Hungary, maize cultivation must cope with water shortages, as the difference between the water need of maize and the precipitation of the growing season is 40–150 mm on the maize croplands. The lack of water is the lowest (40–80 mm)

in the south-western Transdanubia, and the highest in the middle and southern parts of the Great Plain (100–150 mm) (*Nagy*, 2007).

2. *Material and methods*

2.1. Data acquired by on-site monitoring

On-site survey and monitoring were carried out in a systematic, cyclical way in the nearby maize seed producing area of Hajdúszoboszló between the years of 2004 and 2007. The net area of the agrarian fields was measured in the 2–3 leaf states of the vegetation, hence the not-sown fields (fallow fields, polders, etc.) were filtered out of further examinations. The homogeneous area samples, serving as the basis of the phenological observations, were chosen during the monitoring process. In the years of examination, 68 agrarian units were observed phenologically, twice a week on the average. The confinement of the fields was made by means of ProXH GPS and ArcPad x.x data collection softwares. The net area (the area covered with vegetation) was measured due to the unique cropping technology of the observed crop. The spatial uncertainty (2–5 m) was reduced by post-processing of the *.ssf files collected by the GPSCorrect-for-ArcPad auxiliary module. The accuracy was between 0.3 – 0.5 m.

2.2. Climatic data

The determination of climatic data was made by local measurements provided by the Hungarian Meteorological Service. Precipitation and conformation of global radiation and effective heat amount in the vegetative and generative periods were taken into consideration from the agrometeorological parameters. The GDD (1377–1660 °C) and average temperature (17.3 –18.7 °C) of the vegetative period in the years under examination proved to be optimal (*Table 1*).

Table 1. Climate characteristics of Hajdúszoboszló in the years of monitoring

	Favorable values	**2004**	**2005**	**2006**	**2007**
Growing degree days (GDD) (°C)	1250 – 1750	1377	1388	1442	1660
Average temperature of the growing season (°C)	16.8 – 19.0	17.5	17.3	17.6	18.7
Precipitation of the growing season (mm)	270 – 410	378	**455**	348	394
Precipitation of the winter term (mm)	230 – 310	**224**	**186**	237	151
Yearly precipitation (mm)	500 – 720	602	641	585	545
Heat unit – precipitation ratio (°C/mm)	1.9 – 3.1	2.3	2.2	2.5	3.0
Average humidity in July (%)	-	70.2	82.3	73.1	66.6

GDD are generally calculated by taking the average of the daily maximum and minimum temperatures compared to a base temperature, T_{base}. We note, that we used 8 temperature data measured by every 3 hours to improve the calculation of daily average, working with T_{base}=8 °C. The yearly precipitation amount fluctuated between 545 and 641 mm. The amount of precipitation in the growing season was optimal every year; however, the amount was low in the winter terms (151 and 224 mm) except the year of 2006. The heat unit–precipitation ratio (2.2–3.0 °C/mm) was in the optimum range in all the three years. The years 2006 (2.5 °C/mm) and 2007 (3.0 °C/mm) were dry, the years 2004 and 2005 (2.2–2.3 °C/mm) were wet for the maize on the basis of the heat unit–precipitation ratio.

In the period of pollen dispersal (July), the average humidity was pretty high (82.3%) in 2005, it was lower in the years of 2004 and 2006 (70.2% and 73.1%), and it was the lowest in 2007 (66.6%).

The monthly amount of precipitation was fairly diverse during the examination (*Fig. 1*):

- In 2004, the amount of precipitation of April, May, and September (40, 24, and 30 mm) was below, that of July (150 mm) was above the optimum value.
- In 2005, the amount of precipitation of June and July (64 and 68 mm) was below the optimal value; however, the quantity of all the other months exceeded its upper limit.
- In 2006, the sum of precipitation in June and August was above (84 and 82 mm) the upper limit of the optimum interval, but that of September was far below the lower limit.
- In 2007, April and June were featured by low precipitation (1 and 12 mm), while August and September were characterized by high precipitation (160 and 90 mm).

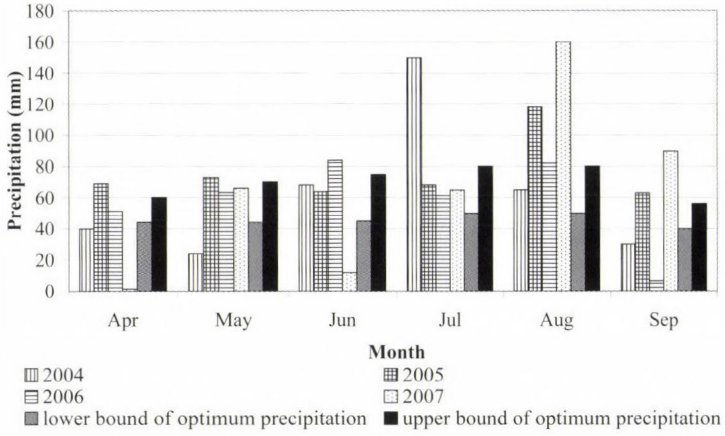

Fig. 1. Monthly amount of precipitation

2.3. Remote sensing data and method of evaluation

Landsat 5TM recordings transformed geometrically were provided by the Institute of Geodesy, Cartography and Remote Sensing, Budapest (see *Table 2*).

Table 2. Time of applied satellite recordings in the sample regions

Serial number of observation	2004	2005	2006	2007
1	May 3	May 31	May 11	May 21
2	June 20	June 16	June 26	June 22
3	July 22	July 25	July 12	July 15
4	August 23	August 10	August 22	August 16
5		September 4	September 14	

During quantitative analyses, information about the particular objects are the given radiation quantity of their characteristics as well as parameters and indicators calculated from them, thus we need to conduct the radiometric correction before processing data. COST model was used to make the atmospheric and radiometric correction (*Chavez*, 1996). In the model, firstly, radiance rates of the sensor have to be determined from the digital numerical values, then, in view of secondary data (zenith angle, Earth-Moon distance), the reference factor measured at the sensor can be calculated. During the correction process, the relief-deforming effect was ignored, since no significant difference was found in the altitudinal value of the territory examined. During pre-processing of the corrected recordings, thresholds of the cloudy area were defined based on the diffusion diagrams of the red channel, above which thresholds pixels have to be masked. Shades of the individual cloudy areas were picked in view of the particular areas.

2.4. Evaluation methodology

To survey the vegetation state of plants, the normalized vegetation index (NDVI) was calculated from the reflectance values of close infra and red channels (*Rouse et al.*, 1974). The possible instability in the NDVI values is accounted for the variance of field color (on surfaces with low vegetation) and humidity content, and also the most important climate attributes (precipitation, temperature, evapotranspiration, sunlight, and relative humidity). In the interval [–1,+1] the fields with healthy vegetation have their typical NDVI values between 0.2 and 0.8 (*Huete*, 1988), but on the spot, sampling and recordings are needed to evaluate the index values. Processing and evaluation using geographical information systems has been done using ArcGIS ArcInfo 9.1 and Erdas Imagine Professional 8.7 software environments.

The correlation between the NDVI and the heat unit is examined yearly, while the correlation between the NDVI and the yield has been further separated

to examination periods. For both cases regression analysis has been carried out. The correlation strength has been determined using the correlation coefficient R and determination coefficient R^2, and the validation of the regression model has been evaluated with the F-statistics of the variance of the estimations and residuals with a significance level of 5%. We have found correlation between NDVI and yield in every year but 2007. Statistical analysis is carried out using SPSS 13.0 program package.

3. *Results and discussion*

3.1. Evaluation of the correlation between the GDD and the NDVI

It is not possible to detect an unequivocal connection between growing seasons and calendar days. Instead of this, it is more suitable to choose the environmental parameter determining the growth of the crop. We have analyzed the change of the NDVI values depending on GDD.

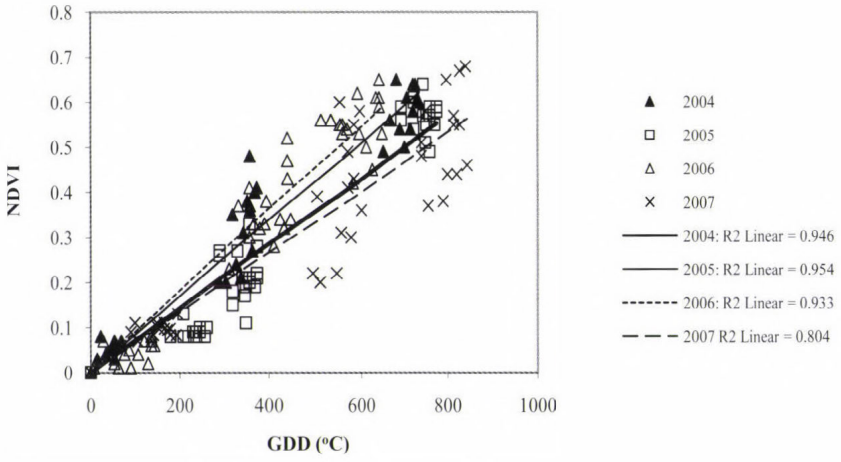

Fig. 2. Correlation between the GDD and the NDVI

The examination of the correlation between the GDD and the NDVI ended at the maximum point of the NDVI. It can be ascertained with the help of graphic trend analysis (*Fig. 2*), that the correlation between the GDD and the NDVI is positive in all the four years. The steepness of the trend lines changed yearly, it was the steepest in 2006, and the least steep in 2007. Examining the validity of the correlations between the GDD and the NDVI with regression analysis, a strong correlation for all the four years is obtained. The correlation coefficient was the largest in 2005 ($R = 0.977$), and the smallest in 2007

($R = 897$). The NDVI depended upon the GDD by 94.6 per cent in 2004 ($R^2 = 0.946$), 95.4 per cent in 2005 ($R^2 = 0.954$), 93.3 in 2006 ($R^2 = 0.933$), and 80.4 in 2007 ($R^2 = 0.804$) (*Table 3*). The variance of the residuals and the estimated values differed significantly in all the four years, so regressions are verifiable. The F-statistics has the biggest value in 2005 ($F = 1078$), and the smallest in 2007 ($F = 164$), i.e., the correlation between the GDD and the NDVI-index was the strongest in 2005.

Table 3. Results of the regression analysis between the GDD and the NDVI (R = correlation coefficient, R^2 = determining coefficient, F = F-statistics, *Sig* = significance, (*) = the variance of estimated and residual values differs on a 5% level of significance)

Year	*R*	R^2	*F*	*Sig*
2004	0.973	0.946	648.007	0.000 (*)
2005	0.977	0.954	1078.400	0.000 (*)
2006	0.966	0.933	630.197	0.000 (*)
2007	0.897	0.804	163.792	0.000 (*)

3.2. Evaluation of the correlation between the NDVI and the yield (t/ha)

On the basis of the graphic trend analysis (*Fig. 3*), the correlation was positive in all the seven cases, i.e., the yields increased with the growth of the NDVI. The correlation between the NDVI and the yield was most significant in the fourth observation time in 2004, in the third and fourth in 2005, and in the third in 2006. The steepness of the trend lines changed yearly and with observation times; it was the steepest in the third observation time in 2006.

From *Table 4* it can be seen that in 2004, observations 1 and 2 showed weak correlation ($R = 0.199$ and 0.287) between the NDVI and the yield, stronger ($R = 0.330$) for observation 3, but the strongest ($R = 0.687$) for observation 4. The values of the F-statistics showed significant and real correlation (*Sig* = 0.009) only for observation 4, while the values are higher than the chosen significance level (0.05) for the other ones. In our tables we detail the results for observations with significant correlation (for example in *Table 4* for observation 4). In observation 4, 47.2% ($R^2 = 0.472$) of the yield is described by the NDVI, and based on the standard error of estimation ($SEE = 1.01$) it can be estimated with an accuracy of 1.01 t/ha. The regression coefficient significantly ($Sig = 0.009$) differs from zero, whereas the regression constant does not ($Sig = 0.405$), therefore, the regression equation is $Y = 10.178 \cdot X$, where Y is the estimated yield and X is the NDVI value.

In 2005, the correlation coefficient is rather small for the first two observations ($R = 0.222$ and 0.067) but stronger for observations 3, 4, and 5 ($R = 0.638$, 0.673, and 0.410). The variance of the estimated values and residuals differed significantly from zero only for observations 3 and 4 ($Sig = 0.004$ and

0.002). In observation 3, the 40.7% of the yield is described by the NDVI, and it can be estimated with an accuracy of 0.98 t/ha (see *Table 5*). The slope and the regression coefficient significantly differ from zero, thus we can accept that the regression equation $Y = 22.477 \cdot X - 9.649$ is valid. In observation 4, the 45.3% of the yield is described by the NDVI with an accuracy of 0.94 t/ha. The regression equation is $Y = 23.479 \cdot X - 10.221$.

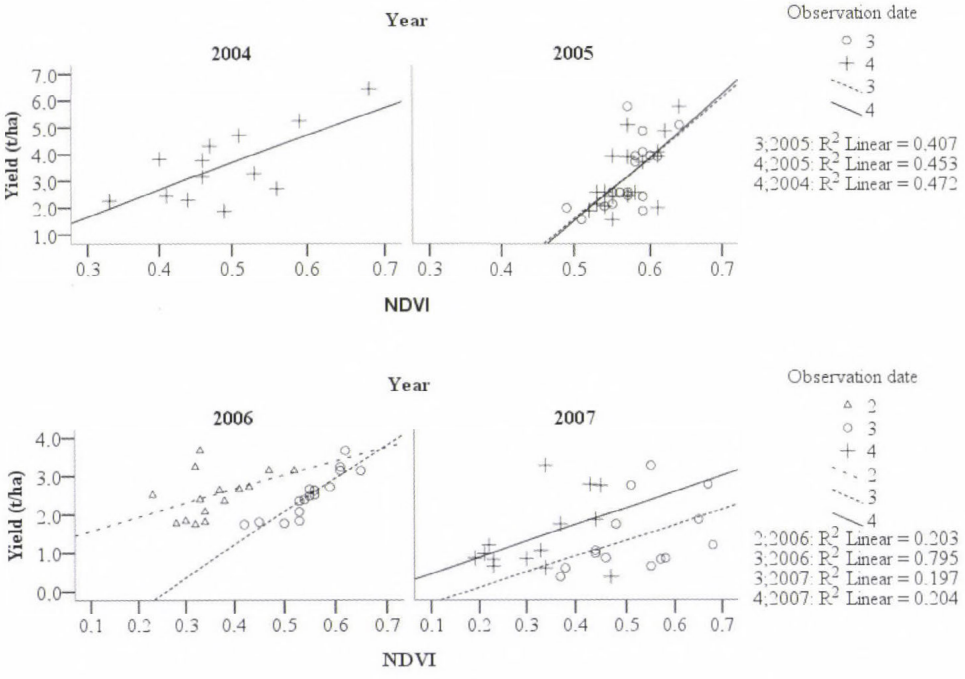

Fig. 3. Correlation between the NDVI and the yield (2004–2007)

Table 4. Regression analysis table between the NDVI and the yield (t/ha) for the year 2004 (*B* = non-standardized coefficient, *SE* = standard error, *T* = t-statistics)

Observation date	***R***	***R²***	***SEE***	***F***	***Sig***
1	0.199	0.039	-	0.451	0.516
2	0.287	0.082	-	0.985	0.342
3	0.330	0.109	-	1.344	0.271
4	0.687	0.472	1.01	9.827	0.009 (*)
Observation 4		***B***	***SE***	***T***	***Sig***
Regression constant (slope)		-1.390	1.606	-0.866	0.405
Regression coefficient		10.178	3.247	3.135	0.009

Table 5. Regression analysis table between the NDVI and the yield (t/ha) for the year 2005

Observation date	***R***	R^2	***SEE***	***F***	***Sig***
1	0.222	0.049	-	0.829	0.376
2	0.067	0.004	-	0.071	0.793
3	0.638	0.407	0.98	10.986	0.004 (*)
4	0.673	0.453	0.94	13.233	0.002 (*)
5	0.410	0.168	-	3.230	0.091
Observation 3		***B***	***SE***	***T***	***Sig***
Regression constant (slope)		-9.649	3.88	-2.487	0.024
Regression coefficient		22.477	6.781	3.314	0.004
Observation 4		***B***	***SE***	***T***	***Sig***
Regression constant (slope)		-10.221	3.693	-2.768	0.014
Regression coefficient		23.479	6.454	3.638	0.002

In 2006, observations 1, 4, and 5 show weak correlation ($R=0.186$, 0.219, and 0.237) between the NDVI and the yield, stronger ($R=0.451$) for observation 2, but the strongest ($R=0.892$) for observation 3 (see *Table 6)*. The values of the F-statistics showed significant and real correlation only for observation 3, while the values are higher than the chosen significance level for all the other ones. In observation 3, 79.5% of the yield is described by the NDVI and it can be estimated with an error of 0.27 t/ha. The slope and the regression coefficient significantly differ from zero, thus we can accept that the regression equation $Y=8.625\cdot X-2.232$ is valid.

Table 6. Regression analysis table between the NDVI and the yield (t/ha) for the year 2006

Observation date	***R***	R^2	***SEE***	***F***	***Sig***
1	0.186	0.035	-	0.502	0.490
2	0.451	0.203	-	3.314	0.092
3	0.892	0.795	0.27	54.336	0.000 (*)
4	0.219	0.048	-	0.654	0.433
5	0.237	0.056	-	0.836	0.376
Observation 4		***B***	***SE***	***T***	***Sig***
Regression constant (slope)		-2.232	0.647	-3.448	0.004
Regression coefficient		8.625	1.170	7.371	0.000

In 2007, observations 1 and 2 show weak correlation ($R=0.078$ and 0.244) between the NDVI and the yield, while stronger ($R=0.444$ and 0.452) for observations 3 and 4. The variance of the estimated values and residuals does

not differ significantly in either case, so no evidence for the correlation between NDVI and the yield from 2007 has been found (*Table 7*).

Table 7. Regression analysis table between the NDVI and the yield (t/ha) for the year 2007

Observation date	R	R^2	F	*Sig*
1	0.078	0.006	0.073	0.792
2	0.244	0.060	0.762	0.400
3	0.444	0.197	2.942	0.112
4	0.452	0.204	3.073	0.105

In *Table 8* we can see that the standard variation of the yield was the smallest (0.226) in 2006, higher in 2004 and 2005 (0.364 and 0.379 respectively), and the highest (0.632) in 2007 saying that the crop was the most homogenous in 2006 and the least homogenous in 2007. According to the investigations, the higher the standardized deviation the weaker the correlation between the NDVI and the yield. In 2007, the low yield and the heterogeneity of it can be explained by a drought period and high temperature during blooming that caused low fertility.

Table 8. The standard variation of the yield and the correlation between the NDVI and the yield

Year	Standard variation	R^2
2006	0.226	0.892
2005	0.379	0.673
2004	0.364	0.687
2007	0.632	0.452

4. Conclusions

It has been shown that estimating plant growth using satellite records can be applied in a new field, namely in maize seed production. Estimated production results of crop fields were derived from processed data. During growing season, especially at blooming, one can examine the heterogeneity and the fertility of crop mass using the files provided. Applying the method for longer time series, the most suitable fields for crop production and high productivity cultures can be identified with high probability. Providing exact information quickly has become a basic requirement of reliable agricultural production. Data collected by remote sensing provides information that can be used widely in cultivation both in the technological and decision support processes areas. The technologies in industrial processing require constant quality of input goods. It is essential to

set up and improve the monitoring system of production (optimal selection of fields, yield estimation, and effective identification of negative processes during plantation growth).

Acknowledgements—This work is connected to the scientific program of the "Development of quality-oriented and harmonized R+D+I strategy and functional model at BME" project. This project is supported by the New Hungary Development Plan (Project ID: TÁMOP-4.2.1/B-09/1/KMR-2010-0002).

References

Ángyán, J., 1985: Mass production forage maize production – Geographical location of maize production (in Hungarian). In *A kukoricatermesztés kézikönyve* (ed.: *Z. Menyhért*). Mezőgazdasági Kiadó, Budapest, 199-228.

Bocz, E., 1996: Maize – Climatic requirements, soil requirements, soil tillage, crop rotation (in Hungarian). In *Szántóföldi növénytermesztés* (eds.: *E. Bocz, I. Késmárki, A. Kováts, L. Ruzsányi, M. Szabó*). Mezőgazdasági Kiadó, Budapest, 379-387.

Chavez, P.S., 1996: Image-based atmospheric corrections – Revisited and improved. *Photogrammetric Engineering and Remote Sensing 62*, 1025-1036.

Huete, A.R., 1988: A soil-adjusted vegetation index (SAVI). *Remote Sens. Environ. 25*, 295-309.

Keszthelyi, S., 2005: Effect of the climatic factors of year 2004 on the development of maize, and the appearance of its pests and their damage (in Hungarian). *Agrofórum 16*, 10, 3-7.

Nagy, J., 2006: Multifunctional agriculture (in Hungarian) In *Területfejlesztés, agrárium és regionalitás Magyarországon* (eds.: *B. Baranyi, J. Nagy*). DE-AMTC & MTA-RKK, Debrecen, 191-206.

Nagy, J., 2007: *Maize Production* (in Hungarian) *Kukoricatermesztés*. Akadémiai Kiadó, Budapest.

Rouse, J.W., Haas, R.H., Schell, J.A., 1974: Monitoring vegetation systems in the Great Plains with ERTS. In *Third Earth Resources Technology Satellite-1 Symposium.* December 10-14, 1973, NASA SP-351, Washington, D.C. (eds.: *S.C. Freden, E.P. Mercanti, M.A. Becker*). NASA STIO, Goddard SFC and Washington, D.C., 309-317.

Szász, G., 2002: Utilization of climatic natural resources in domestic crop production (in Hungarian). *Agrártudományi Közlemények – Acta Agraria Debreceniensis 9*, 101-106.

Turcsányi, G., 1985: Maize morphology, histology and physiology – Maize physiology (in Hungarian). In *A kukoricatermesztés kézikönyve* (ed.: *Z. Menyhért*). Mezőgazdasági Kiadó, Budapest, 58-76.

IDŐJÁRÁS

Quarterly Journal of the Hungarian Meteorological Service
Vol. 114, No. 4, October–December 2010, pp. 275–286

Ensemble calibration of ECMWF's medium-range forecasts

István Ihász[1*], **Zoltán Üveges**[1], **Máté Mile**[1], and **Csilla Németh**[2]

[1]*Hungarian Meteorological Service,*
P.O. Box 38, H-1525 Budapest, Hungary; E-mail: ihasz.i@met.hu

[2]*Department of Meteorology, Eötvös Loránd University,*
P.O. Box 32, H-1518 Budapest, Hungary; E-mail: csidori@gmail.com

[*]*Corresponding author*

(Manuscript received in final form November 4, 2010)

Abstract — A post-processing method is presented, that is aimed at enhancing the value of ensemble forecasts through ensemble calibration. This approach can reduce model errors. In March 2008, ECMWF introduced the VarEPS/Monthly system. Part of this service provides a weekly reforecast dataset for the last 18 years. This dataset has been successfully applied for ensemble calibration at the Hungarian Meteorological Service. The calibration was performed for surface meteorological variables such as 2m temperature, minimum and maximum temperature, 10m wind speed, and daily precipitation. An objective verification was performed on the basis of several deterministic and ensemble verification scores. The calibration method was introduced operationally in mid-2009.

Key-words: ensemble calibration, medium–range weather forecasts, reforecast dataset, model climate, ensemble verification

1. Introduction

The ECMWF, established by 18 European countries in 1973, is the world leader of numerical weather prediction providing highly reliable medium-range forecasts. In 1994, Hungary was the first Eastern European country to sign a co-operation agreement with the ECMWF (*Woods*, 2006) and the Hungarian Meteorological Service (HMS) has been using the full set of operational forecasts ever since. In the last 15 years, the HMS made several local developments to provide additional tools for forecasters and users to help decision making and improving the quality of the forecasts, especially in

medium-range and extended medium-range scales (*Ihász*, 2008). In this paper a new development, the so-called ensemble calibration post-processing method is presented.

Calibration of ensemble forecasts is a new challenge in meteorology (*Hamill* and *Whitaker*, 2007), and in most cases, different techniques are used for different types of meteorological variables depending on their probability distribution. Even though a number of derived ensemble products (e.g., forecast probabilities) are provided directly by the ECMWF, its Member States are encouraged to make local developments. Therefore, since 2008 reforecast products have been available for calibration purposes (*Hagedorn*, 2008), whilst the calibration itself is not performed by the ECMWF. We have successfully applied a simple calibration method for several meteorological variables such as 2m temperature, daily precipitation, 10m wind speed, which have completely different distribution functions. The method and the verification results are presented in Sections 2, 3, and 4 of this paper. This method was introduced operationally in the second part of 2009 at the HMS.

2. Calibration of ensemble forecasts

Although numerical forecasting models have gone under huge development, their raw forecasts still contain errors stemming from a wide range of sources. The influence of these errors can be reduced to some extent by post-processing methods. In this part of the paper, a quite simple but effecient calibration method will be shown. This method has been developed and applied at the Hungarian Meteorological Service in order to make ECWMF's medium-range ensemble forecasts more reliable.

At first we take a deeper look into the general procedure of calibration, which is based on the comparison of statistical distributions of the model variables and observations. In the second part, deep investigations will be presented on the distribution functions of model forecasts in order to size up the model's behavior in case of different meteorological parameters. Then we will try to demonstrate the effectiveness of calibration by representing a couple of examples of calibrated and verified model results as well as a case study.

3. Method of the calibration

As it was mentioned above, the chosen calibration method is based on the comparison of empirical distribution functions. Thus, the adequate construction method and data quality of these functions have primary importance.

The classical and the most simple method is to create a model climate using ensemble forecasts of the past couple of years. As a matter of fact, the model climate is a collection of forecasts with start and prediction dates from the past,

containing data for a considerable number of years (*Hamill* and *Whitaker*, 2007; *Hagedorn*, 2008).

However, it is important to note that there are always some differences between past and recent behavior of the model due to model developments. To avoid difficulties caused by this fact, reforecast datasets can be generated operationally at the largest centers (*Hagedorn*, 2008). Let us see a short summary of the model climates generated at the ECMWF.

The necessity of generating and using a set of runs to define the model climate was addressed more than fifteen years ago. Firstly, the reanalysis projects provided model climates. At the ECMWF, the ERA-15 (*Gibson et al.*, 1997), ERA-40 (*Uppala et al.*, 2005), and ERA-Interim (*Simmons et al.*, 2007) products provided model climate for the deterministic model, but they were not relevant for ensemble forecasts. In the beginning of the first decade of the 21st century, a new product, the Extreme Forecast Index (EFI) was developed (*Lalaurette* and *Grijn*, 2003), which also needed model climate. The first version of EFI used the classical method for generating model climate between the late 2003 and early 2006. In November 2006, daily operational forecasts were extended from 10 to 15 days by the introduction of the VarEPS system (*Buizza et al.*, 2006). Between 2006 and 2008, the model climate was operationally generated daily, by running a reforecast of the control model of ensemble system only up to +48 hours for the period of 1971–2000. This was the first model climate that was adequate enough to be used for calibration purposes. By the middle of March 2008 VarEPS was merged with the former monthly forecast. At the same time, a new reforecast method was introduced, i.e., a 5-member ensemble reforecast dataset was operationally produced weekly for the last 18 years (*Hagedorn*, 2008). To increase the representativeness, the distributions of model climates can be generated from 5 consecutive weekly reforecast datasets that can be obtained from ECMWF's Meteorological Archival and Retrieval System (MARS) (*Raoult*, 2001).

Hagedorn (2008) proved the usefulness of calibration for 2m temperature, and this encouraged the members to develop and apply calibration procedures for their local needs. *Hagedorn* (2008) used non-homogeneous Gaussian regression method (*Hamill* and *Whitaker*, 2007) based on daily values of archived observations and model variables. Verification results showed that the success of calibration is partly originated from simple bias correction, but additional improvements could be achieved by ensemble calibration. The 2m temperature ensemble forecast was calibrated for 250 European stations. A verification measure, the continuous rank probability score (CRPS) showed that calibrated EPS forecasts for day 4 are as good as uncalibrated forecasts for day 1. The disadvantage of this method is that it can only be used for meteorological variables, which have Gaussian distribution. Another type of calibration method must be applied for non-Gaussian meteorological variables, e.g., precipitation (*Hamill et al.*, 2007).

Since national meteorological services have real-time access to data coming from the most dense network of reliable observations, the best approach is to make calibration at the national level. Beside the model climate, a reliable observed climate is also needed for successful calibration which can be provided by the national meteorological services. It has been noticed that it is essential to match the reference interval of the model and observed climates since different reference intervals. Serious inaccuracies can be caused in calibrated forecasts as a result of slight climate changes. Model climate can be locally calculated at meteorological services with the most appropriate method for their local needs.

In the beginnings of 2007, HMS decided to develop a calibration algorithm for EPS forecasts, to test and verify the system as well. In the first stage of the work, model climate was created from the +48-hour reforecasts of the control model, for the period of 1971-2000 *(Ihász*, 2007; *Ihász* and *Mile*, 2008). Forecast calibration was aimed only between +24 and +120 hours (*Mile*, 2008a, 2008b). The calibrations were made on five meteorological parameters: 2m minimum and maximum temperatures, 2m temperature at 12 UTC, daily accumulated precipitation, 10m wind speed at 12 UTC. Nine reliable Hungarian synoptical stations (Békéscsaba, Budapest, Miskolc, Nagykanizsa, Nyíregyháza, Pécs, Siófok, Szeged, and Szombathely) were selected for the investigations.

It has been mentioned that in the middle of March 2008, a brand new EPS system was launched. In addition, a new model climate with totally different properties (such as reference interval, number of ensemble members, forecast period, etc.) became available. It was worth to include products of the new reforecast system into our calibration process.

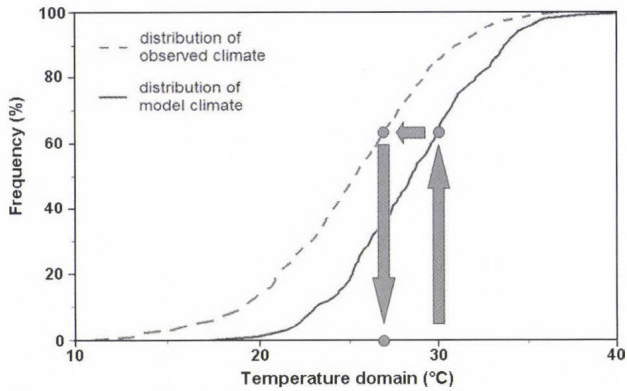

Fig. 1. Example of calibration method.

To understand our calibration method itself, procedure is illustrated in *Fig. 1.* Suppose that one of our ensemble members predicts a temperature of 30 °C. Firstly, we have to find the frequency in the model climate that belongs to the value of 30 °C. Then, this frequency must be projected onto the observed

climate. And finally, we get a value belonging to this frequency which is the new value of our ensemble member. As a matter of fact, we assume that the distribution of observed values describes weather conditions more accurately in a given place than the distribution of values forecasted by a numerical model. Thus, instead of a simple shifting of the curve of distribution functions, like in case of bias correction, we look for the frequency of each EPS value both in the model- and observed climates.

4. Comparison of modeled and observed climate distributions

Before calibrating forecasts, deeper investigations were made on the model climates in order to scale the model's behavior in case of different parameters.

4.1. Comparison of recent and former model climates

The model climates were compared (the recent one having a reference interval of 1990–2007 and the former one with an interval of 1971–2000) so that the climate changes as well as the differences between model versions could be found (*Üveges*, 2009a, 2009b). It can be clearly seen that the difference is in some cases is greater than 1.5 °C.

4.2. Comparison of model climate and observations

In the following part of the investigation, the systematic errors of the model could be demonstrated by comparing the model climate with observations at synoptic stations. All of the graphs were made from reforecast climates with a time step of 180 hours and from the corresponding observated climates. The left side of *Fig. 2* shows an example for distribution of daily precipitation.

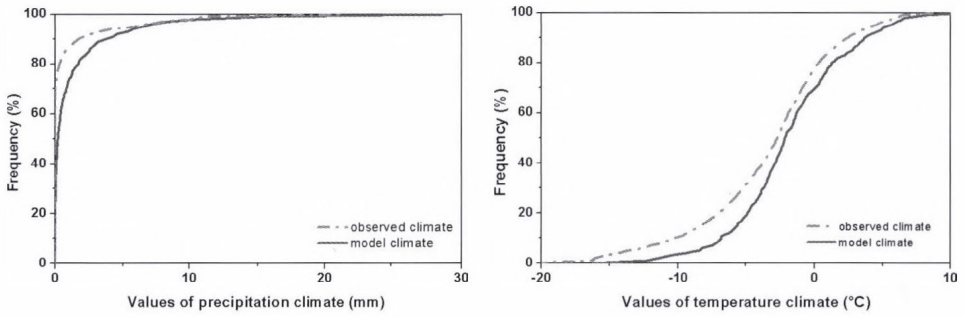

Fig. 2. Monthly distributions of 24-hour precipitation for Szombathely in January (left) and monthly distributions of daily minimum temperature for Nagykanizsa in January (right).

Overestimation can be observed in daily precipitation in January in the case of Szombathely, a town near the Austrian border at the foot of the Alps. In summer, the model climate is colder than the observed one. This difference may be caused by convective precipitation. Lowest temperatures can be seriously affected by local conditions which cause significant systematic errors in the forecasts (see the curves showed on the right side of *Fig. 2*).

5. Comprehensive verification of uncalibrated and calibrated ensemble forecasts

A wide range of methods is available for ensemble verification (*Persson* and *Grazzini*, 2007). During our investigation, the reliability diagram, ROC diagram, Brier (skill) score, and calculation of outliers were used.

Since the monthly ensemble forecasts are produced only once a week, and during our study they were available altogether from April 2008 till March 2009, the amount of forecast values was insufficient to get reliable verification results in some cases. Thus, only 15-day forecasts were verified and joint verification was made.

5.1. 2m temperature at 12 UTC

The first calibrated and verified parameter is temperature at 12 UTC. The results are displayed among others in Talagrand diagrams, which provide useful information about the relationship of ensemble spread and observations. In uncalibrated cases, J-shape diagrams can be seen on both graphs caused by accumulation of the observed values in the lower temperature domain (*Fig. 3*). Thus, the ensemble system makes a constant overestimation of temperature at 12 UTC. In the case of calibrated forecasts, the distributions of observations are much flatter, i.e., the calibration managed to reduce the error discussed above.

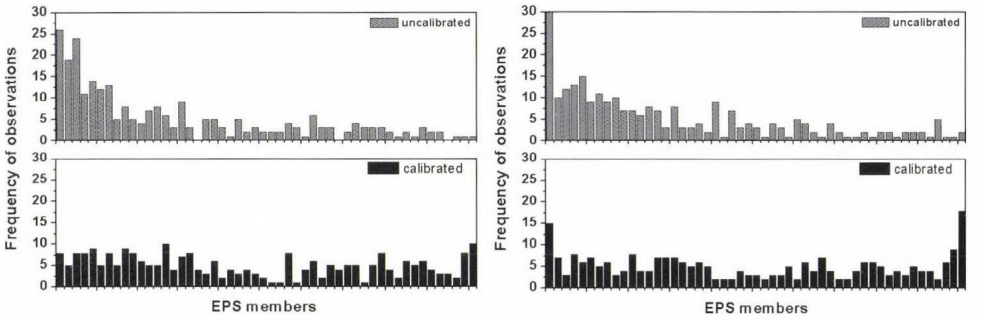

Fig. 3. Talagrand diagrams of 2m temperature forecasts at 12 UTC for Miskolc (left) and Siófok (right).

5.2. *Daily maximum temperature*

Probabilistic forecasts can be transformed into a categorical yes/no forecast defined by some probability thresholds as well as meteorological events. For different thresholds the corresponding hit rates and false alarm rates can be computed. A very powerful way to display and interpret this information is the two-dimensional relative operating characteristics or ROC diagram. A point in the ROC diagram is defined with the POFD (or False Alarm rate) on the x-axis and POD (or HR) value on the y-axis. The upper left corner of the ROC diagram represents a perfect forecast system where there are no false alarms and only hits. The closer the point is to this upper left corner the higher the skill is. The lower left corner, where both hit and false alarm rates are zero, represents a system which never warns of a predefined event.

Although many kinds of verification methods have been tried, maximum temperature is the only parameter for which no significant improvement has been observed.

5.3. *Daily minimum temperature*

One of the best methods for displaying the verification results of an ensembe forecast is making reliability diagrams. They are simple graphs of the observation frequency (y-axis) of an event against the forecast probability of the same event (x-axis). This graph effectively tells how often a forecast probability actually occurred. In a perfect forecast system, for example, a meteorological event forecasted with a probability of 10%, should occur one out of 10 times. The curves of the graph connect the intersections of probabilities and the corresponding observation frequencies. Thus, in case of a reliable ensemble forecast system, the curves have low deviation from the diagonal of the graph box. One of the predefined events was the minimum temperature value exceeding 5 °C. The results for two locations are displayed in *Fig 4.*

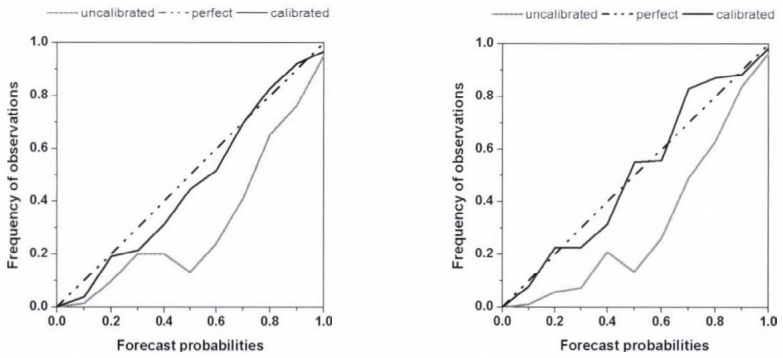

Fig. 4. Reliability diagrams of daily minimum temperature forecasts for Budapest (left) and Siófok (right).

In both cases, uncalibrated forecasts show serious overestimation of the event. However, the calibrated forecasts illustrated with red lines are much closer to the diagonal, which means that the calibration resulted in much more reliable forecasts. The synoptic station of Siófok is located on the shore of the Lake Balaton, the other one in Budapest is located in a quite dense urban area. It seems like the local conditions are taken into account more precisely in the case of the calibrated forecasts.

5.4. Daily precipitation

As it is well known, precipitation is much more variable in space and time than temperature. Precipitation is a non-continuous meteorological variable, therefore, making a successful forecast and verification is quite challenging, especially in summer, when convection can be quite intense.

Brier skill scores (BSS) were calculated for verifying precipitation forecasts. If BSS equals 1, the forecast is perfect. If it equals 0, the forecast has no skill compared to a reference forecast, in this case to the uncalibrated forecast. In case of negative BSS values, the examined forecast is worse then the reference. The defined meteorological event was the occurence of daily precipitation greater than 1 mm. As we saw at the examples of systematic errors, EPS forecasts are likely to overestimate the amount and frequency of precipitation. Since positive BSS values can be seen on the graphs in all cases, the calibration process reduced the error (*Fig 5*).

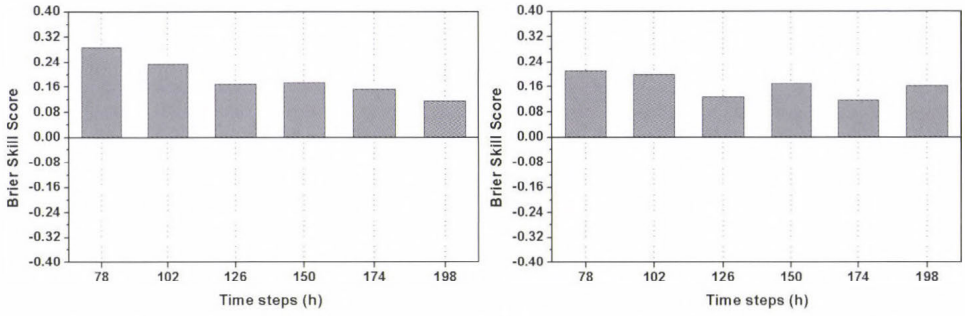

Fig. 5. Computed BSS values of daily precipitation forecasts for Pécs (left) and Szeged (right).

5.5. 10m average wind speed at 12 UTC

The surface wind speed strongly depends on surface conditions. For this variable, calibrated wind speed forecasts showed the greatest improvement. This is demonstrated by the graphs displaying mean square error (MSE) values. MSE is the squared deviation of a forecast value from the observation.

Reduction in MSE values of wind forecasts were more succesful where the surface conditions are highly variable. The ensemble forecast of ECMWF takes into account the mountains and hills to an unsufficient extent because of its horizontal resolution. This is the reason for the big improvement of the forecasts at Miskolc at the foot of the Northern Mountains (*Fig. 6*). On the contrary, calibration has hardly any effect in Nyíregyháza, which is located in the Great Plain.

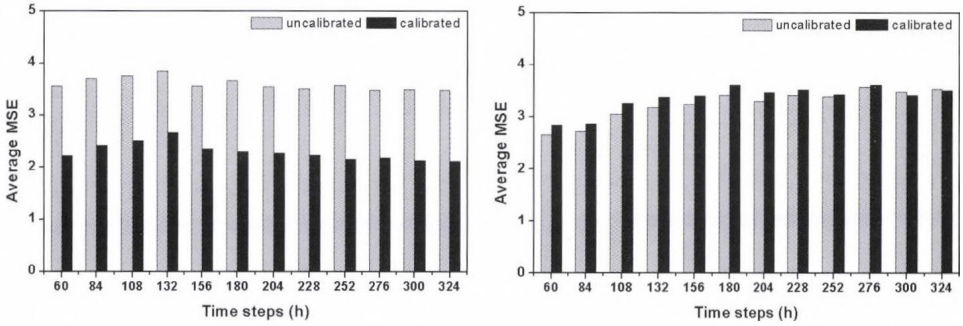

Fig. 6. MSE values of the 10m average wind speed forecasts at 12 UTC for Miskolc (left) and Nyíregyháza (right).

5.6. Case study

Case studies were also made in order to prove the effectivenes of calibration. At the beginning of 2009, a strong and stable inversion layer developed over the Carpathian Basin. Consequently, the air pollution became more and more critical during the period, and the mayor of Budapest had to issue a smog alert in the city. It can be clearly seen in *Fig. 7*, that the observations marked with red points are located much closer to the ensemble mean in the case of calibrated forecasts, i.e., if the process of calibration had been used operationally at the HMS, much better wind speed forecast could have been done for the critical period.

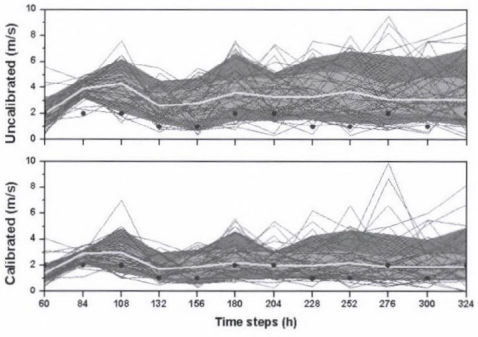

Fig. 7. EPS plumes of the 10m average wind speed forecasts at 12 UTC, January 1, 2009, in Budapest.

5.7. Grid based calibration

After having encouraging verification results concerning to the selected synoptical stations, it was considered to extend calibration for the regular 0.5 by 0.5 degrees grid belonging to EPS model resolution valid in 2009. The area of the country is 93,030 km^2, it is covered by approximately 70 grid points, so 70 stations were selected for providing 'observed' climate distributions for all grid points.

The largest part of the country is flat, while in the mountainous regions the observation density is not completely enough for providing perfect interpolation for ensemble grid, therefore, the observed climate distribution of each gridpoints is represented by distribution of the closest observation. The method of the calibration was exactly the same as in case of station based calibration. An important advantage of the grid based calibration is that uncalibrated and calibrated meteorological fields can be easily visualized, and local forecasts can be easily derived for end users.

Firstly, the 2m temperature was chosen to test the new grid based calibration, because this variable is quite sensitive to the influence of the orography (*Németh*, 2010). Verification of calibration was made for 2009. Calculation of the monthly mean of raw and calibrated ensemble forecasts in addition to observed values was made for each month of 2009. Maps belonging to each month showed that calibration forecasts are definitely closer to the reality, especially in the mountainous regions (*Fig. 8*).

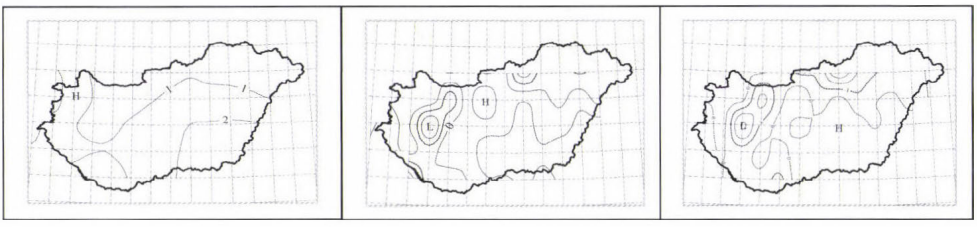

Fig. 8. Monthly mean chart of raw (left), calibrated (middle), and observed (right) values for Hungary in January 2009.

Mean error and root mean square error maps were also made between the raw and observed values beside the calibrated and observed values. Finally, outlier maps were used to clearly show the regions where under or overestimation appeared.

The ensemble spread was found not sufficiently wide at lower time steps, it was good just after an approximately 3-day lead time. At all time steps between +12 and +180 hours, critical mountainous regions show systematic overestimation of the uncalibrated forecast, that could be eliminated well by calibration.

To demonstrate that ensemble calibration could particularly improve the forecast in mountainous regions. a grid point was chosen in the area in Bakony hill in the transdanubian region. It can be clearly seen that calibration successfully eliminates the systematic error (*Fig. 9*).

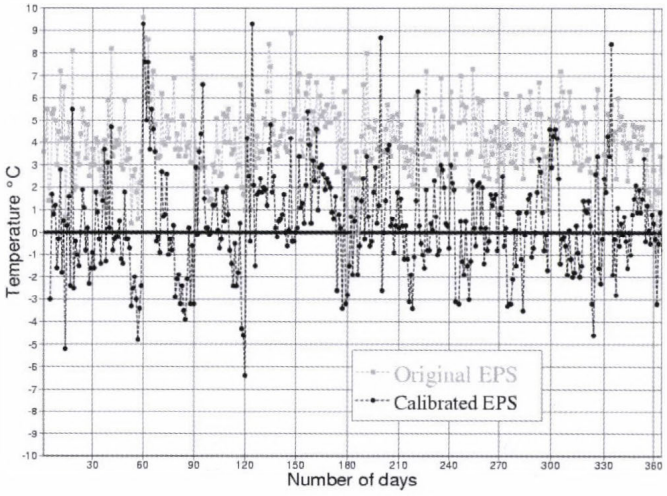

Fig. 9. Time series of forecasted 12 UTC temperature based on raw (red) and calibrated (green) temperature at a selected mountainous grid point (47.0° N, 17.5° E).

6. Summary, conclusions

In this paper, a calibration method developed and used at HMS for post-processing of ensemble forecasts was presented. It has been shown that the method significantly improves the forecast efficiency on regional and local scales. This method was intensively investigated and verified for five important meteorological variables: 2m temperature, daily minimum and maximum temperatures, daily precipitation, and 10m average wind speed.

In the new calibration system, a new type of reforecast datasets was used. The model climate based on 5 member EPS reforecasts was compared to an older one and the observed climate as well, in order to examine the special characteristics over the territory of Hungary. Verification of calibrated forecasts shows that in most cases the calibrated products are more skillful than the raw forecasts.

Acknowledgements — Authors are very grateful to *László Hercsényi*, *Rita Hodossy,* and *Zsuzsa Kövér* for kindly providing the monthly observed distribution dataset by Software Development Division of Telecommunication and Informatics Department. We also thank *Gábor Radnóti* and *Miklós Vörös* for useful suggestions and comments on work and reviewing the manuscript. This work was partly supported by the Hungarian National Office for Research and Technology (NKFP, grant No. 3A/051/2004).

References

Buizza, R., Bidlot, J-R., Wedi, N., Fuentes, M., Hamrud, M., Holt, G., Palmer, T., Vitart, R., 2006: The ECMWF Variable Resolution Ensemble System (VAREPS). *ECMWF Newsletter 108,* 14-20.

Gibson, J.K., Kallberg, P., Uppala, S., Hernandez, A.., Nomura, A. and *Serrano, E.,* 1997: ERA-15 description. *ERA-15 Project series 1.* ECMWF.

Hamill, T.M. and *Whitaker, J.S.,* 2007: Ensemble calibration of 500 hPa geopotential height and 850 hPa and 2-metre temperature using reforecasts. *Mon. Weaather Rev. 135,* 3273-3280.

Hamill, T.M., Hagedorm, R. and *Whitaker, J.S.,* 2007: Probalistic Forecast Calibration: Using ECMWF and GFS Ensemble Reforecasts. Part II: Precipitation. *Mon. Weather Rev. 135,* 2620-2632.

Hagedorn, R., 2008: Using the ECMWF reforecast dataset to calibrate EPS forecasts. *ECMWF Newsletter 117,* 8-13.

Ihász, I., 2007: Experiences using VarEPS products at the Hungarian Meteorological Service. *Proceedings of the Eleventh ECMWF Workshop on Meteorological Operational Systems.* Reading, UK, 14-18 November 2007, 130-135.

Ihász, I. and *Mile, M.,* 2008: Calibration of ECMWF ensemble precipitation forecasts for hydrological purposes at the Hungarian Meteorological Service. *Proceedings of the XXIV Conference of the Danubian Countries.* 2-4 June 2008, Bled, Slovenia.

Ihász, I., 2008: Model products of medium and long range forecasts and possibilities for applications (in Hungarian). *Proceedings of 34th Scientific Meteorological Days at Hungarian Scientific Academy,* 20-21 November 2008. Budapest, Hungary.

Lalaurette, F. and *van der Grijn, G.,* 2003: Ensemble forecasts: Can they provide useful early warnings? *ECMWF Newsletter 96,* 10-18.

Mile, M., 2008a: Subsequently calibration of ensemble forecasts of the ECMWF (in Hungarian). *Proceedings of the Scientific Student Conference on Environment.* 25-26 March 2008, Nyíregyháza, Hungary.

Mile, M., 2008b: Subsequently calibration of ensemble forecasts of the ECMWF (in Hungarian). *Master Thesis,* Eötvös Loránd University, Budapest, Hungary.

Németh, Cs, 2010: Verification of the calibrated probability forecasts of ECMWF's ensemble model (in Hungarian). *BSc Thesis,* Eötvös Loránd University, Budapest, Hungary.

Persson, A. and *Grazzini, F.,* 2007: *User Guide to ECMWF Forecasts Products: Meteorological Bulletin, 3.2 (version 4.0),* ECMWF, Reading, UK.

Raoult, B., 2001: MARS on the Web: a virtual tour. *ECMWF Newsletter 90,* 9-17.

Simmons, A., Uppala, S., Dee, D. and *Kobayashi, S.,* 2007: ERA-Interim: New ECMWF reanalysis products from 1989 onwards. *ECMWF Newsletter No. 110,* 25-35.

Uppala, S.M., Kallberg, P.W. Simmons, A.J., Andrae, U., Bechtold, V.D., Fiorino, M., Gibson, J.K., Haseler, J., Hernandez, A., Kelly, G.A.;Li, X., Onogi, K., Saarinen, S., Sokka, N., Allan, R.P., Andersson, E., Arpe, K., Balmaseda, M.A., Beljaars, A.C.M., Van De Berg, L., Bidlot, J., Bormann, N., Caires, S., Chevallier, F., Dethof, A., Dragosavac, M., Fisher, M., Fuentes, M., Hagemann, S., Holm, E., Hoskins, B.J., Isaksen, L., Janssen, P.A.E.M., Jenne, R., McNally, A.P., Mahfouf, J.F., Morcrette, J.J., Rayner, N.A., Saunders, R.W., Simon, P., Sterl, A., Trenberth, K.E., Untch, A., Vasiljevic, D., Viterbo, P., Woollen, J., 2005: The ERA-40 Reanalysis. *Q. J. Roy. Meteor. Soc. 131,* 2961-3013.

Üveges, Z., 2009a: Calibration of monthly forecasts of the ECMWF (in Hungarian). *Proc. of the 29th Scientific Student Conference (OTDK),* Szombathely, Hungary. March 23-24, 2009.

Üveges, Z., 2009b: Calibration of monthly forecasts of the ECMWF.(in Hungarian). *Master Thesis,* Eötvös Loránd University, Budapest, Hungary.

Woods, A., 2006: *Medium-Range Weather Prediction The European Approach.* Springer.

IDŐJÁRÁS

Quarterly Journal of the Hungarian Meteorological Service
Vol. 114, No. 4, October–December 2010, pp. 287–302

Modeling of the urban heat island pattern based on the relationship between surface and air temperatures

J. Unger[1*], T. Gál[1], J. Rakonczai[2], L. Mucsi[2], J. Szatmári[2], Z. Tobak[2], B. van Leeuwen[2], and K. Fiala[3]

[1]*Department of Climatology and Landscape Ecology, University of Szeged, P.O. Box 653, H-6701 Szeged, Hungary; E-mail: unger@geo.u-szeged.hu*

[2]*Department of Physical Geography and Geoinformatics, University of Szeged, P.O. Box 653, H-6701 Szeged, Hungary*

[3]*Directorate for Environmental Protection and Water Management of Lower Tisza District, P.O. Box 390, H-6701 Szeged, Hungary*

[*]*Corresponding author*

(Manuscript received in final form July 27, 2009)

Abstract—The aim of this study is to develop a new – and easy to use – method for early night-time near-surface air temperature pattern estimation based on surface temperature data in urban areas. The surface temperature data have been collected by an airborne thermal infrared sensor at an altitude of 2000 m above ground level. The study area was covered by hundreds of images with a spatial resolution of about 2 m. The measured values were calibrated with data of in situ surface measurements of different land use types. Simultaneous air temperature measurements were carried out using a car-based temperature sensor along an almost 12 km long N-S urban transect. The measured points were located using a GPS device. Data were processed with GIS methods, including newly developed algorithms. In order to find the relationship between air and surface temperatures a wider environment, the source area which determines the air temperature at a given point and time was taken into account. Using a source area with a radius of 500 m, a strong relationship was detected between the two parameters. Namely, the temperatures of the surfaces found in the surroundings (weighted by the distance) determine the temperature of the air parcel located at a given point. The obtained regression equation was applied to extend our results in order to model the air temperature field in a larger urban area.

Key-words: urban environment, surface and air temperatures, remote sensing, source area, Szeged, Hungary

1. Introduction

The thermal features of settlements are different from their natural surroundings. This phenomenon is related to the alteration of the original surface (material, geometry) and the by-products of human activity (heat, water vapor, pollution). As a consequence, a temperature excess develops in our living space in the near-surface air layer (compared to the rural areas). This is the so-called 'classical' *urban heat island* (UHI), already recognized at the end of the 18th century but named only much later by *Balchin* and *Pye* (1947).

As subsequent studies revealed, many kinds of UHIs can be defined. They include those defined according to the target medium (air, surface, sub-surface), the location (surface nature, height of measurement), and the type of sensor (*Roth et al.*, 1989). Considering the thermal effect of cities according to these new approaches, they do not appear in an 'island' structure. Moreover, the investigations are often directed on the intra-urban variations of the temperature. Therefore, in these cases it is more appropriate to talk about the *urban temperature field* or *pattern*. Besides 'classical' UHI, this study concentrates on urban surface temperature patterns.

Cities present an almost limitless array of surface configurations (*Soux et al.*, 2004). The detemination of the surface temperature in cities is difficult because of the complex structure of the urban-atmosphere interface (*Voogt* and *Oke*, 1997). In large urban areas it is usually measured indirectly by remote sensing technology mounted on satellite or aircraft platforms, but the sensor can be carried by car or manually too. In this case the problem is that the camera does not 'see' the total active surface because of the obstructions present on the 3D surface (*Roth et al.*, 1989; *Soux et al.*, 2004).

The temperature of the air (T_a) among the buildings is affected by the temperatures (T_s) of both horizontal and vertical surfaces (e.g., roofs, roads, tree tops, ground, walls) (*Voogt* and *Oke*, 1998). This multiple impact and the magnitudes of the effects of individual factors are very difficult to determine. *Voogt* and *Oke* (1997) introduced the concept of *complete surface temperature* which cannot be measured directly, but it can be calculated or estimated as a result of the radiation originating from all of the (horizontal and vertical) surfaces. Since such a detailed survey is extremely time-consuming, it cannot be applied in a larger area.

Roth et al. (1989) came up with the question of what the relationship is between surface and air temperature patterns. It is known that the nocturnal intra-urban variability in T_s is much smaller than the diurnal variability, while the opposite is true for T_a. As the near-surface climates are directly connected to the active surface (if the larger scale weather situation is favorable) there seems to be a contradiction. According to *Roth et al.* (1989), this could be due to the following: (i) lack of simple connection between the T_s and T_a values (implied also by *Goldreich* (1985)), (ii) remote sensors do not perceive the full active

surface, (iii) failure to recognize the different scales of climatic phenomena in the urban environment.

In the frame of a small review, we only go through the results of some earlier studies, which partly dealt with T_s–T_a relationship. Because of the better geometric resolution, in these studies the surface infrared images were taken from airborne platforms (with one exception). The T_a data were obtained by mobile transects or fixed stations at 1.5–2 m above the ground. The observations of both parameters were taken at 'ideal' (calm and clear) weather conditions in the evening or at night. The parameters of the mentioned studies are summarized in *Table 1*.

Table 1. Parameters of nocturnal surface and air temperature measurements of some earlier studies

City	Thermo camera platform, altitude of flying	Pixel size	Type of stations	Source
Johannesburg	Aircraft, 400 m	2.5 m^2	Mobile	*Goldreich* (1985)
Malmö	Aircraft, -	1 × 2 m	Mobile	*Bärring et al.* (1985)
Göteborg	Aircraft, 600 m	2 × 2 m	Fixed, mobile	*Eliasson* (1992)
Göteborg	Manual	-	Fixed, mobile	*Eliasson* (1996)
Tel-Aviv	Helicopter, 2300 m	2 × 2 m	Mobile	*Ben-Dor* and *Saaroni* (1997)
Tel-Aviv	Helicopter, 2300 m	2 × 2 m	Mobile	*Saaroni et al.* (2000)

The investigation made by *Goldreich* (1985) is among the first of our subject. Results of both measurement methods indicate one nocturnal UHI core and a strong temperature gradient at about 600 m from the core, so the two temperature patterns overlap.

Bärring et al. (1985) found that high T_s can also be observed in suburban streets, provided that the streets are narrow enough. In contrast, T_a values decrease from the city center to the outskirts. According to their explanation, the air temperature is influenced both by the local street surface temperature, which is regulated by street geometry, and by the general thermal level of the surrounding city area determined by its general geometry and other UHI generating factors (air pollution, anthropogenic heat release).

Eliasson (1992) compared the two temperatures measured along a route in streets and squares in a central urban area. While she observed 5 °C differences on the surface, the T_a variation was well-balanced with a range of only a few tenths of degrees. Later *Eliasson* (1996) draws attention to the fact that many studies do not make a clear distinction between surface and air temperatures. For example, the results of models predicting T_s are often compared or validated with field studies of T_a. She compared the variations in the two parameters along urban transects and found that the intra-urban surface and air temperature patterns are very different. T_s is influenced by the immediate urban structure (geometry), while T_a is not, so the former shows far larger fluctuations than the latter.

Ben-Dor and *Saaroni* (1997) compared surface and air temperature patterns measured separately along four N-S transects in a large urban area. The T_s values were computed as averages of about 40 pixel values around the spots of the T_a recordings. On and over uniform (asphalt) surfaces, they found strong relationships between the two temperature variations for all transects. *Saaroni et al.* (2000) generated isotherm maps from the measured T_s and T_a values along the four transects mentioned above. The obtained temperature fields were similar both in areal structure and magnitude.

The results of the mentioned studies are a bit contradictory. As *Voogt* and *Oke* (2003) summarized, the relations between the two parameters remained empirical and no simple general relation was found, but the correlations improved at night when microscale advection is reduced. It is clear that the complex interrelations between the two parameters in urban environments are not unambiguously detected or it is not even possible to describe them. Within this system, our research is focused on the area of impact which has an influence on the temperature of the near-surface air, presuming that a statistically based relationship can be established between the two temperatures if the size of this area is appropriately selected. Accordingly, the area of impact or *source area* is the place where the total impact of the physical features of its elements and their responses to the outer effects (heating-cooling, generation of turbulent processes) determine the temperature of a given air parcel.

The aim of this study is (i) to compare the air and surface temperatures developing in a complex urban environment, (ii) to reveal the relationship between them applying different source areas, and (iii) to generate an air temperature field for a large urban area with the help of the obtained relationship for two summer evenings, when the weather conditions in the preceding 36 hours were favorable for the microclimate modifying effects of the surface features.

2. Study area, weather situations

2.1. Szeged

Szeged is located in the southeastern part of Hungary (46°N, 20°E) at 79 m above sea level on a flat plain (*Fig. 1*). It belongs to the climatic region *Cf* according to Köppen's classification (temperate warm climate with uniform annual distribution of precipitation) (*Péczely*, 1979). Szeged provides a favorable background for urban climatological research, since its climate is free from the influences of orography and large water bodies, while its weather is characterized with high sunshine duration, low wind speed, and low precipitation (*Table* 2). Therefore, research on urban heat island and its consequences in Szeged has a several year long history (e.g., *Unger*, 1996; *Unger et al.*, 2001; *Kristóf et al.*, 2006).

Fig. 1. (a) City center, (b) housing estates, (c) detached houses with gardens, (d) industry and warehousing, (e) agricultural, green, and open area as land use types in Szeged.

The city's population of about 160,000 lives within an administration district of 281 km^2, but the highly urbanized area is restricted to an area of about 30–35 km^2. In the course of the 19th century, a structure of boulevards and avenues was established using the river Tisza as an axis. A large number of different land-use types are present including a densely built center with medium-wide streets and large housing estates of tall apartment buildings set in wide green spaces. There are zones used for industry and warehousing, areas occupied by detached houses, and considerable open spaces along the banks of the river, in parks, and around the city's outskirts (*Fig. 1*).

Table 2. Climate averages (1961–1990) in Szeged region (*WMO*, 1996)

Parameter	August	Year
Sunshine duration (h)	266	2023
Wind speed (m s^{-1})	2.8	3.4
Air temperature (°C)	20.2	10.5
Relative humidity (%)	69	75
Precipitation (mm)	57	495

2.2. *Weather situations before and during the measurements*

The observed T_a and T_s values depend not only on the momentary weather conditions but on the conditions prevailing in the previous (a few hours or days) time period as well. Therefore, a short description is given about the weather features of the 36-hour periods preceding the measurements of August 12 and 14, 2008 (between 18:30 and 19:30 UTC, see Section 3.1.).

The observations of the University station located at the edge of the city center were used to characterize the weather in the mentioned time period. Among them, the data of global radiation (G) and wind speed (v) are the most important, because these values reflect whether the weather was clear and calm (*Fig. 2*). According to the data, the insolation was undisturbed during the daylight hours (regular bell-shape G variation) with maximum values of 810 – 860 W m^{-2}. On the whole, the air movement was moderate (0 – 4.7 m s^{-1}) and during the measurements, it ranged between 0.8 and 3.1 m s^{-1}. Since the wind speed was measured at 26 m above ground level, it was likely to be significantly smaller at the street level. The days were rather warm with maximum values of 28 –36 °C and with minimum values of 17–22 °C at dawn.

Consequently, during the investigated period, the weather conditions promoted the microclimatic effects of the surface features in Szeged.

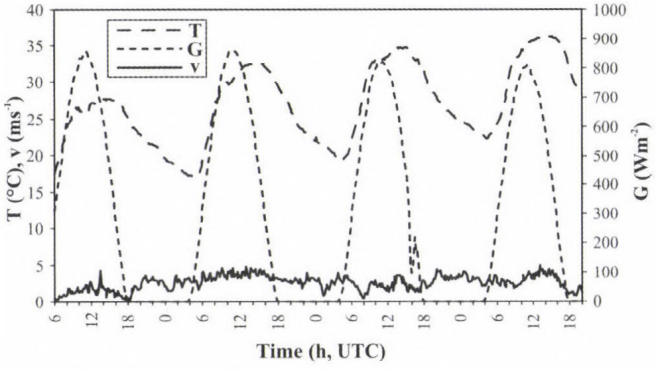

Fig. 2. Variation of global radiation (G), air temperature (T), and wind speed (v) at the University station during the measurements and the preceding one and a half days (06:00 UTC, August 11, 2008 – 20:00 UTC, August 14, 2008).

3. *Methods*

3.1. *Temperature measurements*

The measurements in August took place in the 1.5 –2-hour periods immediately after sunset, because there was no direct shortwave radiation disturbing the signals recorded by the camera at that time and the flight did not violate the flight ban

after 22:00 LST. As sunset was at 19:57 LST (17:57 UTC), the airborne images were taken between 18:15 and 19:45 UTC, the surface and near-surface measurements were performed between 18:30 and 19:30 UTC. Thus, 19:00 UTC (1 hour after sunset) can be regarded as a reference time of all measurements. It is worth to note that test measurements were taken on July 29, 2008 in order to optimize the flying parameters, spots, and route of the surface and near-surface observations, as well as to harmonize the work of the different measurement teams (flying – 3, mobile measurement – 2, measurements by hand – 4 people).

3.1.1. Mobile air temperature measurements along a N-S urban transect

Mobile measurements are widespread in studying urban climatic parameters (e.g., *Conrads* and *van der Hage*, 1971; *Eliasson*, 1996; *Voogt* and *Oke,* 1997; *Henninger* and *Kuttler*, 2007). In our case the temperature observations were carried out by an automatic radiation-shielded sensor (DCP D100089 HiTemp) connected to a digital data logger (LogIT DataMeter 1000) that provided data at every 2 seconds. In order to diminish the thermic disturbing effect of the car, the sensor was located on a bar 0.6 m before the car and 1.45 m above the ground. Due to the requirements of efficient ventilation and data density, the speed of the car was 20–25 km h^{-1}, and thus the data were gathered every 11–14 m. The locations of the data along the measurement route were recorded by GPS. Data measured at the compulsory stops (red light, barrier etc.) were later deleted from the database.

The 11.8 km long measurement route is a N-S transect of Szeged crossing the typical urbanized land use areas of the city (housing estates, detached houses with gardens, city center, industry, and warehousing). One-hour measurements were taken there and back along the route in order to make time adjustments to the reference time (19:00 UTC) assuming linear air temperature change with time at this period of the day (*Oke* and *Maxwell*, 1975). This linear change was also observed in the records of the University weather station (*Fig. 2*). In order to get uniform temperature distribution along the route, the route was divided by 15 m, then the averages of the mean values of the readings taken separately there and back on the 15 m long sections were computed (*Fig. 3*). Thus, there are altogether $2 \times 786 = 1572$ T_a values, which refer to the middle points of these sections.

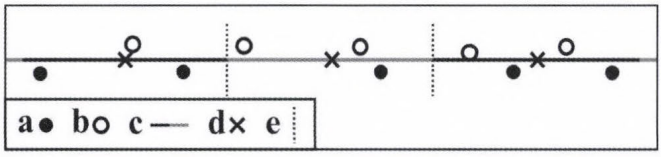

Fig. 3. An example on the spots of air temperature values regarded at the averaging route. (a) spots there, (b) spots back, (c) 15 m long sections, (d) section centers, (e) section borders.

The relative temperatures by points along the route (that is the UHI intensity) were determined by regarding the value of the minimum T_a as a UHI intensity of 0 °C.

3.1.2. Surface temperature measurements in the urban environment using an airborne thermal camera

The thermal measurements were carried out using a self-developed low-cost small-format digital imaging system. The current system is based on the experiences gained during earlier research using thermal (*Mucsi et al.*, 2004) and CIR (color-infrared) small format aerial photography (SFAP) data collected with a small airplane (*Rakonczai et al.*, 2003; *Szatmári et al.*, 2008). The system is based on a FLIR ThermaCam P65 thermal camera integrated with a navigation system and a GPS/GNSS receiver (Mobile Mapper CE).

The FLIR (forward looking infrared radiometer) is a compact single-band thermal camera with a temperature sensitivity of 0.08 °C. The instrument can measure temperatures between −40 °C and +500 °C and has a resolution of 320 × 240 pixels. The camera has germanium lenses to register the thermal radiation emitted by the object of investigation.

The flight plan determined the data collection density during the survey. Since a fixed photographic lens was used for the camera, the flying speed, height, and the distance between consecutive flight lines defined the overlap between adjacent images. For later post-processing purposes, an overlap of at least 20–30% was needed. To collect data at the required density, one image per 4 seconds was recorded while flying with a speed of 120 km h^{-1} at a height of 2000 m.

Before the flight, a detailed flight plan (*Fig. 4*) was created, and during the survey this plan was followed as accurately as possible. A Mobile Mapper CE GPS/GNSS receiver provided navigational aid during the flight and recorded the actual high precision GPS flight track, which was used for positioning the images during the post-processing phase.

After the survey, the acquired data needed to be post-processed. Using software specifically designed for the analysis of the thermal images, several parameters needed to be readjusted. Using the results of the fieldwork carried out at the same time as the flight, the data was inspected and calibrated (see Section 3.1.3.). The temperature data collected by the thermal camera was refined based on the time-synchronized field measurements of the same evening as the flight. After this, the thermographic data was stored in a file as a matrix, containing the calibrated temperatures.

The next step in the thermal processing chain was the extraction of the coordinates and time data from the GPS track log recorded during the flight. This data was connected to the camera log file that stores the precise time of every recorded image. With this operation, EOV coordinates were generated for

every image center. During the next step, the center coordinate and the image resolution were combined to create a so-called world file. A world file is a simple text file that was used to georeference the thermal images. Using this georeference, a first, coarse geometric correction was executed with an accuracy of about 100–150 meter, depending on the weather circumstances during the flight (*Fig. 5*). In the next step, the images were combined to one single image, resulting in a thermal mosaic with a spatial resolution of 2.5 m, covering the complete survey area (*Fig. 6*).

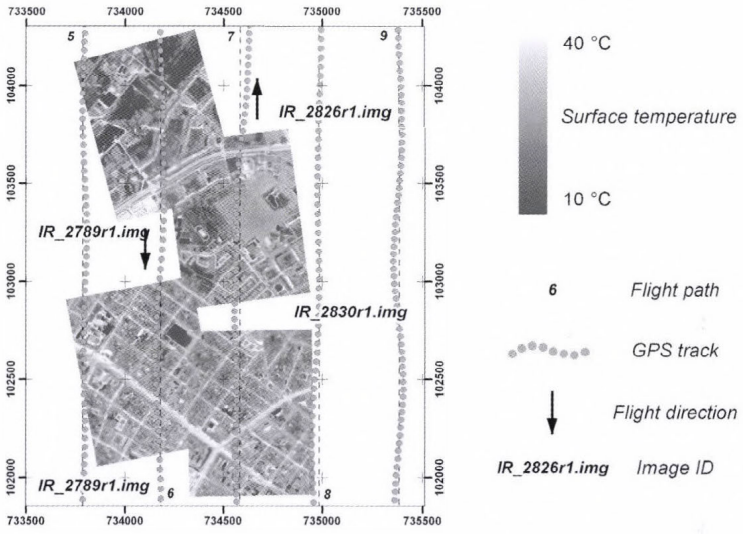

Fig. 4. Flight plan with real GPS track and calibrated sample thermal images of the city.

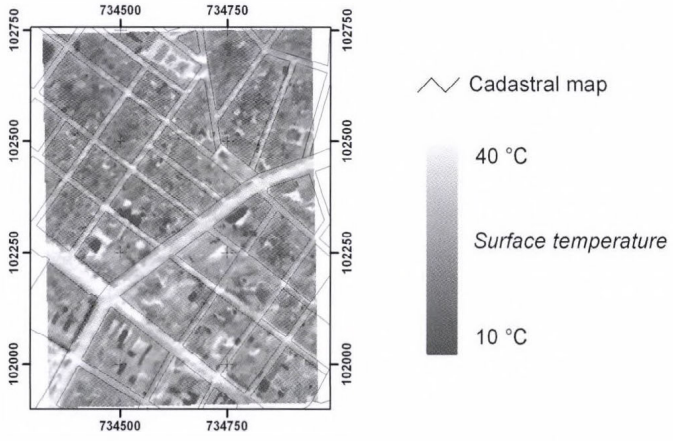

Fig. 5. Georeferenced (Hungarian EOV) thermal image with cadastral vector layer.

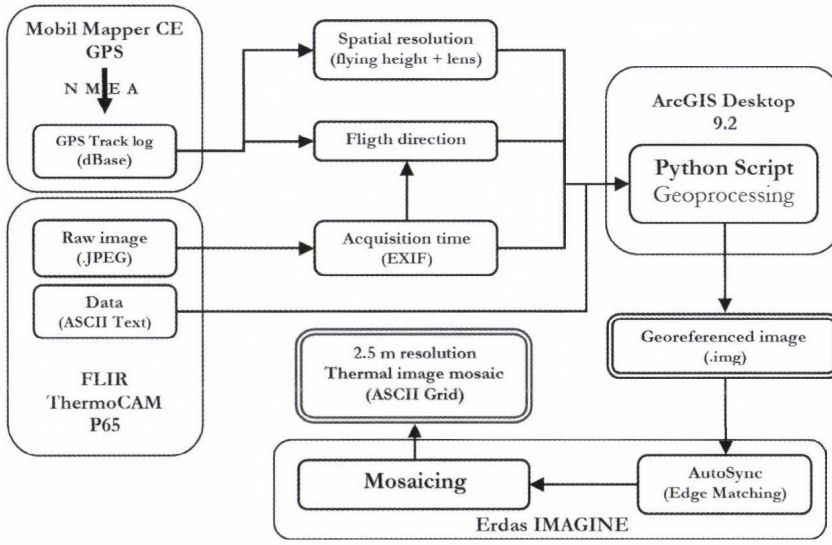

Fig. 6. Flowchart of the image processing.

It was assumed that some decrease can be found in the surface temperatures during the flight times (50 and 51 minutes on August 12 and 14, respectively). If this dependence from the time is significant, the pixel values have to be corrected to the middle time (19:00 UTC) of the survey according to the general cooling tendency. A statistically established trend was found only in the evening of August 14 (*Fig. 7*).

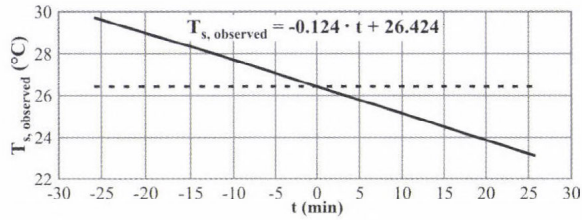

Fig. 7. Regression line of the pixel values ($T_{s,observed}$) as a function of time (t) in August 14, 2008.

In order to refer the pixel values to the middle time, these values were corrected by the obtained cooling rate: the values before the middle time were lowered; the ones after the middle time were increased:

$$T_{s,observed} = -at + b, \qquad T_s = T_{s,observed} + at,$$

where $T_{s,observed}$ is the measured pixel value, a is the slope of the regression line,

t is the time in minutes (–25.5 – 25.5), b is the value of the regression line at the middle time, and T_s is the corrected pixel value. Henceforth T_s means the uncorrected and corrected surface temperature in August 12 and 14, respectively.

3.1.3. In situ surface temperature measurements in selected points of representative urban surfaces

The temperature of the surface was measured directly by hand (DCP D100047 ProTemp sensor, LogIT DataMeter 1000 data logger) in the 40 selected points representing the urban surfaces in two sample areas (*Fig. 1*). These T_s values are necessary for the calibration of the airborne thermal images, namely for transforming the relative temperature scale of the images to an absolute scale.

3.2. Statistical method to reveal the relationship between air and surface temperatures

As mentioned in Section 1, the air temperature at a given point at 1.5 m above ground level depends not only on the immediate surface under it and its own temperature. The T_a of this point is a result of the total effects of the turbulent heat transports generated by the surrounding heated surfaces. Several studies looking for T_a–T_s relationship point out the importance of the micro-advection in the near-surface air layer (e.g., *Roth et al.*, 1989), which promotes the mixing of the thermal properties in a wider environment. Therefore, to investigate this connection a larger area, the source area and its thermal features have to be taken into account. According to the related literature, this source area covers an area with a radius of a few hundred meters around the measurement point, and in the case of calm weather it can be regarded as a circle. In case of a temperature sensor at 1.5–2 m above ground level in urban environment, the circle has a radius of maximum 0.5 km, but this is likely to depend on the building density (*Oke*, 2004).

These active surfaces are not only horizontal but also vertical (e.g., walls). In affecting the value of T_a, the role of the surfaces nearer to the point is more important compared to the ones farther away. It has to be taken into account that in the case of 1.5 m level, the role of the roofs is likely to be smaller than the role of the ground surfaces (pavements, roads, parking lots, grass areas, etc.). In our case, only the temperatures of the horizontal surfaces can be detected on the thermal images, thus we can only use these temperatures in searching for the relationship between T_a and T_s.

For the determination of the size of the source area for the T_a values along the transect and the distance-based weighting of the pixel values inside it, different approaches were applied. Only those are presented here which gave the best results in investigating the relationship and that are in accordance with the conditions mentioned above.

Among the results of the manual T_s measurements, the lowest value was 19.4 °C, however, the possibility of lower values occurring in the investigated area cannot be excluded. After the air temperature data was processed, it became clear that there are areas detected by the camera that have temperatures that are up to 15 degrees lower than the directly surrounding surface. The reason for this is the heterogeneity of the urban environment. The camera was setup to use normal calibration values. The physical properties of the roofs constructed from metal considerably differ from the standard calibration values. Highly reflective surfaces like aluminum, copper, or stainless steel work as a mirror resulting in false temperature measurements. The false temperatures were identified and filtered out of the images.

As a second step, according to the maximum size of the source area mentioned above (*Oke*, 2004), circles with a radius r (r = 100–500 m) around the points of T_a values were selected (see Section 3.1.1.). The (filtered) T_s pixel values of these circles were taken by weighting, the farthest (r) values with a factor of 0.5, the nearest ones (0 m) with a factor of 1, and the ones between them with a proportionality factor between 0.5 and 1. Thus, the weighted and averaged surface temperature ($T_s(wr)$) regarding a given point's surrounding with a radius of r is determined by the next formula:

$$T_S(wr)=\frac{\sum_{i=1}^{n} T_{Si}\cdot\left(1-\frac{D_i}{2r}\right)}{\sum_{i=1}^{n}\left(1-\frac{D_i}{2r}\right)}, \tag{1}$$

where T_{Si} is the ith pixel value, D_i is the distance of the ith pixel from the given point, and the summation refers to all (not filtered) pixels inside the circle with a radius of r. In order to automate this calculation for all points along the transect, an algorithm was developed in the ArcView Avenue script language.

4. Results

Fig. 8 shows the variations of the UHI intensity along the transect on the two evenings. The reference place (with the lowest T_a value) is located in an area with abundant vegetation almost at the south end of the transect. In cities in the temperate climate zone during 'ideal' weather conditions the maximum development of the UHI occurs 3–5 hours after sunset because of the different cooling rates of urban and rural areas (*Oke*, 1987). Therefore, in our case (1 hour after sunset), the obtained UHI intensities are likely to be smaller than the maximum values occurring during the same night.

In the evening of August 12 the intensity was relatively high (~2 °C) at the north end of the transect, wich can be attributed to the area characterized with buildings of a housing estate. Going towards the south, two maximums

reaching almost 3 °C occurred: the first one in an area with large artificial surfaces (shopping centers, parking lots), while the second one appeared in the densely built-up city center. From here the intensity decreases almost continuously towards the south end of the transect.

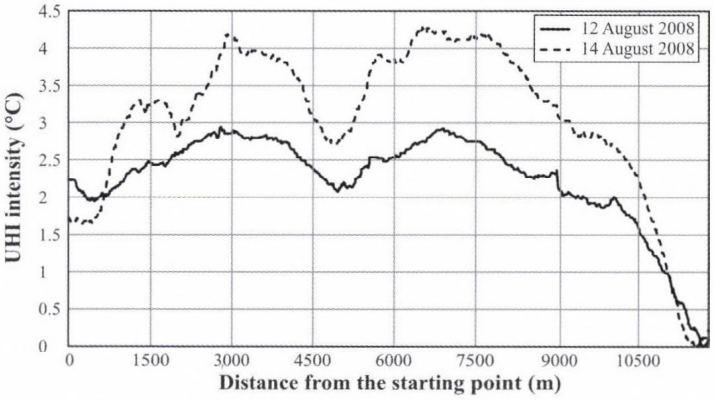

Fig. 8. UHI intensities along the N-S transect in Szeged (19:00 UTC, August 12 and 14, 2008), starting point at the north.

On August 14, the variation of the intensity was very similar to the previous one with the exceptions of the maximum values, which exceeded even 4 °C this evening.

Since the measurement route was located inside the urban area, the obtained intensity values reflect the intra-urban temperature variation rather than the real magnitude of the UHI. Namely, when we talk about the heat island, the urban temperatures are usually compared to the temperatures of the surrounding rural ('natural') areas (*Oke*, 1987; *Lowry*, 1977). This can also be an explanation for the moderate magnitude of the obtained maximum UHI values in this study.

According to the method described in Section 3.2, several relationships can be obtained between the T_a values along the transect and the $T_s(wr)$ values computed by Eq. (1) with different radii (two measurements – n = 1572). As *Table 3* shows, the relationships are significant in all cases (even at a level of 0.1% at this high number of element pairs), however, the larger the radius the stronger the connection between the two parameters (to the upper limit of r, see Section 3.2.). This can be explained by the thermal compensatory effect of the larger area and confirm the possible size of the source area related to the air temperature measured at a level of 1.5 m in urban environments. Since the best relationship is derived in the case of $r = 500$ m, henceforth the regression equation obtained in this case is applied to extend our results: to model the spatial distribution of T_a in a larger urban area in the case of the investigated two evenings.

Table 3. Relationships between T_s and T_a along the urban transect and their parameters regarding the surroundings with different radius r (R^2 is the determination coefficient, R is the correlation coefficient, σ_R is the standard deviation around the regression line) on August 12 and 14, 2008 (n = 1572)

r (m)	Regression equation	R^2	R	σ_R	Significance level
100	$T_a = 0.373 \times T_s(w100) + 17.691$	0.574	0.757	0.858	< 0.001
200	$T_a = 0.406 \times T_s(w200) + 16.898$	0.611	0.781	0.820	< 0.001
300	$T_a = 0.426 \times T_s(w300) + 16.453$	0.642	0.801	0.787	< 0.001
400	$T_a = 0.436 \times T_s(w400) + 16.228$	0.663	0.814	0.763	< 0.001
500	$T_a = 0.447 \times T_s(w500) + 15.982$	0.685	0.828	0.738	< 0.001

In the course of the extension of our results, surface temperatures in the whole study area were used as input data in a 100 m × 100 m mesh for modeling the air temperature fields in the evenings of August 12 and 14. Since for computing $T_s(w500)$ the pixel values around the mesh points ($r = 500$ m) are needed, the modeling area is smaller (~21 km^2) compared to the originally recorded area (marked by intermittent line in *Fig. 1*). The deficiencies at the corners are caused by some errors in the flying paths.

The modeled air temperature field on August 12 has large areas with a temperature greater than 26.5 °C. This area is located in the city center and streches out towards NW, where industrial and warehousing land use dominates (*Fig. 9a*). A temperature extension is present in NE direction, where the large housing estates can be found. The cooler areas of the low built-up districts, the outer green zones, and the belt of the Tisza River and its banks (at NW, SW, and SE) are also recognizable. On the whole, a difference of about 3 °C occurs in the area which is in accordance with the temperature range experienced along the transect in this evening (*Figs. 8* and *9a*).

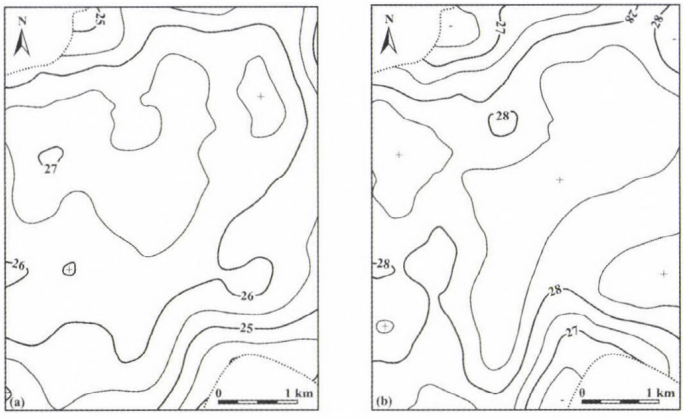

Fig. 9. Modeled air temperature patterns in Szeged at 19:00 UTC, (a) August 12 and (b) August 14, 2008 (location of the area is shown in *Fig. 1*).

The values of the modeled air temperature pattern on August 14 are higher than the values of the previous one (*Fig. 9b*). As on August 12, basically the warmest (>28.5 °C) areas can be found in the center, in the NW and NE parts, augmented towards the south. Broadly speaking, the cooler areas are also the same. On the whole, also a difference of about 3 °C occurs in the area, which is a bit lower than the temperature range measured along the transect of this evening (*Figs. 8* and *9b*).

5. Conclusions

In this study we tried to reveal a statistical (but physically supported) connection between the air and surface temperatures measured in an urban environment. During the data collection, airborne and surface-based remote sensing (indirect) and traditional (direct) tools and methods were applied. In order to search for the mentioned relationship, a wider environment, the source area was taken into account, which determines the air temperature at a given point and time. As the results show, using a source area with a radius of 500 m, a strong relationship was detected between the two parameters. Namely, the temperatures of the surfaces found in the surroundings (weighted with the distance) decisively influence the temperature of the air parcel located at a given point. The obtained regression equation was applied to extend our results in order to model the air temperature field in a larger urban area in the investigated two evenings.

By all means we should not forget that the obtained relationship is based on the data of only two, however complex, measurement campaigns. In the future, when using data of more measurements on days with similar environmental conditions to that of the investigated days, the result could be refined. Based on these new results we can make steps to the generalization of the operation mechanisms between the urban air and surface temperatures. In the frame of this study, a data collection in different seasons could also be a new direction, which can provide a possibility to examine the specific seasonal features and enable their comparison.

Acknowledgements—This work was supported by the Hungarian Scientific Research Fund (OTKA T048400, K-67626). The authors' special thanks are due to *G. Barna, K. Balogh, N. Kántor, Z. Ladányi, Z. Sümeghy, T. Unger* taking part in the measurements and to *E. Tanács* for the language revision of the manuscript.

References

Balchin, W.G.V. and *Pye, N.*, 1947: A micro-meteorological investigation of Bath and the surrounding district. *Q. J. Roy. Meteor. Soc. 73,* 297-319.

Bärring, L., Mattsson, J.O. and *Lindqvist, S.*, 1985: Canyon geometry, street temperatures and urban heat island in Malmö, Sweden. *J. Climatol. 5,* 433-444.

Ben-Dor, E. and *Saaroni, H.*, 1997: Airborne video thermal radiometry as a tool for monitoring microscale structures of the urban heat island. *Int. J. Remote Sens. 18,* 3039-3053.

Conrads, L.A. and *van der Hage, J.C.H.*, 1971: A new method of air-temperature measurement in urban climatological studies. *Atmos. Environ. 5*, 629-635.

Eliasson, I,, 1992: Infrared termography and urban temperature patterns. *Int. J. Remote Sens. 13,* 869-879.

Eliasson, I., 1996: Urban nocturnal temperatures, street geometry and land use. *Atmos. Environ. 30,* 379-392.

Goldreich, Y., 1985: The structure of the ground heat island in a central business district. *J. Clim. Appl. Meteorol. 24*, 1237-1244.

Henninger, S. and *Kuttler, W.*, 2007: Methodology for mobile measurements of carbon dioxide within the urban canopy layer. *Climate Res. 34,* 161-167.

Kristóf, G., Bányai, T. and *Rácz, N.*, 2006: Development of computational model for urban heat island convection using general purpose CFD solver. *Preprints 6th Int Conf on Urban Climate,* Göteborg, Sweden, 822-825.

Lowry, W.P., 1977: Empirical estimation of urban effects on climate: A problem analysis. *J. Appl. Meteorol. 16*, 129-135.

Mucsi, L., Kiss, R., Szatmári, J., Bódis, K., Kántor, Z., Dabis, G. and *Dzsupin, M.*, 2004: The analysis of contamination deriving from the leakage of subsurface pipeline networks via remote sensing (in Hungarian). *Geodézia és Kartográfia 56*/4, 3-8.

Oke, T.R., 1987: *Boundary Layer Climates.* 2nd edition. Routledge, London-New York.

Oke, T.R., 2004: Siting and exposure of meteorological instruments at urban sites. *27th NATO/CCMS Int Tech Meeting on Air Pollution Modelling and Application.* Kluwer, Banff, Canada, 14 p.

Oke, T.R. and *Maxwell, G.B.*, 1975: Urban heat island dinamics in Montreal and Vancouver. *Atmos. Environ. 9,* 191-200.

Péczely, G., 1979: *Climatology* (in Hungarian). Tankönyvkiadó, Budapest.

Rakonczai, J, Csató, Sz, Mucsi, L, Kovác,s F, Szatmári, J, 2003: Experiences on the evaluation of the 1999 and 2000 excess waters (in Hungarian). *Vízügyi Közlemények Különszám IV,* 317-336.

Roth, M., Oke, T.R. and *Emery, W.J.*, 1989: Satellite-derived urban heat islands from three coastal cities and the utilization of such data in urban climatology. *Int. J. Remote Sens. 10,* 1699-1720.

Saaroni, H., Ben-Dor, E., Bitan, A. and *Potchter, O.*, 2000: Spatial distribution and microscale characteristics of the urban heat island in Tel-Aviv, Israel. *Landscape Urban Plan 48,* 1-18.

Soux, A., Voogt, J.A. and *Oke, T.R.*, 2004: A model to calculate what a remote sensor 'sees' of an urban surface. *Bound.-Lay. Meteorol. 111,* 109-132.

Szatmári, J., Tobak, Z., van Leeuwen, B., Olasz, A. and *Dolleschall, J.*, 2008: An effective and low-cost method to detect environmental contaminations: the promise of CIR small format aerial photography. *12th Geomathematics Conf.*, Mórahalom, Hungary.

Unger, J., 1996: Heat island intensity with different meteorological conditions in a medium-sized town: Szeged, Hungary. *Theor. Appl. Climatol. 54,* 147-151.

Unger, J., Sümeghy, Z. and *Zoboki, J.*, 2001: Temperature cross-section features in an urban area. *Atmos. Res. 58,* 117-127.

Voogt, J.A. and *Oke, T.R.*, 1997: Complete urban surface temperatures. *J. Appl. Meteorol. 36,* 1117-1132.

Voogt, J.A. and *Oke, T.R.*, 1998: Radiometric temperatures of urban canyon walls obtained from vehicle traverses. *Theor. Appl. Climatol. 60,* 199-217.

Voogt, J.A. and *Oke, T.R.*, 2003: Thermal remote sensing of urban climates. *Remote Sens. Environ. 86*, 370-384.

WMO, 1996: *Climatological normals (CLINO) for the period 1961-1990.* WMO/OMM-No. 847, Geneva.

IDŐJÁRÁS

Quarterly Journal of the Hungarian Meteorological Service
Vol. 114, No. 4, October–December 2010, pp. 303–318

Odor setback distance calculations around animal farms and solid waste landfills

Melinda Cseh[1], **Katalin F. Nárai**[1], **Endre Barcs**[1], **Dezső B. Szepesi**[1], **Dezső J. Szepesi**[1], and **James L. Dicke**[2]

[1]*Consultants on Air Resources Management (CARM) Inc., Katona József u. 41. V/25, H-1137 Budapest, Hungary; E-mail: szd12506@ella.hu*

[2]*Consulting Meteorologist, U.S.A.; E-mail: jldandpad@hotmail.com*

(Manuscript received in final form February 27, 2010)

Abstract—ODOR-TRANSMISSION (OT) is a regulatory model for estimating odor setback distances around livestock production farms and municipal solid waste landfills on virtual maps prepared by an interdisciplinary team. This paper describes the development of the model, odor emission and dispersion calculations, and visualization techniques. The atmospheric dispersion simulation portion is based on HNS-TRANSMISSION, an air quality model published by *Szepesi et al.* (2005), while the odor emission module is adapted mostly from U.S.A. results, e.g., *Guo et al.* (2004). As a new development, estimated setback distances from an odor source are presented on virtual maps. The main characteristics of the OT model can be found in the model catalogue system of the European Environmental Agency. A case study for a municipal solid waste landfill is also included. Furthermore, a comparison study with other odor setback distance calculation methods shows that reliable results can be obtained by using the OT model.

Key-words: odor, odor unit, transmission modeling, setback distance, exceedance probability, odor threshold

1. Introduction

Over the last decades, odor nuisances, e.g., from livestock production units, have become more frequent and intensive in our environment. Fundamental human rights include a pure, livable environment, and this includes odor-free air as well. To find solutions for odor problems, standard regulations must be adopted. This involves the need to determine setback distances around animal production farms, municipal solid waste landfills, wastewater treatment plants and factories that emit odorous gases. Most of the existing setback guidelines

were determined either by individual judgment and experience or by a combination of neighbor surveys and odor measurements, instead of calculations of dispersion models (*Guo et al.*, 2004). Determination of odor nuisances by olfactometria (testing and measurement of the sensitivity of the sense of smell) is essential, although the practice involves many subjective factors. Therefore, it is essential to establish a science-based model to predict setback distances more objectively. Such a model can become an effective tool for researchers, regulatory agency staff, and other decision-makers. The aim of this paper is to present the newly developed OT model for determining odor setback distances.

The OT model is an extended version of HNS-TRANSMISSION (*Szepesi et al.*, 2005), an air pollution regulatory model that includes a meteorological database for the calculations. The OT model consists of three main parts: (i) the odor emission module for estimating the odor source term; (ii) the HNS-TRANSMISSION model for calculating the atmospheric dispersion of the odorants, and; (iii) visualization techniques for presenting the setback distances on maps such as those obtained from Google®.

The odor emission module quantifies the odor emissions originating from animal farms, municipal solid waste landfills, and similar sources. Quantitative operating parameters of the facilities are necessary, e.g., types of animals, the area of the outdoor manure storage or the size of the municipal solid waste landfills, etc.

Odor dispersion in the outdoor air is simulated by the HNS-TRANSMISSION model. The OT model outputs are tables containing the number of odor exceedances vs the distance from each source by each of 16 wind directions. These results are analyzed according to the number of hours in a year, and thereby the area that is exposed to any given level of odor annoyance can be determined. The OT model produces setback distances along the 16 wind directions on a Google®-type map.

Both of these models are part of the model documentation system of EIONET program of the European Environmental Agency, (ODOR-TRANSMISSION: http://pandora.meng.auth.gr/mds/showlong.php?id=179, HNS-TRANSMISSION: http://pandora.meng.auth.gr/mds/showlong.php?id=48).

2. Estimating the odor source term

2.1. Odor

Odor is the property of a chemical substance or substance mixtures, dependent on the concentration, that activates the sense of smell, and thus starts an odor sensation (*Winneke* and *Steinheider*, 1994). As odor sensitivity differs in each person, a completely objective and analytical measurement cannot be done. However, it is possible to define the annoyance level of the odorant by several

methodologies. To measure odor, an olfactometry methodology is used that is based on a panel of human noses as sensors. For the determination of the quantity of odorants in the air, odor concentration is used – the dimension is European odor unit per m^3 (OU_E / m^3). The European odor unit by definition is: the amount of odorant(s) that, when evaporated into one cubic meter of neutral gas at standard conditions, elicits a physiological response from a panel (detection threshold) equivalent to that elicited by one European reference odor mass (EROM), evaporated in one cubic meter of neutral gas at standard conditions (*CEN*, 2003). EROM is the accepted reference value for the European odor unit, equal to a defined mass of a certified reference material. One EROM is equivalent to 123 mg *n*-butanol (CAS 71-36-3) evaporated into one cubic meter of neutral gas. This produces a concentration of 0.040 $mmol / m^3$ (*CEN*, 2003). These olfactometric measurements are needed to determine a reference scale for each odorant. However, for everyday regulations, these processes are too complicated and require considerable time. Therefore, more effective and straightforward techniques should be used, such as can be achieved by developing models based on the results of analytical measures. This is one aim of the OT modeling program.

2.2. Odors and their sources

The OT model was developed to address odors emitted from livestock operations, municipal waste landfills, and factories. The odor that is detected from a livestock operation is a complex mixture of gases. Most often the odor is a result of the uncontrolled anaerobic decomposition of manure. However, feed spoilage can also contribute to the odor. The odor that is detected by the human nose can be a combination of 60 to 150 different compounds. Some of the most important types of odor causing compounds are volatile fatty acids, mercaptans, esters, carbonyls, aldehydes, alcohols, ammonia, and amines. The odor strength of these compounds does not combine in an additive manner. That is, sometimes mixing several of these compounds can result in reduced odor by dilution of the strongest smelling compounds. In other instances, the mixture is worse than any of the individual compounds.

2.2.1. Animal farms

To determine the setback distance around an animal production farm, odor emissions must be estimated. Eq. (1) for calculating odor emissions is based on the Purdue model, which was developed by *Lim et al.* (2000) and combines features of Austrian and British setback guidelines (*Schauberger* and *Piringer*, 1997; *Williams* and *Thompson*, 1985):

$$OE = \Sigma (A_E \cdot N \cdot P \cdot B), \quad (1)$$

where

OE is the odor emission rate, OU/s,
A_E is the building odor abatement factor (0.30 –1.00),
N is the number of animals, and
P is the building odor emission factor, OU/s.

The second equation of the model is

$$B = M - D, \tag{2}$$

where

B is the building design and management factor,
M is the manure removal frequency (0.40 – 1.00), and
D is the manure dilution factor (0.00 – 0.20).

The OT model takes into consideration the following parameters: type of animals, number of animals, manure removal frequency, manure dilution factor, area of the storage building, wind speed above the ground, and odor abatement factors. The method for estimating odor emissions is based on the livestock unit. The livestock unit (LU) is a unit to compare or aggregate numbers of animals of different species or categories. Equivalences based on the food requirements of the animals are defined. While the Purdue model estimates the emissions for swine buildings, the OT model applies the methodology to other livestock units as well (*Table 1*). These livestock units are based on the field and laboratory measurements from the North Dakota State University, Dickinson Research Extension Center (*Manske*, 1998) and the Minnesota Department of Agriculture (*MDA*, 2009).

Concerning the outdoor manure system, an empirical equation (Eq. 3) is used based on the studies of *Heber et al.* (2002). This equation considers the area of the storage system and the wind speed above the ground.

$$OE_o = S \cdot 10^{-0.56+0.671V} \cdot A_s, \tag{3}$$

where

OE_o is the outdoor odor emission (OU/s),
S is the surface area of the outdoor manure storage, (m^2),
V is the wind speed, (m/s), and
A_s is the outdoor odor abatement factor (0.30 – 1.00).

After calculating the emissions for each subsystem of the animal production farm, the results are summed to obtain the final emission rate (Eq. 4):

$$OU/s = \Sigma OE + \Sigma OE_o. \tag{4}$$

Table 1. Livestock units for different animals (*Manske*, 1998; *MDA*, 2009)

Animal type	LU
Swine	
Swine heavier than 135 kg	0.400
Swine between 25 – 135 kg	0.300
Swine under 25 kg	0.050
Cattle	
Weaned cow lighter than 360 kg	0.750
Young cow between 360 – 405 kg	0.850
Cow between 405.–.495 kg with calf	1.000
Cow between 495 – 585 kg with calf	1.150
Cow heavier than 585 kg with calf	1.250
Bull lighter than 900 kg	1.500
Bull heavier than 900 kg	2.000
Calf	0.200
Horse	1.000
Lamb	0.100
Sheep	0.100
Chicken	
Broiler (liquid manure system)	0.033
Chicken heavier than 2.25 kg (dry manure system)	0.005
Chicken lighter than 2.5 kg (dry manure system)	0.003
Turkey	
Turkey heavier than 2.25 kg	0.018
Turkey lighter than 2.5 kg	0.005
Duck	0.010

2.2.2. Municipal solid waste landfills

Odor emission calculations for municipal solid waste landfills are based on Italian studies (*Sironi et al.*, 2005). For the estimation of odor emissions, the following parameters have to be taken into consideration: (1) annual waste acceptance, (2) waste density, (3) working days in one year, (4) height of the daily deposited waste layer, (5) surface of the active parcels, and (6) surface of the restored parcels. Eq. (5) expresses the relationships of these parameters:

$$OE_w = 59R/(\rho \cdot D \cdot H) + 8S_A + 4S_R, \tag{5}$$

where

OE_w is the odor emission from the municipal solid landfill, (OU/s),
R is the annual waste acceptance, (t/yr),
ρ is the waste density, (t/m^3),
D is the working days, (day/yr),

H is the height of daily deposited waste layer, (m/day),
S_A is the surface of active parcel, (m^2), and
S_R is the surface of the restored parcels, (m^2).

The results of the OT emissions module for all cases (animal production farms, manure storage systems, municipal solid waste landfills) are given in odor units/second. One odor unit (OU) in this paper is equal to one European Odor Unit (OU_E), which was defined above. The output of the OT emissions module is one of the data inputs to the HNS-TRANSMISSION model, which calculates the dispersion of odorants. HNS-TRANSMISSION normally expresses emissions in units of kilogram/hour, which is not equal to odor unit/second. The conversion is: 1 OU/s = $3.6 \cdot 10^{-6}$ kg/h.

3. Odor dispersion in the air

The OT model was developed from the HNS-TRANSMISSION model (*Szepesi et al.*, 2005), which is used for the calculation of pollutant dispersion in the atmosphere. The model is well-known and commonly used in air quality modeling practice in Hungary. The software considers meteorological parameters (wind speed, wind direction frequency, and atmospheric stability) and uses a long-period meteorological database for the whole area of Hungary. This database can be modified for use in other specific locations as well. Land-use and topographic conditions are taken into consideration by parameters specified in the software. The model calculates the concentrations of given pollutants at user-specified distances from the sources. Concerning odor nuisance modeling, the required data for the OT model include the following: (1) coordinates of the livestock sites (geometrical coordinates are used in order to determine the center of the emissions), (2) odor emissions (discussed above), and (3) properties of the emitted air (temperature, rate of flow). Based on these parameters, the OT model calculates odor concentrations along the 16 wind directions at user-specified distances from each source.

The HNS-TRANSMISSION model incorporates a Gaussian dispersion model. This is the most widely used model type for plume dispersion calculations. Its most attractive feature is that it fits what we see and experience in the real world for a range of conditions. In addition, the mathematics of the model is fairly straightforward. On the other hand, Gaussian models need significant empirical input to be used for practicable dispersion estimates, making the model results highly dependent on the conditions of the sampling used to derive the empirical values.

Similarly to the decision process used to select the appropriate model for regulatory purposes, the selection of the appropriate dispersion model for odor assessment starts with the source type and release scenario. In general, most sources can be categorized as point, area, or volume sources, with continuous or

instantaneous releases. The sources responsible for odor complaints are generally continuous sources, such as from stacks, scrubbers, or basins, although routine but instantaneous or very short-term releases (for example, from digester pressure release valves) can also pose problems at nearby receptors. Depending upon the rate of release relative to the short time frame of odor perception, intermittent sources can be classified as either continuous sources (release rate on the order of minutes or longer), or instantaneous sources (release rate on the order of seconds). Short-time concentrations are estimated from 30-minute maximum plume axis concentrations.

The OT model determines the number of odor exceedances at selected distances from sources along each of the 16 wind directions. The calculation requires the determination of the threshold limit for odors. In some European countries the odor threshold limit varies from 3 to 10 OU/m^3 (*Table 2*).

By setting a specific number of odor exceedances, the OT model calculates the setback distance along each wind direction around the virtual emission point. The setback distance represents the area within which odor nuisances are expected to occur more frequently than allowed in a year. For example, in an area where the odor exceedance probability is 1%, odor nuisances would be expected to occur on 88 hours per year. To develop a standard modeling system, an odor exceedance probability that is unacceptable needs to be determined by regulatory authorities, based on appropriate studies. Internationally, the most recently used value is 2%, which means that odor nuisances are expected to occur on 176 hours per year.

Table 2. Odor threshold limits in some European countries (*Ritvay* and *Kovács*, 2006)

Country	Odor threshold limit (OU/m^3)
Denmark	5 – 10
The Netherlands	5
Ireland	3 or 6
Norway	5 – 10
Hungary (suggested)	3 – 5

4. Presentation of setback distances on a virtual map

The OT model plots setback distances on Google®-type maps with an accuracy of ± 1 meter. In order to define the setback distance accurately, dimensions of the animal farm must be known. Based on these dimensions, the center, which is taken as the virtual emitting point, is defined. The geographical longitude and latitude coordinates of this point are the bases of the plotting system. The setback distances are measured from this point. By plotting the setback distance on each of the 16 wind direction axes, the odor impact zone can be illustrated on

an appropriate map. *Fig. 1* shows an example of the setback distance visualization around an animal farm. In this case the odor threshold limit was 3 OU/m^3, while the exceedance probability was 2%.

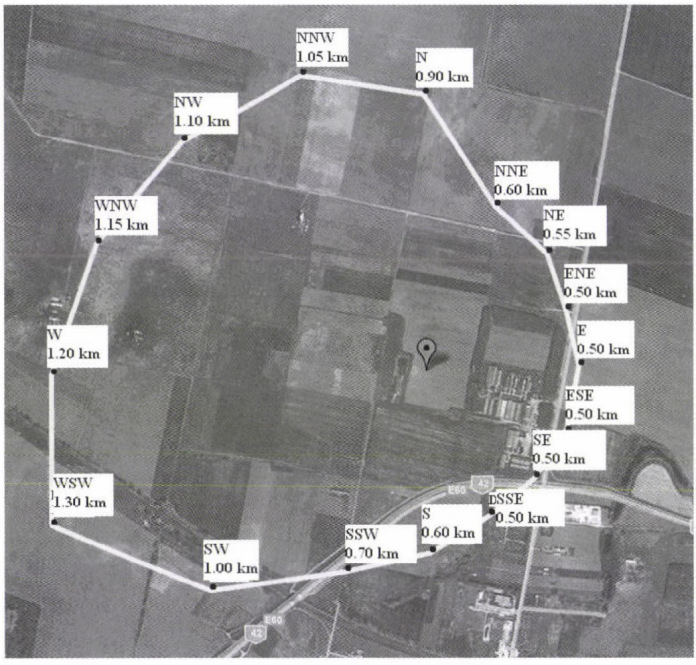

Fig. 1. Visualization on a Google map of the setback distances around an animal farm. The distances are measured from the virtual emitting point along the 16 wind directions.

This final visualization is a helpful tool for decision-makers, as the impact zone is well determined and visible. Furthermore, the mode of the map can be switched from any normal map to satellite-based (e.g., from Google®) and vice versa.

5. Setback distance determination around a municipal solid waste landfill

A case study was conducted to calculate odor emissions and setback distances around a municipal solid waste landfill in Dunakeszi, Hungary. The parameters of the landfill are given in *Table 3*.

Odor emissions are calculated based on Eq. (5). The output data of the emission calculations are also presented in *Table 3*. Based on the odor emissions, the frequency of odor exceedances was calculated using a specified 4 OU/m^3 threshold limit. The required meteorological parameters (wind direction frequency, wind speed, and atmospheric stability) for the dispersion calculations

are given in the database of the HNS-TRANSMISSION model. From the analysis of the frequency of exceedances for the number of hours in a year, the resulting setback distances along the 16 wind direction axes are plotted around the emitting point on a Google map (*Fig. 2*).

Table 3. Input and output data for odor emission calculations for the municipal solid waste landfill in Dunakeszi, Hungary

Input data:	
Annual waste acceptance	200,000 t/yr
Waste density	0.6 t/m^3
Working days	300 day/yr
Height of daily deposited waste layer	3 m/day
Surface of active parcels	3000 m^2
Surface of the restored parcels	22,000 m^2
Output data:	
Emissions from the daily deposited waste layer	21,852 OU/s
Emissions from active parcels	24,000 OU/s
Emission from restored parcels	88,000 OU/s
Total odor emissions (OU/s)	133,852 OU/s

Fig. 2. Odor setback distances along the 16 wind directions around a municipal solid waste landfill in Dunakeszi, Hungary.

6. *Model testing and validation*

For testing and validation purposes, the OT model was compared to three international odor models: W-T model, Purdue model, and Minnesota OFFSET model (*Guo et al.*, 2004). The first two models are based on empirical principles, while the OFFSET model incorporates an atmospheric dispersion module.

In this study, odor setback distance calculations were made for 12 swine farms in the USA. The livestock facilities were located in the State of Minnesota. The sizes of the swine farms were different, and the type and number of animals also differed as shown in *Table 4*.

Table 4. Characteristics of the 12 livestock operation farms (*Guo et al.*, 2004)

Farm	Types of swine	Odor sources	
		Buildings (m^2)	Outside manure storage
1	960 nursery to finishing	4 barns (735)	None
2	1720 finishing	2 barns (1637)	None
3	2500 nursery/finishing	7 barns (2725)	None
4	750 sows	2 barns (1869)	1 lagoon (91 × 91 m)
5	600 sows, 2500 nursery/finishing	6 barns (3450)	1 earthen basin (31 × 38 m)
6	2000 nursery, 1000 sows	3 barns (3534)	1 earthen basin (61 × 61 m)
7	1300 sows farrowing to weanling	3 barns (3348)	2 earthen basins (61 × 48 m, 61 × 61 m)
8	1300 sows, 4000 nursery	3 barns (4167)	2 earthen basins (58 × 58 m, 58 × 61 m)
9	1400 sows, 2800 nursery	4 barns (4508)	2 earthen basins (48 × 48 m, 48 × 76 m)
10	2400 sows farrowing to weanling	3 barns (6882)	1 tank (1116 m^2), 1 basin (61 × 76 m)
11	4600 sows farrowing to weanling	6 barns (13020)	2 tanks (1116 m^2), 1 basin (61 × 122 m)
12	3500 nursery, 3500 finishing	5 barns (4185)	2 earthen basins (61 × 152 m, 61 × 203 m)

Based on the given data concerning farm size, swine types, outdoor manure storage, and meteorological parameters measured at the Rochester, MN Airport, odor setback distances were calculated using the newly developed OT model and were compared to the results of other methods – the W-T model, the Purdue model, and the OFFSET model, as summarized in *Guo et al.* (2004). In this study, the terrain around each swine farm was assumed to be flat.

The calculated setback distances for the 4 models are shown in *Table 5*. Although the OT model calculates setback distance for the 16 wind directions, in this study the maximum setback distance was considered around each swine farm, irrespective of wind direction. The numbers (kilometers) are the maximum setback distances, considering the percent probability of a nuisance in a year. In the case of the OT and OFFSET models, the given percentages represent the percentage of hours per year when an odor threshhold would likely be exceeded. The two cases for the Purdue model are the farthest (f) and shortest (s) setback distances that represent the 'worst' and 'best' cases. The W-T model calculates only the maximum setback distance.

Considering the OFFSET model, which also uses an atmospheric dispersion model for the setback distance determination, the distances for the 2, 3, and 4% exceedance probabilities show good agreement with the OT model. In the case of the Purdue model, the agreement is best with the 3, 4, and 5% exceedance probabilities. In general, the best agreement between the OT and W-T models – which is based on an empirical formula – occurs, when comparing the 2% exceedance probability distances (*Fig. 3*).

Table 5. Setback distances (km) determined by four models (OT, OFFSET, W-T, and Purdue). Odor setback distance is shown for the 12 swine farms considering different exceedance probabilities (the percentages refer to the exceedance probabilities in terms of the hours in one year)

		Setback distances (km)											
		Farm											
		1	**2**	**3**	**4**	**5**	**6**	**7**	**8**	**9**	**10**	**11**	**12**
OT	1%	0.35	0.65	0.75	2.05	1.20	1.60	1.90	2.50	2.20	2.25	3.45	5.50
	2%	0.30	0.55	0.65	1.75	1.00	1.40	1.65	2.15	1.90	1.90	2.95	4.60
	3%	0.25	0.40	0.50	1.25	0.75	1.00	1.15	1.50	1.35	1.35	2.05	3.20
	4%	0.25	0.40	0.50	1.20	0.70	0.95	1.10	1.40	1.25	1.30	1.95	3.20
	6%	0.15	0.30	0.35	0.90	0.55	0.70	0.85	1.10	0.95	0.95	1.45	2.30
	9%	0.15	0.25	0.30	0.75	0.45	0.60	0.70	0.90	0.80	0.80	1.15	1.70
OFFSET	1%	1.09	1.55	2.03	2.31	2.43	2.57	2.73	2.77	3.08	3.43	4.52	4.61
	2%	0.63	0.92	1.21	1.39	1.46	1.55	1.66	1.68	1.88	2.10	2.80	2.86
	3%	0.40	0.59	0.78	0.89	0.94	0.99	1.06	1.07	1.20	1.34	1.80	1.84
	4%	0.28	0.43	0.58	0.67	0.71	0.76	0.81	0.82	0.93	1.05	1.44	1.47
	6%	0.20	0.31	0.41	0.48	0.51	0.54	0.58	0.59	0.67	0.75	1.03	1.05
	9%	0.14	0.21	0.29	0.34	0.36	0.39	0.42	0.43	0.49	0.55	0.78	0.80
W-T		0.37	0.56	0.77	1.55	1.09	1.43	1.77	1.71	1.80	2.06	2.72	3.83
Purdue	f	0.40	0.55	0.64	0.81	1.18	1.01	1.08	1.21	1.13	1.45	2.00	1.37
	s	0.18	0.24	0.42	0.40	0.77	0.66	0.71	0.81	0.74	0.95	1.31	0.97

Model results differ mainly because of the different calculation methods. The OFFSET model uses meteorological parameters and contains the

atmospheric dispersion model INPUFF-2 (*Petersen* and *Lavdas*, 1986). The OT model also incorporates a Gaussian dispersion model, however, the odor emission calculations differ between the two. Although the OT model incorporates the odor emission techniques in the Purdue model, wind frequency is the only meteorological parameter considered in the Purdue model. This affects the model results. Again, the W-T model is an empirical model, developed by correlating odor emissions with data on the spatial extent of odor complaints (*Guo et al.*, 2004).

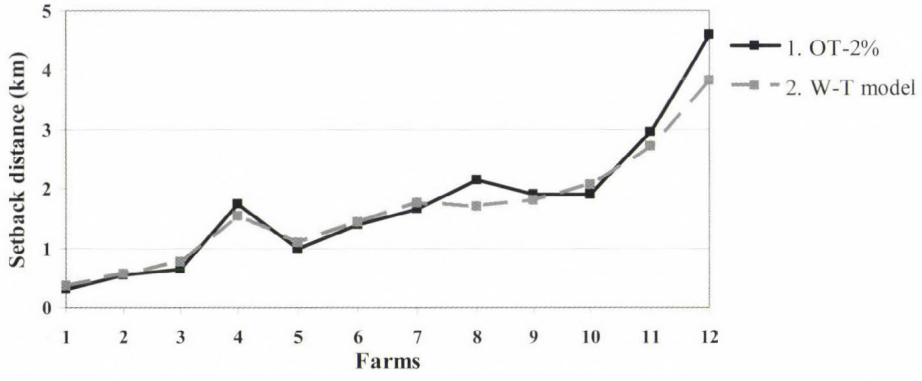

Fig. 3. Comparison of maximum setback distances: OT model and W-T model. The OT model distances are for the 2% exceedance probability case. The W-T model distances are the maxima calculated.

7. Sensitivity study

A sensitivity study was conducted in order to compare setback distance as a function of animal type, number of animals, and odor threshold limit. The study site is near the city of Kecskemét (Törökfái) in Hungary, and the exceedance probability considered was 2%. First, odor emission calculations were carried out for chickens, cattle, and ducks. Two cases were considered based on the number of animals. The results (*Table 6*) show that if the number of animals is doubled, the setback distance grows, but not in direct proportion to the changes in number of animals. Considering different threshold limits (3 OU/m^3, 4 OU/m^3, 5 OU/m^3), the setback distance is inversely proportional to the odor threshold limit.

The setback distance was also compared using a swine farm containing 10000 swine as a function of the odor threshold limit. The change in the setback distance was studied using 3, 4, and 5 OU/m^3. *Figs. 4*, *5*, and *6* clearly show that as the odor threshold limit increases, the maximum setback distance decreases. In the case of 3 OU/m^3 (*Fig. 4*), the maximum setback distance from the

emitting point is 1.75 km. This value is 1.5 km if the odor threshold limit is set at 4 OU/m^3 (*Fig. 5*), while for 5 OU/m^3(*Fig. 6*), the setback distance is just 1.3 km.

Table 6. Sensitivity analysis based on a livestock production farm near Kecskemét. Setback distance is analyzed as a function of odor emission and threshold limit

Animal	**Number of animals**	**Odor emissions**	**Setback distance (m) as a function of odor threshold limit**		
		OU/s	**3 OU/m^3**	**4 OU/m^3**	**5 OU/m^3**
Chickens	100000	107100	600	500	450
	200000	214200	950	850	700
Cattle	2000	74520	500	400	350
	4000	149040	800	650	550
Ducks	100000	32400	250	200	150
	200000	64800	450	350	300

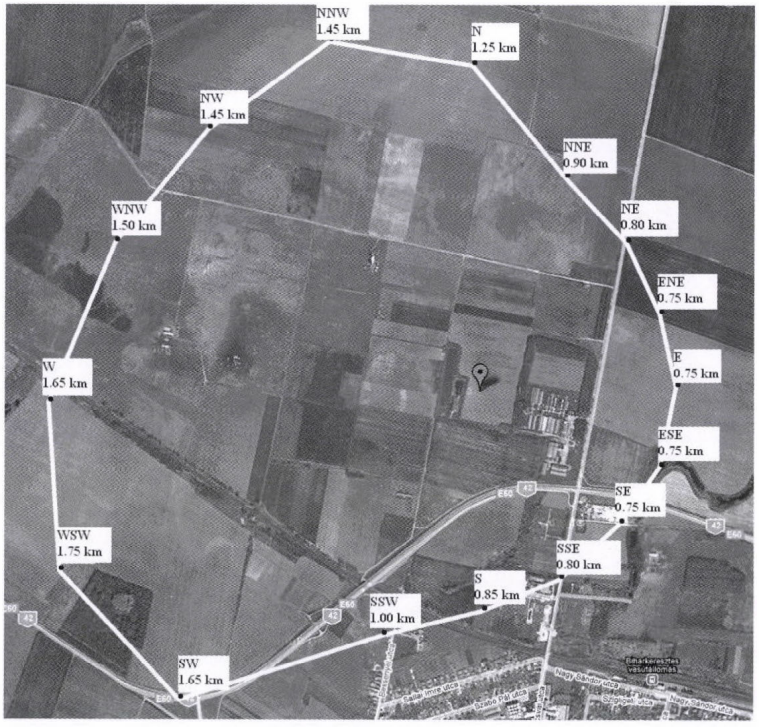

Fig. 4. Maximum setback distances along the 16 wind directions around a swine farm (10,000 swine) in the case of a 3 OU/ m^3 threshold limit. The maximum setback distance is 1.75 km.

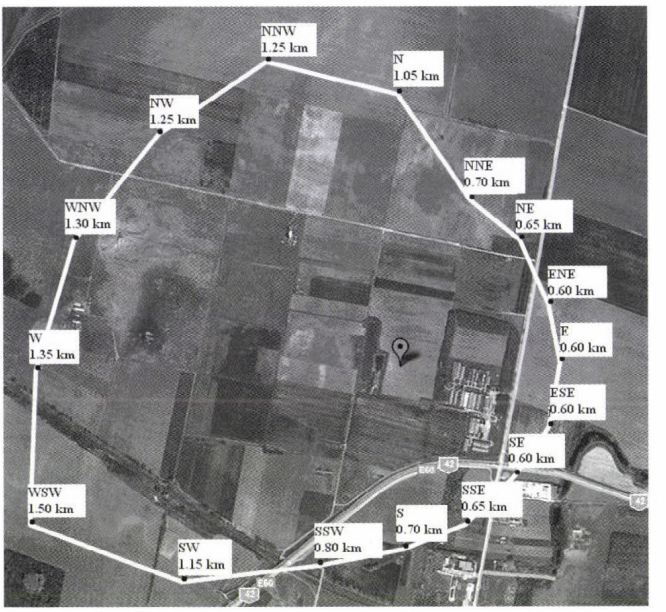

Fig. 5. Maximum setback distances along the 16 wind directions around a swine farm (10,000 swine) in the case of a 4 OU/ m^3 threshold limit. The maximum setback distance is 1.50 km.

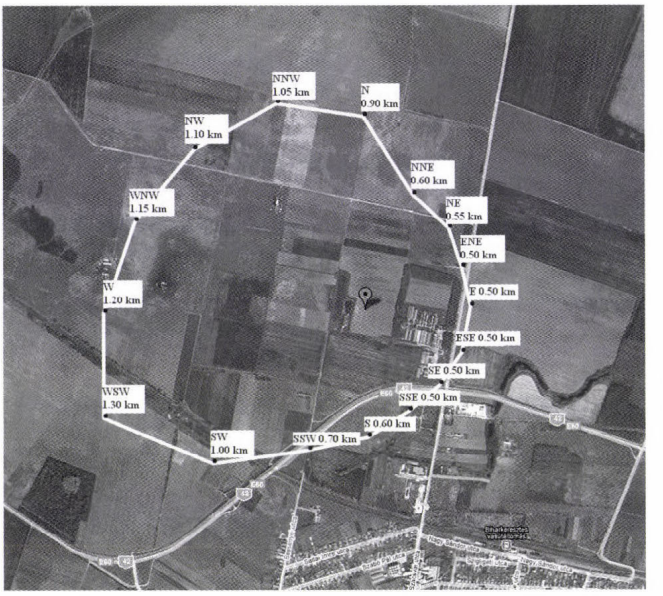

Fig. 6. Maximum setback distances along the 16 wind directions around a swine farm (10,000 swine) in the case of a 5 OU/ m^3 threshold limit. The maximum setback distance is 1.30 km.

8. Conclusions

The ODOR-TRANSMISSION (OT) model has been shown to be a very useful, objective method for determining setback distances around odor-emitting sources. Using the model is quite straightforward and does not require special skills. If the input data are correctly provided, then odor annoyances can be determined quantitatively and in a standardized way.

The odor emissions module in the OT model is based on several studies of animal farms and considers the livestock unit of each type of animals (*Manske*, 1998; *MDA*, 2009). The OT model considers not only animal type and number, but also manure handling methods, indoor or outdoor manure storage buildings, and odor abatement technologies as well. The OT model executes a Gaussian model to calculate the dispersion of odors from their emission point(s). The model currently contains a meteorological database for Hungary (wind direction frequency, wind speed, and atmospheric stability) and can also consider topography around the source. Using visualization techniques to portray model results on a map, e.g., those available via Google®, one can show, in accurate and understandable terms, the area around an emission point where odor annoyances are likely to occur. Model results can help decision-makers and other experts control, plan for, and regulate odor sources.

References

CEN, 2003: Air quality determination of odour concentration by dynamic olfactometry. Ref. No.: EN13725: 2003. Management Centre, Rue de Stassart 36, Brussels.

Guo, H., Jacobson, L.D., Schmidt, D.R., Nicolai, R.E. and *Janni, K.A.,* 2004: Comparison of five models for setback distance determination from livestock sites. *Canadian Biosystems Engineering 46,* 6.17-6.25.

Heber, J., Ni, J.-Q and *Lim, T.T.,* 2002: Odor flux measurements at a facultative swine lagoon stratified by surface aeration. *Applied Engineering in Agriculture 18*, 593-602.

Lim, T.T., Heber, A.J., Ni, J-Q., Grant, R. and *Sutton, A.L.,* 2000: Odor impact distance guideline for swine production systems. In *Water Environment Federation, Odors and VOC Emissions 2000.* Odors/VOC Emissions Conference, Cincinatti, OH, April 17-19, 2000.

Manske, L.L., 1998: Animal unit equivalent for beef cattle based on metabolic weight. *Research Report*, North Dakota State University, Dickinson Research Extension Center.

MDA, 2009: *Minnesota Department of Agriculture*: The Minnesota Livestock Producer's Feedlot Planning and Operations Manual. *Earth Tech, Inc.,* Minneapolis, Minnesota, http://www.mda.state.mn.us/en/sitecore/content/Global/MDADocs/animals/siting/feedlotguide.aspx.

Petersen, W.B. and *Lavdas, L.G.,* 1986: *INPUFF-2.0 A Multiple Source Gaussian Dispersion Algorithm User's Guide.* EPA/600-8-86-024. Washington, DC.

Ritvay, D. and *Kovács, D.*, 2006: The international and Hungarian practice of odor emission control (in Hungarian). National Environmental Conference, Siófok, Sept 19-21, 2006, http://www.vituki.hu/files/buz_szabgyak.pdf.

Schauberger, G. and *Piringer, M.,* 1997: Guideline to assess the protection distance to avoid annoyance by odour sensation caused by livestock husbandry. *Proceedings of the Fifth International Livestock Environment Symposium*, Bloomington (Minnesota), May 29-31, 1997, 170-178.

Sironi, S., Capelli, L., Céntola, P., DelRosso, R., and *Il Grande, M.,* 2005: Odour emission factors for assessment and prediction of Italian MSW landfills odour impact. *Atmos. Environ. 39,* 5387–5394.

Szepesi, D., Fekete, K., Büki,, R., Koncsos, L., and *Kovács, E.*, 2005: Development of regulatory transmission modeling in Hungary. *Időjárás 109*, 257-279.

Williams, M.L. and *Thompson, N.*, 1985: The effects of weather on odour dispersion from livestock buildings and from fields. In *Odor Prevention and Control or Organic Sludge and Livestock Farming* (eds: *V.C. Nielsen, J.H. Voorburg* and *P. L'Hermite*). Elsevier Applied Science Publishers, New York, 227-233.

Winneke, G. and *Steinheider, B.*, 1994: Exposure-response associations between environmental odours, traffic noise, annoyance and somatic complaints. In *Umwelthygiene – Supplement 2.* 1st Internationaler Kongress für Umwelt-medizin. Gesellschaft für Hygiene und Umweltmedizin/-Medizinisches Institut für Umwelthygiene an der Heinrich-Heine-Universität Düsseldorf (Hrsg.), 87-89.

IDŐJÁRÁS

Quarterly Journal of the Hungarian Meteorological Service
Vol. 114, No. 4, October–December 2010, pp. 319–324

Comments on "Greenhouse effect in semi-transparent planetary atmospheres" by Ferenc M. Miskolczi

Henk A. R. de Bruin

*King's College, London, U.K.; Freelance Researcher, Bilthoven, The Netherlands**

(Manuscript received in final form November 12, 2010)

Abstract—This commentary is meant to show that several relationships derived in *Miskolczi* (2007) are debatable and, in my opinion, based on untenable physics.

Key-words: greenhouse effect, radiative equilibrium

1. Introduction

As lecturer emeritus at the University of Wageningen, the Netherlands, I was involved in introductory courses of meteorology, and I used simple 'flat earth greenhouse' models to illustrate the optical effects of greenhouse gases on climate. In these models the atmosphere is replaced with a hypothetic 'glass-plate' with a prescribed spectral emissivity $\varepsilon(\lambda)$ as function of wavelength λ mimicking the optical properties of the different greenhouse gases as well as the so-called atmospheric window. In the context of computer-aided-learning (CAL), I developed a number of interactive CAL modules with which the students could simulate the climate on Earth or Mars by selecting themselves appropriate functions for $\varepsilon(\lambda)$. I always stressed that these CAL modules were meant to clarify a single aspect of the climate system, notably, the optical effects of greenhouse gases, and that they are too simple to describe the actual climate, let alone climate sensitivity. Recently, I came across the papers by *Ferenc Miskolczi* (2007, 2010; hereafter M07 and M10, respectively) and by *van Andel* (2010; hereafter VA10) forcing me to reconsider my understanding of the optical effects of greenhouse gases on climate. I was challenged by van Andel who wrote: *The Miskolczi theory is so different from the usual stream of thought on climate change, that many are either confused, or revolt or embrace this*

*Associate Professor Emeritus Meteorology and Air Quality Group, Wageningen University, Wageningen, The Netherlands; E-mail: hardb@xs4all.nl

theory without really having penetrated it. In this commentary I try to penetrate parts of the Miskolczi theory. It is my objective to show that at several points this theory is untenable.

2. *Brief summary of M07*

The novel laws derived in M07 are:

- Referring to Kirchhoff's law and analyzing sets of radiosonde data with a line-by-line radiation transfer model by *Miskolczi* and *Mlynczak* (2004), it is found that

$$A_A = E_D. \tag{1}$$

- Referring to hydrostatic equilibrium, the virial theorem and identifying E_U as the total internal kinetic energy of the atmosphere, it is stated that

$$E_U = S_U/2. \tag{2}$$

- By applying the principle of conservation of energy and arguing that $S_U - (F^0 + P^0)$ and $E_D - E_U$ represent two flux terms of equal magnitude, propagating into opposite directions, while using the same F^0 and P^0 as energy sources, it is concluded that

$$S_U - (F^0 + P^0) + E_D - E_U = F^0 + P^0. \tag{3}$$

- Next it is stated that the latter equation poses a strict criterion on the global average S_U:

$$S_U = 3OLR/2. \tag{4}$$

- Furthermore, according to M07 this leads to

$$S_U - (F^0 + P^0) = R, \tag{5}$$

where R is the *pressure of thermal radiation at the surface,* which, according to M07 is given by

$$R = S_U/3. \tag{6}$$

- By arguing that the *virial term* $S_V = S_T/2 - E_D/10$ forces the hydrostatic equilibrium while maintaining the radiative balance, it is stated that

$$S_U + S_T/2 - E_D/10 = 3OLR/2. \tag{7}$$

- According to M07, this leads to

$$S_U - (F^0 + P^0) = 6 \text{ A } R/5. \tag{8}$$

- Finally, it is stated in M07 that, among others, the above yields

$$E_U / E_D = 3/5. \tag{9}$$

My comments concern these novel findings.

3. *My comments*

3.1. $A_A = E_D$

In a personal communication, dr. Miskolczi agreed that referring to Kirchhoff's law (and later in M10 to *Prevost*, 1791) can lead to misunderstandings, so I will not comment on these references, except that they are incorrect. The main evidence is to show that $A_A = E_D$ is provided by the calculations of A_A and E_D using the line-to-line radiation transfer model of *Miskolczi* and *Mlynczak* (2004). Arguing that there is *radiative exchange equilibrium between land-sea surface and atmosphere*, these calculations are performed using the boundary condition that the surface temperature equals the air temperature, t_A, at the lowest level in the radiosonde dataset, usually 1.5 or 2 m. Moreover, it is assumed that the surface is black for long-wave radiation. So, in the line-to-line calculations yielding A_A and E_D, the boundary conditions

$$S_U = \sigma t_a^4 \tag{10}$$

are used.

This choice or assumption explains why it is found that $A_A = E_D$. Experience shows that E_D can be approximated accurately with

$$E_D = \varepsilon_{atm} \sigma t_a^4, \tag{11}$$

where ε_{atm} is an apparent emissivity of the atmosphere. Accurate radiation transfer will yield an E_D value for a given radiosonde sounding, so this can be written as $E_D = \varepsilon_{atm} \sigma t_a^4$. In fact, the model yields a value for ε_{atm}. If Eq. (10) is used as boundary conditions for the calculation of A_A with the same model, one will find (due to Kirchhoff's law applied to each absorption line) that $\varepsilon_{atm} = \alpha_{atm} = A$ (apparent emissivity equals the apparent absorptivity), by which one obtains $E_D = A_A$. In fact, evidence given in Fig. 2 in M07 supports this argument. For a surface emissivity of 0.96, E_D appears to be not equal to A_A, because now $S_U \neq \sigma t_a^4$.

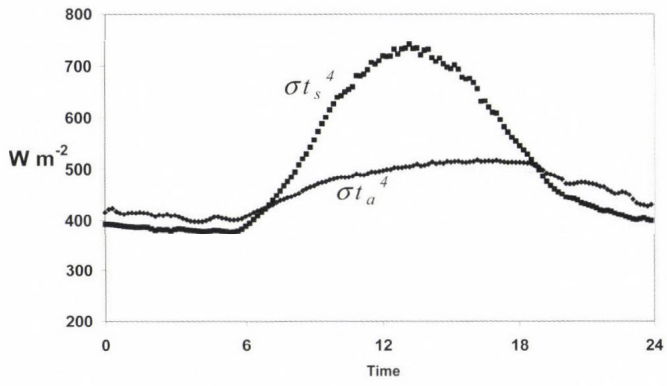

Fig. 1. Diurnal cycle of σt_a^4 and σt_s^4, observations during the MATDADOR field campaign in Arizona desert, t_s is observed with an IR-thermometer.

Is the boundary condition $S_U = \sigma t_a^4$ correct? I don't think so. In textbooks on micrometeorology (e.g., *Geiger*, 1971; *Oke*, 1987; *Garratt*, 1992) it is explained why, in general, the surface temperature is not equal to t_a. In a desert, the difference can exceed 40 °C, but also over grass in mid-latitude climate zones, the difference can be 5 to 10 °C. In the last decade, the sensors to measure surface temperature S_U and E_D are improved significantly, and in open literature many micrometeorological data sets collected over a wide range of surface types can be found. Several of these can be downloaded freely. Some of these are at my disposal and I have sent dr. Miskolczi some results showing clearly that $S_U \neq \sigma t_a^4$. One example is depicted in Fig. 2 of M07. Usually, S_U is greater than σt_a^4 during daytime. Although during nighttime the opposite occurs, the daily mean of the difference is not zero. See, for example, *Fig. 1*. Among others, this is due to non-linearity effects in atmospheric turbulence transfer and, not at least, because during daytime the surface is heated by solar radiation, whereas nighttime cooling is governed by entirely other physical processes. I conclude that, in general, $E_D \neq A_A$. The evidence provided in M07 to show that $E_D = A_A$ is based on the incorrect assumption that $S_U = \sigma t_a^4$. Consequently, all conclusions in M07 drawn from $E_D = A_A$ are untenable. Because in the later sections in M07 often the assumption that the surface temperature equals t_a is adopted, most results derived from that must be considered with caution also.

3.2. Comment on virial theorem and $E_U = S_U/2$

Firstly, I would like to remark that $E_U = S_U/2$ cannot be true in general. Suppose that the atmosphere consists of 20% O_2 and 80% N_2, so solely of diatomic gases, then there is no LW absorption or emission, so $E_U = 0$, whereas, because most

surface have emissivity close to 1, S_U will be greater than 0 due to solar heating. I give this simple example also to introduce my comment on the statement in M07: "*the total internal kinetic energy of the atmosphere, which – according to the virial theorem – hydrostatic equilibrium balances the total gravitational potential energy*", because the actual atmosphere consists primarily of O_2 and N_2, so of diatomic gases. The virial theorem is developed in astrophysics, where it is applied to, e.g., gaseous stars. Without any explanation, the virial theorem is applied to the atmosphere in the gravitation field of the Earth, which is quiet different from the gaseous star case. In stars one has to account for gravitation forces between different layers, whereas in the atmosphere these can be ignored, because they are much smaller than the gravitation force by the Earth. Thus, application of a virial theorem to climate topics is questionable. Anyhow, the virial theorem applied to gaseous stars deals with the potential and internal energy. In textbooks (*Holton*, 1979; *Iribarne* and *Godson*, 1986) one can find that for the atmosphere, in a gravity field that thermodynamic principles lead to $P=(\eta-1)U$, where P is the potential energy, U is the internal energy, and η is the ratio of specific heat at constant pressure and constant volume. Because U can be linked to *the total internal kinetic energy*, I presume that this is meant in M07. But for diatomic atmospheres $P=\frac{2}{5}U$, so P is not equal to U. This result was also found recently by *Toth* (2010). Let us ignore this factor 2/5 and also the question whether horizontal and vertical atmospheric motions of 'air parcels' are included in what is denoted as *total kinetic energy* (these are NOT covered by U, see, e.g., *Toth*, 2010), my main criticism concerns the fact that, without a single clue, in M07 U is linked to E_D. Note that E_D originates from LW radiation emission by three-atomic gases, and the above 'virial theorem' applies to diatomic atmospheres. I conclude that the derivation in M07 of $E_U = S_U/2$ is so unclear that, for the time being, it must be considered not to be based on the first physical principle. The same applies to all further formulas in M07 derived from the virial theorem and $E_U = S_U/2$.

3.3. Comments on $S_U - (F^0 + P^0) + E_D - E_U = F^0 + P^0$ and term R

This equation is based on the following arguments: "$S_U - (F^0 + P^0)$ and $E_D - E_U$ *represent two flux terms of equal magnitude, propagating into opposite directions, while using the same F^0 and P^0 as energy sources. The first term heats the atmosphere and the second term maintains the surface energy balance. The principle of conservation of energy dictates that*: $S_U - (F^0 + P^0) + E_D - E_U = F^0 + P^0$ ". I am sorry, this is entirely unclear to me. The conservation law has been applied before. Moreover, I cannot follow the algebra with which next leads to $S_U = 3OLR/2$ and $S_U - (F^0 + P^0) = R$. With $(F^0 + P^0) = OLR$ and $G = S_U - OLR$ the latter yields $R = G$.

The term R was introduced in M07 as *the pressure of thermal radiation at the surface.* Firstly, I have problems with the units. R is a pressure (force per m^2), whereas all other terms are energy flux densities??? But more importantly, in astrophysics one have to account for pressure of radiation indeed, but this pressure (*Jeans*, 1961, page 37) is given by $P_{rad} = \frac{1}{3} aT^4$, with $a = 4\sigma/c$, where c is the speed of light. In M07 it is stated that $R = \frac{1}{3} \sigma T^4$, which is greater than P_{rad} by a factor of $c/4$! The correct expression shows that LW radiation effects on atmospheric pressure can be ignored entirely. Consequently, any statement referring to P_{rad} must be considered inappropriate to explain atmospheric phenomenon. Statements such as "*G will always be equal to the radiation pressure of the ideal gas and the atmosphere will have a constant optical depth*" (page 8 in M07) and "*Formally, in the presence of a solid or liquid surface, the radiation pressure of the thermalized photons is the real cause of the greenhouse effect, and its origin is related to the principle of the conservation of the momentum of the radiation field.*" are incorrect.

3.4. Further comments

The algebra or physics leading to Eqs. (7)–(9) are not clear to me. In Eq. (7), suddenly the virial term $S_T/2 - E_D/10$ is introduced. Where does this come from? According to Eq. (4) this term is zero. Moreover, I do not understand the way Eqs. (8) and (9) are derived.

Acknowledgement — In content I disagree with his thoughts, but I would like to thank *dr. Miskolczi* for inspiring novel ideas about our climate system.

References

Garratt, J.R., 1992: *The Atmospheric Boundary Layer*. Cambridge University Press, 316 pp.

Geiger, R., 1971: *The Climate Near the Ground*. Harvard University Press, Cambridge, USA, 611 pp.

Holton, J.R., 1979: *An Introduction to Dynamic Meteorology*. Academic Press Inc., 391 pp.

Iribarne, J.V. and *Godson, W.L.*, 1986: *Atmospheric Thermodynamics*. Reibel Publ. Comp., Dordrecht, 259 pp.

Jeans, Sir J.H., 1961: *Astronomy* and *Cosmogony*. Dover, New York, 426 pp.

Miskolczi, F.M., 2007: Greenhouse effect in semi-transparent planetary atmospheres. *Időjárás 111*, 1-40.

Miskolczi, F.M., 2010: The stable stationary value of the Earth's global average atmospheric Planck-weighted greenhouse-gas optical thickness. *Energy and Environment 21*, 243-262.

Miskolczi, F.M. and *Mlynczak, M.G.*, 2004: The greenhouse effect and the spectral decomposition of the clear-sky terrestrial radiation. *Időjárás 108*, 209-251.

Oke, T.R., 1987: *Boundary Layer Climates*. Methuen, London and New York, 435 pp.

Prevost, P., 1791: Mémoire sur l'équilibre du feu. *Journal de Physique 30*, 314–323.

Toth, V.T., 2010: The virial theorem and planetary atmospheres, *Időjárás 114*, 229-234.

van Andel, N., 2010: Note on the Miskolczi theory. *Energy and Environment 21*, 277-292.

INSTRUCTIONS TO AUTHORS OF *IDŐJÁRÁS*

The purpose of the journal is to publish papers in any field of meteorology and atmosphere related scientific areas. These may be

- research papers on new results of scientific investigations,
- critical review articles summarizing the current state of art of a certain topic,
- short contributions dealing with a particular question.

Some issues contain "News" and "Book review", therefore, such contributions are also welcome. The papers must be in American English and should be checked by a native speaker if necessary.

Authors are requested to send their manuscripts to

Editor-in Chief of IDŐJÁRÁS
P.O. Box 39, H-1675 Budapest, Hungary
E-mail: antal.e@met.hu

including all illustrations. MS Word format is preferred in electronic submission. Papers will then be reviewed normally by two independent referees, who remain unidentified for the author(s). The Editor-in-Chief will inform the author(s) whether or not the paper is acceptable for publication, and what modifications, if any, are necessary.

Please, follow the order given below when typing manuscripts.

Title page: should consist of the title, the name(s) of the author(s), their affiliation(s) including full postal and e-mail address(es). In case of more than one author, the corresponding author must be identified.

Abstract: should contain the purpose, the applied data and methods as well as the basic conclusion(s) of the paper.

Key-words: must be included (from 5 to 10) to help to classify the topic.

Text: has to be typed in single spacing on an A4 size paper using 14 pt Times New Roman font if possible. Use of S.I. units are expected, and the use of negative exponent is preferred to fractional sign. Mathematical formulae are expected to be as simple as possible and numbered in parentheses at the right margin.

All publications cited in the text should be presented in the *list of references*, arranged in alphabetical order. For an article: name(s) of author(s) in Italics, year, title of article, name of journal, volume, number (the latter two in Italics) and pages. E.g., *Nathan, K.K.,* 1986: A note on the relationship between photo-synthetically active radiation and cloud amount. *Időjárás 90,* 10-13. For a book: name(s) of author(s), year, title of the book (all in Italics except the year), publisher and place of publication. E.g., *Junge, C.E.,* 1963: *Air Chemistry and Radioactivity.* Academic Press, New York and London. Reference in the text should contain the name(s) of the author(s) in Italics and year of publication. E.g., in the case of one author: *Miller* (1989); in the case of two authors: *Gamov* and *Cleveland* (1973); and if there are more than two authors: *Smith et al.* (1990). If the name of the author cannot be fitted into the text: *(Miller,* 1989); etc. When referring papers published in the same year by the same author, letters a, b, c, etc. should follow the year of publication.

Tables should be marked by Arabic numbers and printed in separate sheets with their numbers and legends given below them. Avoid too lengthy or complicated tables, or tables duplicating results given in other form in the manuscript (e.g., graphs).

Figures should also be marked with Arabic numbers and printed in black and white or color (under special arrangement) in separate sheets with their numbers and captions given below them. JPG, TIF, GIF, BMP or PNG formats should be used for electronic artwork submission.

Reprints: authors receive 30 reprints free of charge. Additional reprints may be ordered at the authors' expense when sending back the proofs to the Editorial Office.

More information for authors is available: antal.e@met.hu

Published by the Hungarian Meteorological Service

Budapest, Hungary

INDEX 26 361

HU ISSN 0324-6329